



저작자표시-비영리-변경금지 2.0 대한민국

이용자는 아래의 조건을 따르는 경우에 한하여 자유롭게

- 이 저작물을 복제, 배포, 전송, 전시, 공연 및 방송할 수 있습니다.

다음과 같은 조건을 따라야 합니다:



저작자표시. 귀하는 원저작자를 표시하여야 합니다.



비영리. 귀하는 이 저작물을 영리 목적으로 이용할 수 없습니다.



변경금지. 귀하는 이 저작물을 개작, 변형 또는 가공할 수 없습니다.

- 귀하는, 이 저작물의 재이용이나 배포의 경우, 이 저작물에 적용된 이용허락조건을 명확하게 나타내어야 합니다.
- 저작권자로부터 별도의 허가를 받으면 이러한 조건들은 적용되지 않습니다.

저작권법에 따른 이용자의 권리는 위의 내용에 의하여 영향을 받지 않습니다.

이것은 [이용허락규약\(Legal Code\)](#)을 이해하기 쉽게 요약한 것입니다.

[Disclaimer](#)

Doctoral Thesis

Epitaxially Grown Metal Oxide Semiconductors on
Two-Dimensional Carbon Materials

Hyo-Ki Hong

Department of Materials Science and Engineering

Graduate School of UNIST

2018

Epitaxially Grown Metal Oxide Semiconductors on Two-Dimensional Carbon Materials

Hyo-Ki Hong

Department of Materials Science and Engineering

Graduate School of UNIST

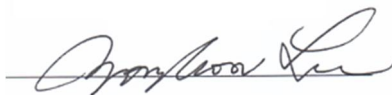
Epitaxially Grown Metal Oxide Semiconductors on Two-Dimensional Carbon Materials

A thesis/dissertation
submitted to the Graduate School of UNIST
in partial fulfillment of the
requirements for the degree of
Doctor of Philosophy

Hyo-Ki Hong

6. 11. 2018 of submission

Approved by



Advisor

Zonghoon Lee

Epitaxially Grown Metal Oxide Semiconductors on 2-Dimensional Carbon Materials

Hyo-Ki Hong

This certifies that the thesis/dissertation of Hyo-Ki Hong is
approved.

6/11/2018 of submission

signature




Advisor: Zonghoon Lee

signature



Soon-Yong Kwon: Thesis Committee Member #1

signature



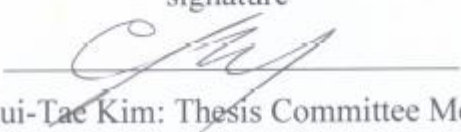
Jung-Woo Yoo: Thesis Committee Member #2

signature



Young Chul Jun: Thesis Committee Member #3

signature



Eui-Tae Kim: Thesis Committee Member #4;

Abstract

After the discovery of mechanically exfoliated graphene, there is an unprecedented increase in research on ultra-thin two-dimensional (2D) nanomaterials in the fields of nanotechnology, physics, chemistry, condensate physics, materials science, and biological sciences. Nowadays, a number of new 2D nanomaterials are discovered and widely studied, such as metal oxides, hexagonal boron nitride, transition metal dichalcogenides, 2D covalent organic frameworks, 2D metal-organic frameworks, black phosphorene, carbon nitride, and silicene. Among them, 2D metal oxides have unique structural properties because of their numerous low-coordinated surface dangling bonds and noticeable lattice structural distortion. 2D metal oxides also exhibit unique electric, mechanic, and catalytic performance owing to their ultrahigh surface-to-volume ratio and quantum confinement effects. Nowadays, there has been increasing studies that focus on 2D metal oxides, offering unprecedented opportunities in a variety of applications. However, the synthesis of 2D metal oxide nanosheets in a common and easy way is still a big challenge.

This work mainly focused on atomically thin semiconducting metal oxide on graphene carries unique combination of adjustable band gaps, high charge carrier mobility, and optical transparency, which can be widely applied for opto-electronics, supercapacitors, rechargeable batteries and catalysis. But, study on the epitaxial formation and properties of metal oxide monolayer on 2D carbon layer remains unexplored due to hydrophobic 2D carbon surface and limits of conventional bulk deposition technique. Here, we report atomic scale study of heteroepitaxial growth and relationship of a single-atom-thick ZnO layer on graphene using atomic layer deposition. Among the metal oxide, we selected ZnO semiconductor as forms of epitaxial growth on 2D carbon substrate. Also, we demonstrate atom-by-atom growth of zinc and oxygen at the preferential zigzag edge of a ZnO monolayer on graphene through *in situ* observation. We experimentally determine that the thinnest ZnO monolayer has a wide band gap (up to 4.0 eV), due to quantum confinement and graphene-like structure, and high optical transparency. This study can lead to a new class of atomically thin two-dimensional heterostructures of semiconducting oxides formed by highly controlled epitaxial growth.

Contents

Chapter 1: Introduction	1
Chapter 2: Research background	3
2.1. Advanced transmission electron microscopy	3
2.1.1. Aberration corrected transmission electron microscopy	3
2.1.2. Theory of high resolution imaging	5
2.1.3. Electron energy loss spectroscopy	6
2.2. Electron beam-specimen interactions	8
2.2.1. Electron beam-induced crystallization	8
2.2.2. Atomic rearrangement in 2D nanostructures induced by electron beams	11
2.3. Fabrication of 2D metal oxide nanomaterials.....	13
2.3.1. Top-down synthesis of 2D metal oxide nanosheets	14
2.3.2. Bottom-up synthesis of 2D metal oxide nanosheets	16
Chapter 3: Atomic scale study on growth and heteroepitaxy of ZnO monolayer on graphene ...	17
1. Introduction.....	17
2. Experimental section	18
2.1. Graphene sample preparation	18
2.2. Graphene transfer	18
2.3. Graphene TEM grid preparation.....	18
2.4. Atomic resolution TEM imaging and STEM-EELS spectra	19
2.5. Atomic layer deposition of ZnO	19
2.6. Characterization.....	19
2.7. Image simulation	19
2.8. DFT calculation	20
3. Results and discussion	20
3.1. ZnO monolayer on pristine and UV/Ozone-treated graphene.....	20
3.2. Field effect transistor measurement	24
3.3. Time-elapsd ARTEM images showing ZnO monolayer growth behavior under electron beam irradiation.....	25
3.4. Heteroepitaxial relations of the ZnO monolayer on graphene analyzed through aberration-corrected TEM	29
3.5. Heteroepitaxial relations of the ZnO monolayer on graphene analyzed through aberration-corrected TEM	35
3.6. Model system	40
3.7. Electronic and optical properties of ZnO deposited with different ALD cycles on UV/Ozone	

treated graphene	42
3.8. Raman spectroscopy, X-ray diffraction, XPS, STEM-HAADF imaging, EELS core loss spectra and SEM measurement	47
3.9. Compositional analysis of ZnO deposited on graphene by TOF-SIMS measurement.....	53
4. Conclusion	54
Chapter 4: Synthesis of high-quality monolayer graphene by low-power plasma	55
1. Introduction.....	55
2. Experimental section	56
2.1. Graphene sample preparation	56
2.2. Graphene transfer	56
2.3. Characterization.....	56
3. Results and discussion	57
3.1. Methane as an effective hydrogen source for monolayer graphene synthesis on Cu.....	57
3.2. Domain size and graphene coverage on copper foil using ICP-CVD.....	59
3.3. Graphene synthesized at 850°C for 60 min at plasma powers of 0, 50, and 200 W with an Ar/H ₂ /CH ₄ gas mixture	61
3.4. TEM images of graphene on copper foil.....	61
3.5. Electrical properties of graphene using ICP-CVD.....	65
4. Conclusion	67
References.....	68

List of Figures

[Chapter 2]

Figure 1. (a) Schematic illustration of the spherical aberration of a converging lens.²³ (b) Spherical aberration is compensated by combining the converging lens with a suitable diverging lens.²³

Figure 2. The relationship between the classic energy diagram of a metal atom (left) and the density of the filled and empty states in the conduction/valence band (right).⁴⁰

Figure 3. Schematic representation of the redistribution of the incoming beam energy along an irradiated amorphous specimen.⁴¹ Most of the energy input is used to excite the atoms of the specimen and only a small fraction gets stored in the form of defects.⁴¹ The atoms in stimulated specimen rearrange until they adopt a crystalline configuration as the specimen decays into a lower energy state (lower than the original amorphous state).⁴¹

Figure 4. (a) to (c) Graphene sheets irradiated at different current densities. (a) Low irradiation dose ($1.25 \times 10^8 \text{ e nm}^{-2}$), (b) moderate dose ($2.94 \times 10^9 \text{ e nm}^{-2}$) and (c) high dose ($9.36 \times 10^9 \text{ e nm}^{-2}$).⁴¹ The specimen irradiated at a higher dose shows a higher degree of beam-induced disordering (amorphization) as it can be noticed by observing the blurred-out Fourier transformation pattern on the inset.⁴¹ (d) A small pore on a single-layer grapheme sheet is highlighted in red.⁵⁹ A Fe cluster is seen right below the pore. (e) After 3 s of irradiation, the atoms of the Fe cluster have moved onto the pore forming an atomic-thick free-standing that completely covers the perforation.⁵⁹ (f) A ZnO nanocrystalline sits on top of a grapheme flake.¹ (g) The ZnO crystallite has rearranged into a flat single-sheet ZnO layer with an hexagonal configuration.¹

Figure 5. Strategies for the synthesis of 2D metal oxide nanosheets.¹⁷ Top) Schematic illustration of a typical top-down routine together with microscopy images of the synthesized 2D Cr_2O_3 , ZrO_2 , Al_2O_3 , and Y_2O_3 nanosheets; Bottom) schematic illustration of a typical bottom-up synthesis routine together with microscopy images of 2D TiO_2 , ZnO , Co_3O_4 , and WO_3 .¹⁷

[Chapter 3]

Figure 1. ZnO monolayer on pristine and UV/Ozone-treated graphene. (a) Atomic resolution image of ZnO nanoclusters on pristine graphene. The inset in the upper right corner shows the Fourier transform of the image. (b) Atomic resolution image of ZnO nucleation on a graphene substrate after 180 s of UV/Ozone treatment. The inset in the upper right corner shows the Fourier transform of the image. The scale bar is 2 nm.

Figure 2. ZnO monolayer on pristine and UV/Ozone-treated graphene. (a) The Raman spectra of UV/Ozone-treated graphene after different treatment times. (b) XPS spectra of the UV/Ozone-treated graphene after different treatment times. (c) Current–gate voltage curves of the graphene for different UV/Ozone treatment times. The inset in the upper corner shows the contact angle to the graphene substrate treated to UV/Ozone from 0 to 180 s. (d) Mobility-carrier concentration curves of the graphene for varying UV/Ozone treatment time.

Figure 3. Time-elapsd ARTEM images showing ZnO monolayer growth behavior under electron beam irradiation. (a) ZnO monomer is adsorbed onto the graphene substrate. (b) ZnO becomes amorphous. (c) ZnO forms clusters; unstable clusters are desorbed. (d) The ZnO cluster has periodic atomic arrangement for epitaxial growth on graphene. The scale bar is 1 nm.

Figure 4. Time-elapsd ARTEM images show the growth process of ZnO monolayer on graphene monolayer. The scale bar is 2 nm.

Figure 5. (a) ARTEM image of monolayer ZnO misoriented by 10° with respect to graphene substrate. (b) Fourier transform of the image (a). Scale bar is 1 nm.

Figure 6. Heteroepitaxial relationship of the ZnO monolayer on graphene analyzed through aberration-corrected TEM. (a) Atomic resolution image of ZnO misoriented by 30° on graphene. The inset in the upper right corner shows the Fourier transform of the image. (b) Atomic resolution image of ZnO misoriented by 0° . The inset in the upper right corner shows the Fourier transform of the image. Triangular moiré patterns are repeatedly observed every 2 nm. The scale bars indicate 1 nm.

Figure 7. (a) Atomic model of ZnO/Graphene rotated by 30° . (b) Diffractogram pattern obtained through Fourier transform of the atomic model (a). (c) Atomic model of ZnO/Graphene rotated by 0° . The overlaid triangle shows unit moiré pattern. (d) Diffractogram pattern obtained through Fourier transform of the atomic model (c).

Figure 8. Heteroepitaxial relation of monolayer ZnO on monolayer graphene analyzed by using aberration corrected TEM. (a) Histogram of misorientation angles of ZnO on graphene and calculated binding energy. (b) Raw image of Figure 5a. (c) Image simulation result of monolayer ZnO on monolayer graphene. (d) Normalized intensity profiles acquired from the image simulation (black line) and experimental image (red line), corresponding to marked profiles in red dashed lines in (b) and (c). Scale bars indicate 1nm.

Figure 9. The optimized structure of hexagonal (a), oxygen-terminated (b) and zinc-terminated (c) triangular ZnO nanoclusters on graphene (See the Model Systems below for more information). The red and blue spheres represent oxygen and zinc atoms, respectively, and gray-stick honeycomb network represents graphene. (d) The adhesion energy between three types of ZnO nanoclusters and graphene vs the misorientation angle (θ).

Figure 10. Lateral growth of the ZnO monolayer along the zigzag edges. (a) Raw image of Figure 10 (a) at final step 7. (b) Intensity profile acquired from the experimental image (red line). (c) Image simulation of Figure 10 (a) at final step 7. (d) Intensity profile acquired from the image simulation (blue line). The scale bar is 1 nm.

Figure 11. The top view of atomic configuration of each lateral growth step of oxygen- and zinc-terminated zigzag edge models and armchair edge model, respectively. Note that each edge model consists of equal numbers of carbon, zinc, and oxygen atoms. The red, blue, burgundy, and navy spheres represent oxygen atoms, zinc atoms, oxygen adatom, and zinc adatom, respectively, and gray-stick honeycomb network represents graphene.

Figure 12. (a) Top view of atomic configuration of each growth step of normal and parallel to the growth front direction. Red, blue, burgundy, and navy spheres represent oxygen atoms, zinc atoms, oxygen adatom, and zinc adatom, respectively, and gray-stick honeycomb network represents graphene. (b) Formation energy of ZnO growth in normal and parallel to the growth front direction at oxygen terminated zigzag edges. The inset figure shows that the red arrow is normal to the growth front direction and the red arrow is parallel to the growth front of direction.

Figure 13. Lateral growth of the ZnO monolayer along the zigzag edges. (a) Raw image of Figure 10 (a) at final step 7. (b) Intensity profile acquired from the experimental image (red line). (c) Image simulation of Figure 10 (a) at final step 7. (d) Intensity profile acquired from the image simulation (blue line). The scale bar is 1 nm.

Figure 14. The top and side views of the optimized structure of periodic ZnO on graphene. (a) 4×4 supercell of hexagonal unit cell graphene is matched with a 3×3 supercell of ZnO monolayer, where the lattice mismatch is 0.59%. (b) The interlayer distance between ZnO monolayer and graphene is

3.556 Å. The red and blue spheres represent oxygen and zinc atoms, respectively, and gray-stick honeycomb network represents graphene.

Figure 15. Electronic and optical properties of ZnO deposited with different ALD cycles on UV/Ozone treated graphene. (a) The STEM-EELS spectra of ZnO deposited with different ALD cycles on UV/Ozone-treated graphene. The extrapolation lines (dashed lines) indicate the band gap (E_g) values 4.0, 3.71, and 3.25 eV. Each curve is scaled differently. (b) Optical transmittance measurement of ZnO deposited with different ALD cycles on graphene. (c–e) Bright-field images of suspended UV/Ozone-treated graphene after 10, 20, and 200 cycles of ZnO ALD growth. The scale bar is 200 nm. (f–h) ARTEM images of 10, 20, and 200 cycles of ZnO ALD growth on the UV/Ozone-treated graphene substrate. The insets in the upper right corner show the electron diffraction patterns of the imaging regions (f–h). The scale bar is 1 nm.

Figure 16. $(ah\nu)^2$ versus photon energy of ZnO deposited on graphene by using ALD method. The extrapolation lines (dashed lines) indicate optical bandgaps (E_g) of 4.03, 3.78 and 3.22 eV for (a) 10 cycle, (b) 20 cycle and (c) 200 cycles.

Figure 17. Raman spectroscopy of UV/Ozone-treated CVD graphene on the SiO₂/Si substrate, 20 and 200 ZnO ALD cycles.

Figure 18. X-ray diffraction patterns of 20 and 200 ZnO ALD cycles on UV/Ozone-treated CVD graphene on the SiO₂/Si substrate.

Figure 19. XPS spectra of UV/Ozone-treated CVD graphene on the SiO₂/Si substrate with 20 and 200 ZnO ALD cycles. (a) Zn 2*p* and (b) O 1*s*.

Figure 20. Comparison of EEL spectra of a ZnO monolayer and ZnO multilayer. (a) Atomic resolution TEM image of ZnO on graphene. (b) STEM HAADF image of ZnO on graphene. (c) EEL spectrum obtained from the red circle in (b) of show oxygen K-edge and zinc L-edge of the ZnO monolayer on graphene. The inset figure shows the carbon K-edge from graphene. (d) EEL spectrum obtained from the blue circle in (b) of oxygen K-edge and zinc L-edge of the multilayer ZnO on graphene. Scale bars indicate 5 nm.

Figure 21. Scanning electron microscope images of UV/Ozone-treated CVD graphene on SiO₂/Si substrate. (a) SEM image of UV/Ozone-treated graphene on a SiO₂/Si substrate after 20 ALD cycles of ZnO deposition. (b) SEM image of UV/Ozone oxidized graphene on a SiO₂/Si substrate after 200 ALD cycles of ZnO deposition. The scale bar is 200 nm.

Figure 22. TOF-SIMS mapping images and depth profiles of UV/Ozone oxidized CVD graphene on SiO₂/Si substrate, 20 (a & d), 100 (b & e) and 200 (c & f) ZnO ALD cycles.

[Chapter 4]

Figure 1. Graphene synthesized at 850°C for 12 s at plasma powers of 0, 50, and 200 W under an Ar/H₂/CH₄ gas mixture. (a)–(c) show SEM images of graphene domains synthesized at 850°C for 12 s at plasma powers of 0, 50, and 200 W under an Ar/H₂/CH₄ gas mixture. Scale bar is 5 μm. (d) Domain size of graphene as a function of plasma powers of 0–300 W. (h) Raman spectra of graphene synthesized for 12 s at various plasma powers of 0, 50, and 200 W.

Figure 2. (a) Domain size of graphene and (b) Graphene coverage on copper foil as a function of growth time and plasma powers of 0, 50, and 200 W.

Figure 3. Graphene synthesized at 850°C for 60 min at plasma powers of 0, 50, and 200 W with an Ar/H₂/CH₄ gas mixture: (a) SEM image of graphene on copper foil synthesized at 850°C in 60 min as a function of plasma powers of 0, 50, and 200 W. Scale bars indicate 20 μm. (b) Raman spectra of

graphene films on SiO₂/Si substrates, where the films were grown for 60 min at various plasma powers. (c) Intensity ratios of the D and 2D peaks to the G peak. (d) FWHM of a 2D band obtained from the single-Lorentzian fit.

Figure 4. TEM images of graphene on copper foil synthesized at 850°C in 60 min under Ar/H₂/CH₄ conditions and plasma powers of 0, 50, and 200 W. (a)–(c) Grain-boundary map with an overlaid background of the graphene TEM image of the samples deposited at plasma powers of 0, 50, and 200 W, respectively. The yellow box represents dark-field image regions in Fig. 3(d)–(f). Scale bars indicate 5 μm. (d)–(f) Dark-field TEM images of graphene taken from areas 1 to 2. The inset at the bottom-left corner shows the diffraction pattern of the image. Scale bars indicate 200 nm. (g)–(i) ARTEM images of graphene deposited with plasma powers of 0, 50, and 200 W, respectively. Scale bars indicate 1 nm.

Figure 5. (a) Current gate voltage curves of the graphene films synthesized in 60 min as a function of plasma powers of 50 and 200 W. (b) Mobility–carrier concentration curves of graphene films as a function of plasma powers of 50 and 200 W. The inset at the upper corner shows an optical image of a 10-μm-long channel of an FET device using Au/Cr electrodes. Scale bar is 50 μm.

Chapter 1: Introduction

Metal oxide semiconductors are attractive class of materials with outstanding chemical, electrical¹, and physical properties. Metal oxide semiconductors are broadly used in magnetic and electronic devices and other applications¹. The focus of this study is two-dimensional (2D) metal oxide semiconductors. 2D metal oxides semiconductors present clear differences compared with those having three-dimensional (3D) structures². The 2D transition metal oxides appear as single-layered structures, multi-layered structures, and 3D superlattice structures of different transition metal oxides². 2D metal oxide semiconductors have a unique chemical structure. The distinctive personality of the oxygen ion is the key point in creating outstanding properties on a 2D metal oxide surface, and for layered and 2D transition metal oxides, such surface properties dominate the material's performance³⁻⁴.

Furthermore, heteroepitaxial growth of 2D metal oxide semiconductors on 2D carbon-layered nanomaterials by combining high charge carrier mobility and wide band gap has become a new synergetic way to fabricate optoelectronic and flexible⁵⁻⁷ electronic devices. The heteroepitaxial growth of 2D metal oxides into reasonably well-designed architectures⁸, such as ZnO⁹, TiO₂¹⁰, Co₃O₄¹¹, WO₃¹², CuO¹³, MoO₃¹⁴, NiO¹⁵, Rh₂O₃¹⁶, and SnO¹⁷, is performed by various deposition methods, including “bottom-up” and “top-down” approaches. These rationally designed graphene like 2D sheet metal oxides generally have better interaction interfaces with recovered in-plane carrier-transport kinetics and interplane ion transport and recovered electrolytes than the equivalent 3D materials, and thus significantly improve the storage behavior of Na⁺, Li⁺, and other ions⁸. Additionally, the graphene-like 2D layer structure of metal oxides offers a large specific surface area, facilitating the creation of an enlarged number of active sites, achievement of a uniform charge distribution, and acceleration of the insertion-extraction or redox reaction rates⁸. However, these approaches still have various types of issues. In the case of “bottom-up” process, the lateral expansion of graphene-like 2D metal oxides is highly restricted because of unfavorable energetic kinetics. The trial and errors, thus, are particularly noticeable for metal oxide semiconductors that are functionally all-around and especially important for photonics and electronics. The main issue in the case of “top-down” process is that appropriate and strongly layered materials are necessary because 2D templates are weakly stacked via weak van der Waals forces or atomic bonds.

2D substrates, such as graphene or graphene oxide, were selected in this study as they have brilliant electron beam transparency in TEM. Moreover, 2D carbon substrates can be architecturally well-suited with metal oxide materials having zinc blende, wurtzite, and diamond structures, such as ZnO⁹, TiO₂¹⁰, Co₃O₄¹¹, WO₃¹², CuO¹³, MoO₃¹⁴, NiO¹⁵, Rh₂O₃¹⁶, and SnO¹⁷. In addition, it is well-matched to fabricate superior epitaxial metal oxide semiconductors on carbon substrate heterostructures for various device applications. Epitaxially grown metal oxide semiconductors that have reduced concentration of lattice defects do not have contamination from the 2D carbon layer and thermal lattice mismatch. Metal oxides

have more stable bond configuration with 2D carbon substrates compared to conventional amorphous-SiO₂/Si substrates.

Among the heteroepitaxial growth of 2D metal oxide, ZnO semiconductor in the form of an epitaxial layer on 2D carbon has been widely utilized in innovative transparent electronic devices.¹⁸⁻²¹ ZnO has two types of crystal structures: hexagonal wurtzite and zinc blende type. The Hexagonal wurtzite type is the most commonly formed and thermodynamically stable structure. In comparison, the zinc blende structure is in the metastable state. Moreover, ZnO has a wide band gap energy of 3.3 eV at room temperature. On the contrary, by decreasing the thickness of ZnO film, a graphene-like structure can be produced. ZnO grown on graphene has various crystal formation. It is possible to control the shape of ZnO, depending on the growth method or the type of substrate. Furthermore, ZnO can achieve several applications by controlling their shapes, such as nanowires, nanowall, quantum dot, and thin films. ZnO is used as a gas sensor, light-emitting diodes (LEDs), and transistors. Many researchers report on the heterostructures of ZnO and graphene by optimizing its shape, which can be used in many types of applications, such as UV photosensors, flexible devices, and LEDs.

The investigation on metal oxide nucleation and atomic scale growth is one of the most important topics in materials science. In this study, through *in situ* observation, we provide experimental evidence of atom-by-atom growth of oxygen and zinc at the zigzag edge of the ZnO monolayer on graphene using atomic resolution transmission electron microscopy (ARTEM). *In situ* observation systems are able to extract more crystallographic information from ZnO monolayer than out-of-date microscopy. The *in situ* tools are able to invalidate the vacuum-condition and size limitation of ARTEM. These results coincide with the calculation result showing that the formation energy of zigzag edge is more stable than that of armchair edge. Studying metal oxide nucleation and atomic scale growth is one of the most important topics in materials science.

Chapter 2: Research background

2.1. Advanced transmission electron microscopy

2.1.1. Aberration corrected transmission electron microscopy

Observing atomic layer materials is a long-standing goal, and now we have developed a hot topic with the advent of science and technology. Nano and atomic scale deposition requires atomic resolution characterization of the results²²⁻²³. In recent years this goal has been considerable progress made by transmission electron microscopy in order to achieve the makes sense to do research into atomic resolutions²⁴. However, In the 1990s²⁵⁻²⁶, only the successful creation of a universal electronic lens aberration correction than the ARTEM In the process of developing into applied technology, we have developed materials science²⁷⁻²⁹ and condensed-matter physics. Aberration corrected TEM (ACTEM) makes by possible on the occupancy of the atom position be demonstrated, using the resolution electron energy loss spectroscopy (EELS) combining high resolution of energy and the spot allows for potential chemical bonding with the composition signal by atomic force microscopy. Maps the localized atoms in the electronic state. Generally, two types of aberrations are commonly included. First, it is geometric aberration such as chromatic aberration and spherical aberration that comes from electron energy dependence of magnetic field. The latest lens model can only be modified from the previous lens model. An ideal converging lens imaged a point of an object to a corresponding point in the image due to aberration. Figure 1a shows the spherical aberration. The point spread increases with the angle that the actual lens's refracting power creates by the light rays entering the lens into the optical axis. As a result, scattering in the sample at high angles focuses a small distance in front of the Gaussian image plane defined by the low angle beam. The focal length of the electromagnetic lens can be easily changed by adjusting the current passing through the lens coil. This defocusing also induces point spreads and is treated as aberrations. Although these two represent the most important aberrations, there are more than just contributing to the angular distortion as well as the width of the point-spread disk^{28, 30-31}. In particular, the spherical aberration of the converging lens is much too high for the high angle scattering beam is compensated by adding a compensating diverging lens in Figure 1b. This is accomplished by a conventional TEM and a dual hexapole system³²⁻³³ of a scanning TEM (STEM). Many advances in the field of EM have enabled atomic scale imaging about structure and defects in low dimensional materials. The aberration-correction electro-optic hardware can significantly reduce the influence of the inherent spherical aberration of the electron lens, and a chromatic aberration corrector or monochromator can minimize the energy spreading the electron beam illumination for the sub Angstrom imaging³⁴. The most important factor is the development of imaging with low acceleration voltages (60 and 80 kV, which significantly minimizes the damaging effect of the illumination electrons on the specimen³⁵⁻³⁶. Furthermore, the electron-ion scattering cross sectional area increases as the voltage decreases and produces more contrast for a given dose. Finally, the electronic scintillator camera has a lower point spread function at a lower operating voltage, resulting in a sharper image.

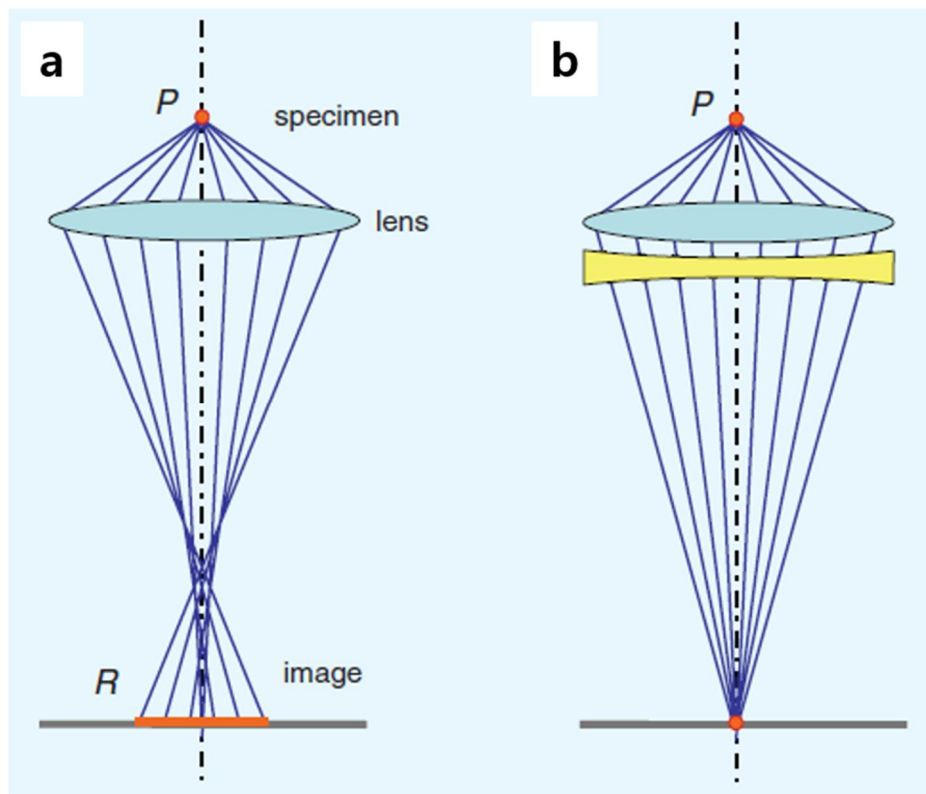


Figure 1. (a) Schematic illustration of the spherical aberration of a converging lens.²³ (B) Spherical aberration is compensated by combining the converging lens with a suitable diverging lens.²³

2.1.2. Theory of high resolution imaging

In EM, electrons are focused using highly-concentrated magnetic fields formed between soft-iron pole pieces and generated by currents flowing through annular coils. In a basic TEM imaging array, the electron beam from the electron gun typically illuminates the specimen through the lens's illumination system. Radiation interacts with the sample and is scattered. The scattered radiation is focused by the objective lens, and the additional magnifier produces a convenient sized image. There are two important factors that determine the essential geometry of an imaging system. First, the wavelength of the electrons determines the range of scattering angles from the specimen. Second, the aberrations of the electron lens limit the angular range of scattered radiation that can make useful contributions to the image. Relative to other radiation of comparable wavelength or energy, electrons interact very strongly with matter.

Elastic scattering is of prime importance for high-resolution imaging³⁷. To avoid serious complications, one must use a specimen thickness of the same order of magnitude as the mean free path for elastic scattering. For electrons, the scattering angles are small, so in traversing a thin specimen, the electron wave does not suffer a sideways displacement dependent on the potential distribution along a straight-line path through the object. Thus, if the potential distribution in the object is represented by a function $\phi(xyz)$, a plane wave transmitted through the object in the z -direction suffers a phase change that is a function of the x,y -coordinates, proportional to the projection of the potential in the z -direction:

$$\phi(xy) = \int \phi(xyz) dz$$

The phase change of the electron wave, relative to a wave transmitted through a vacuum ($\phi=0$), is given by the product of $\phi(xy)$ and an interaction constant σ , which defines the strength of the interaction of electron waves with matter. Mathematically, the effect on an incident wave of the phase change is given by multiplying the incident-wave amplitude by a transmission function

$$q(xy) = \exp[-i\sigma\phi(xy)]$$

This equation is called the phase-object the phase-object approximation (POA). Special preparation techniques are needed to produce specimens the required $\sim 100 \text{ \AA}$ thickness, and the thickness limitation depends on the experimental conditions. For an ideally perfect lens, the image wave function likewise has a phase modulation but no amplitude modulation, so the image-intensity distribution is a constant where the image contrast is zero. To derive some information from the image concerning the object structure, we must use an imperfect lens (which means losing resolution), or resorting to the use of analogs of one of the phase-contrast-imaging schemes used for light optics³⁸

2.1.3. Electron energy loss spectroscopy

EELS relate to energy measurements applied to thin specimens through incident electron beams. There are several ways in which incident electrons can interact with a specimen to generate various characteristics in the energy loss spectrum. One of the most important energy loss processes that can be performed is atomic ionization, in which electrons are emitted from the inside or core of the specimen's shell. This process requires energies equal to or greater than the critical ionization energy, E_c , defined specifically for the core electrons as a function of specific atoms and specific electron shells. That is, at the energy loss level corresponding to E_c , a characteristic signal such as an ionization edge appears in the spectrum to confirm the presence of a specific element in the specimen. The edge intensity can be directly and quantitatively related to the amount of the element present. In addition to containing quantitative elemental information, the ionization edge has a small intensity variation just above the edge onset, called the energy-loss near-edge structure (ELNES)³⁹. ELNES depends on the details of the local nuclear environment, such as coordination and combination types. Understanding the relationship between these microstructural measurements, the electronic structure, and the ultimate properties of materials can provide solutions to many important problems that could not be solved previously. This is especially true if the change in bond length occurs over a small range of lengths.

In the ionization process, the inner shell electrons are given enough energy to overcome the nuclear attraction and are excited by the unfilled energy level if the sample does not fully escape. These unfilled energy levels are a function of the overall electron distribution because of the manner in which atoms and their neighbors (that is, ionized atoms) are bonded to adjacent atoms. Thus, during the ionization, the atoms themselves are converted from the base state of the core shell into the excited state of the core shell with an empty state or hole and excited core electrons at the previously empty energy level. The possible energies that can be applied to the emitted electrons are controlled by the distribution of these unfilled states. Thus, the variations in intensity of the ELNES, which is the ionization edges, are directly related to the distribution of the unfilled electron state and can be interpreted as the bonding state of the ionized atoms.

Besides determining the basic ionization edge type, matrix terms have other important consequences. Generally, there is a possibility that the transition matrix element is not zero and only certain combinations of the initial state and final state are switched. Firstly, the matrix term is not zero; this is called the dipole selection rule, which means that ELNES is a subset of the entire DOS that is part of the appropriate angular momentum symmetry. Secondly, the integral equation involves the multiplication of the initial state and the final state, and this wave function is of significant size only if it is spatially redundant. The initial state is an atom of a state and the final state must have localized components at the same atomic site. For these reasons, the ELNES measures the site and is called a symmetrically planned DOS.³⁹

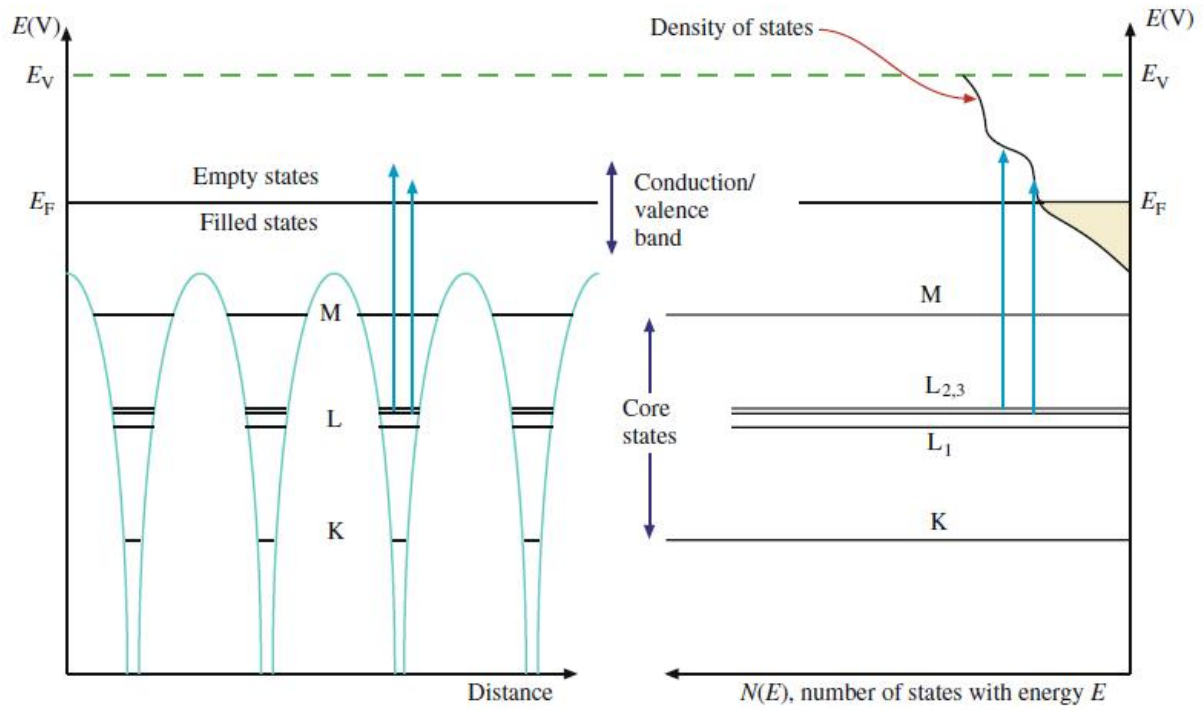


Figure 2. The relationship between the classic energy diagram of a metal atom (left) and the density of the filled and empty states in the conduction/valence band (right).⁴⁰

2.2. Electron beam-specimen interactions

Electron beams (EB) can produce substantial topological changes on TEM specimens⁴¹. This technology is probable to make extended features with atomic-scale in materials such as ZnO monolayer or 2D carbon materials with a high degree of control⁴¹. EB by TEM can substantial changes crystal structure at least three different methods⁴¹. EBs can do so changing the topology of materials and/or rearranging its atomic structure at a local or lateral level⁴¹. We report the accessible works on these three kinds of EB induced changes of 2D metal oxides in accurately the order listed above⁴¹.

2.2.1. Electron beam-induced crystallization

Many literatures are widely documented the crystallization of amorphous sample such as thin film, nanoparticle and nanoclusters by EB bombardment. Occasionally, the crystallization occurs locally over very tiny areas of the specimen. Sometimes, the crystalline areas quickly spread well beyond the irradiated spot; we called “explosive crystallization”. Regarding the “explosive crystallization”, the wide agreement is that is a phenomenon triggered by EB heating effects⁴² in spite of that the crystallization appears at a very fast speed which is uncharacteristic of thermal processes⁴³. However, explosive crystallization can’t be controlled to make clear materials do to the explosive nature of the process. There is more conflict about the physical causes behind the formation of small crystalline domains on specimen irradiated by an EB probe. Some opinions on favor of EBs heating-induced crystallization have been put forward for irradiated oxide films⁴⁴⁻⁴⁷ and possibly for Zr films⁴⁸. Instead, observations advocating for an a-thermal crystallization process of thin films are more numerous⁴⁸⁻⁵⁶. In most cases, the drive mechanism behind the (re-) crystallization process can be subdivided into two categories depending on whether the energy of the main beam E_0 is large enough to overcome the displacement energy E_d of the irradiated material. If the E_d threshold can be reached, crystallization is due to the creation/recombination of point defects and improved atomic mobility.

In principle, high energy electrons are essential for causing crystallization through this elastic processes^{49-50, 53-54}. If E_d can’t be reached, the crystallization mechanism breaks the a-c interfacial bonds that are formed "incorrectly" and reconstitutes the crystalline configuration^{48, 51, 55-56}. Since the crystal threshold is lowered at the defect site, the crystallization process can be driven by an elastic energy transfer events⁵². Other studies have provided a more detailed mechanism to explain the thermal beam induced crystallization⁵⁷. The crystallization path can be described by how the amorphous disordered atomic structure (relatively high internal energy) can be lowered to end its crystallinity (highly aligned), even when subjected to a constant energy input supplied by the e- beam in Figure 3. The energy injected by the beam ΔE_n is redistributed into two parts and the fraction is stored in the form of a generated defect ΔE_{sto} which contributes to the atomic damage of the specimen. The other fraction is dissipated as ΔE_{dis} as the atoms of the impacted specimen are relocated to relax the atomic structure. During the relocation process, the specimen is driven into a thermodynamically unstable “stimulated state” and

decreases rapidly, releasing the total energy amount ΔE_r . After the relocation is complete, the internal energy of the specimen drops the factor of ΔE_{rea} below the initial amorphous state energy value. ΔE_{rea} exclusively describes the difference in free energy of the post-rearrangement crystal structure in relation to the initial disordered state. Typically, these configurations occupy the deepest energy valleys, so there is a high probability that the sample is conceived on the crystal as it rolls out its internal energy landscape.

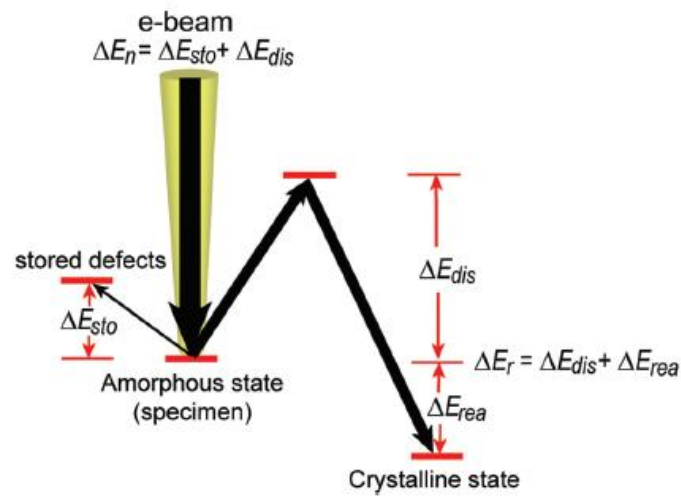


Figure 3. Schematic representation of the redistribution of the incoming beam energy along an irradiated amorphous specimen. Most of the energy input is used to excite the atoms of the specimen and only a small fraction gets stored in the form of defects. The atoms in stimulated specimen rearrange until they adopt a crystalline configuration as the specimen decays into a lower energy state (lower than the original amorphous state).⁴¹

2.2.2. Atomic rearrangement in 2D nanostructures induced by electron beams

Atomic rearrangement in 2D specimens derived by EBs can be observed as a “synthesis” technique when it yields a nanostructure that have properties that are significantly different from the original film. For example, this is achieved when a large area of the a-film is crystallized under EB film irradiation. The procedure may vary depending on atomic sputtering and displacement, either of which is dominant over the other, or both occur at the same time. Large-area crystallization through atomic displacements was determined by inducing a free-carbon layer on the graphene⁵⁸ as well as graphite a-carbon. The accelerated voltage of the 80 kV beam creates a carbon nano onion on the free standing film, while a similar process takes place on the graphene sheet and changes carbon to epitaxial so that the graphene layer is laminated. Graphitization occurs through “inelastic electron scattering interactions”, which is reconfigured as a more stable sp^2 planar carbon isotope by breaking bonds at the carbon. Relocation to a graphene sheet is induced by van der Waals forces due to the hexagonal network of graphene or hBN. The "inverse" transformation of crystalline graphene with an amorphous "glassy" carbon sheet can also be obtained if the sputtering event is included in addition to the EBs induced atomic transfer. Figure 4a-c shows 2D graphene steadily changing with a 100 kV accelerating voltage slightly higher than the sputtering energy threshold of 2D carbon. Specimens of atomically thin iron and ZnO can be made through procedures that rely on EBs-induced atomic rearrangement and continuous self-assembly^{1, 59}. Another document deals with the formation of prominent Fe membranes extending from the graphene vacancies in Figures 4d and e. Fe atoms are usually bound in graphene holes. Another study shows free-standing ZnO for graphene pores in Figures 4f and g. The ZnO structure has a graphene-like structure. The EELS data shows the difference in bonding configuration between ZnO and 3D ZnO, such as graphene. ZnO, such as graphene, fluctuates dynamically under EB due to continuous irradiation.

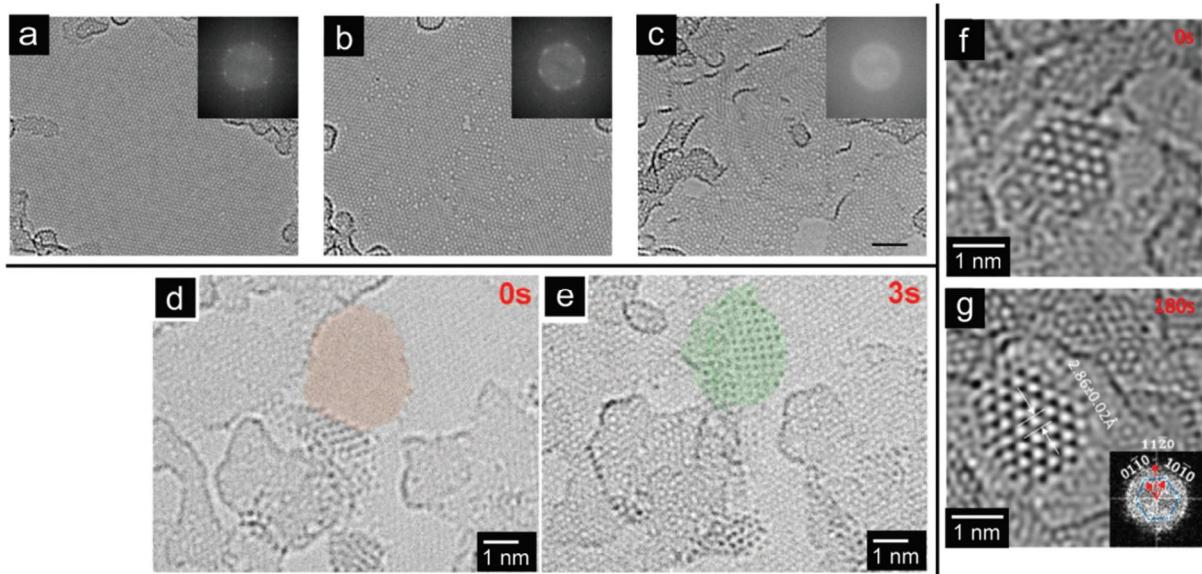


Figure 4. (a) to (c) Graphene sheets irradiated at different current densities.⁴¹ (a) Low irradiation dose ($1.25 \times 10^8 \text{ e nm}^{-2}$), (b) moderate dose ($2.94 \times 10^9 \text{ e nm}^{-2}$) and (c) high dose ($9.36 \times 10^9 \text{ e nm}^{-2}$). The specimen irradiated at a higher dose shows a higher degree of beam-induced disordering (amorphization) as it can be noticed by observing the blurred-out Fourier transformation pattern on the inset.⁴¹ (d) A small pore on a single-layer grapheme sheet is highlighted in red. A Fe cluster is seen right below the pore.⁵⁹ (e) After 3 s of irradiation, the atoms of the Fe cluster have moved onto the pore forming an atomic-thick free-standing that completely covers the perforation.⁵⁹ (f) A ZnO nanocrystalline sits on top of a grapheme flake.¹ (g) The ZnO crystallite has rearranged into a flat single-sheet ZnO layer with an hexagonal configuration.¹

2.3. Fabrication of 2D metal oxide nanomaterials

Due to the large number of members of the 2D metal oxide nanomaterials family, it is very difficult to find a universal and cost-effective routine for synthesizing all types of 2D nanomaterials in a one-pot approach, even if we never stop trying. Generally, the fabrication of 2D metal oxide nanomaterials two approaches can be categorized into “top-down” synthesis and “bottom-up” synthesis. “Top-down” synthesis refers to processes of lowering the size and dimensions of bulk, thin film or other high dimensional materials by mechanical milling, peeling, etc. “Bottom-up” synthesis is a process in which nanomaterials are opposite process in which atoms, molecules, or sometimes proteins are grown or assembled by techniques such as vapor deposition, etc⁶⁰. In addition to the commonly used “top-down” and “bottom-up” approaches, other methods of combining these double procedures have also been used for the making of fusion 2D nanomaterials, for example, where peel-off graphene is used to induce wet conditions 2D nano chemical growth of nanomaterials⁶¹⁻⁶².

2.3.1. Top-down synthesis of 2D metal oxide nanosheets

Several types of 2D metal oxide nanosheets have been produced through a “top-down” strategy after successfully delamination of layered graphite to produce graphene. As with the advantages and disadvantages outlined in Figure 5, “top-down” synthesis is a very simple and effective method that does not require complex facilities and equipment. In addition, this method is easy to scale for relatively large production. 2D nanomaterials fabricated through a “top-down” approach inherit a portion of the crystalline structure of the host crystal and thus usually maintain high crystallinity, which is also a significant advantage for high-speed carrier-charge transport. Graphene can be produced on the scale of hundreds of kilograms using liquid stripping and opens the door for commercialization of this material⁶³. However, there are some disadvantages to the “top-down” method. The main problem is that a weak laminar host crystal with a weak atomic bond or van de Waals forces and weak 2D platelets is needed. 2D materials without corresponding layered host decisions cannot be produced through this “top-down” method. In addition to the requirements for host crystals, the poor-quality distribution of the products obtained is another inevitable challenge. The thickness of the 2D nanomaterials produced by “top-down” techniques, such as liquid exfoliation, is distributed over a wide range from several to several thousand layers. "Top-down" machining can be subdivided into two subcategories: mechanical / thermal cutting and liquid exfoliation. Mechanical cutting was the fastest way to obtain graphene from graphite using scotch tape, and this method was modified to incorporate other 2D nanomaterials by introducing mechanical energy such as ball milling or ultrasonication⁶⁴⁻⁶⁵. Liquid exfoliation is a process carried out in solution in conjunction with organic solvents and / or chemical intercalation or ion-exchange reactions⁶⁶⁻⁶⁷. In the case of liquid exfoliation, the discovery and application of more effective, inexpensive and harmless solvents is a barrier to the commercial production of 2D nanomaterials. There have been many important achievements in the "top-down" synthesis of 2D metal oxide nanomaterials by researchers around the world.

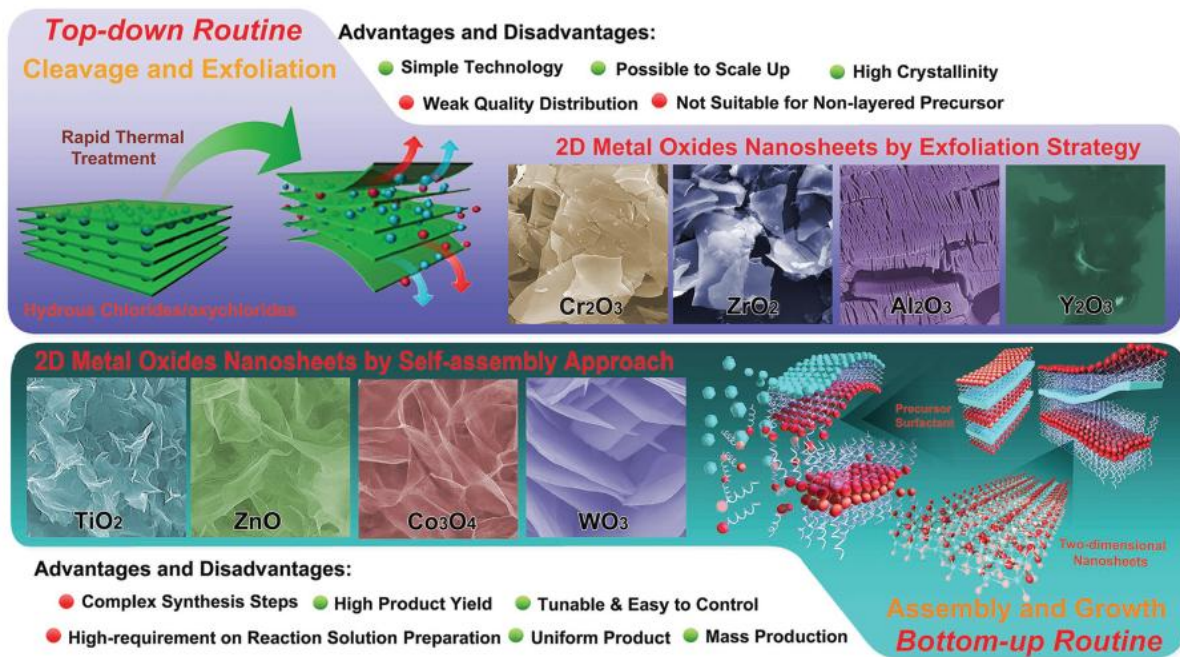


Figure 5. Strategies for the synthesis of 2D metal oxide nanosheets.⁸ Top) Schematic illustration of a typical top-down routine together with microscopy images of the synthesized 2D Cr₂O₃, ZrO₂, Al₂O₃, and Y₂O₃ nanosheets; Bottom) schematic illustration of a typical bottom-up synthesis routine together with microscopy images of 2D TiO₂, ZnO, Co₃O₄, and WO₃.⁸

2.3.2. Bottom-up synthesis of 2D metal oxide nanosheets

“Bottom-up” synthesis methods such as vapor deposition and wet chemical self-assembly have been broadly used to produce 2D metal oxide nanosheets⁶⁸⁻⁶⁹. One common method for the bottom-up growth of 2D metal oxide nanosheets is physical / chemical vapor deposition (PVD / CVD), where solid or gaseous precursors are typically evaporated under heat and deposited on colder substrates. PVD / CVD can produce large area 2D metal oxides on substrates with precisely controlled thickness, good crystallinity and very high charge mobility and has been widely used in the manufacture of 2D electronic materials. However, this method is less productive and therefore has limited applicability to energy storage devices. Wet chemical synthesis is an excellent choice for 2D nanomaterials manufacturing and partially overcomes the clashes between quality and productivity that exist in stripping and deposition methods. The advantages of wet chemical synthesis of 2D nanomaterials include uniform size, shape and thickness of the product, relatively high yield and suitability for scalable synthesis. The disadvantages of this method are complex steps, stringent requirements for reaction solution preparation and relatively expensive precursors. In recent years, we have developed a new molecular self-assembly pathway to produce ultra-thin 2D transition metal oxide nanosheets such as TiO_2 , ZnO , Co_3O_4 , WO_3 , Fe_3O_4 , MnO_2 , etc. by rationally employing lamellar reverse micelles⁷⁰ (Figure 5). This generalized bottom-up method provides a pathway for the synthesis of large quantities of other 2D metal oxide nanomaterials.

Chapter 3: Atomic scale study on growth and heteroepitaxy of ZnO monolayer on graphene

1. Introduction

Heteroepitaxy of metal oxide semiconductors on two-dimensional (2D) layered nanomaterials, combining wide band gap and high charge carrier mobility, has become a new integration method for fabricating flexible⁵⁻⁷ electronic and optoelectronic devices.

Among semiconductor oxides, zinc oxide (ZnO) has been used in novel transparent electronic devices¹⁸⁻²¹ as forms of epitaxial layer on graphene. Thermodynamically, hexagonal wurtzite ZnO¹⁹ is the most stable and common form. The wurtzite structure of ZnO can be transformed to a planar⁷¹⁻⁷³ ZnO monolayer in which Zn and O atoms reside in a trigonal planar coordination, instead of the bulk tetrahedral configuration formed when ZnO is thinned down to a few atomic layers. Since ZnO monolayers on graphene can have many applications in switching electronics and photoactive devices, growth of thin ZnO layers on graphene has been studied extensively^{1, 74-75}.

Various deposition techniques, including metal-organic vapor phase epitaxy⁷⁶, as well as hydrothermal⁷⁷⁻⁷⁸ and electrochemical deposition⁷⁹⁻⁸¹ have been employed for the heteroepitaxial growth of ZnO semiconductors on graphene. However, the strongly hydrophobic graphene limits metal oxide deposition and the wide application of this attractive combination.

Here, we provide experimental evidence for the epitaxial growth of a ZnO monolayer on graphene using atomic resolution transmission electron microscopy (ARTEM) along with the corresponding image simulations and first principles calculations. Furthermore, we demonstrate through *in situ* observation the atom-by-atom growth of zinc and oxygen at the zigzag edge of the ZnO monolayer on graphene at the atomic scale. We also confirm the heteroepitaxial growth and misorientation angles of this ZnO monolayer by direct observation and energy calculations of the heterostructures. In addition, we demonstrate the presence of 2–3 nm quantum dots (QDs) of the epitaxial ZnO monolayer grown by atomic layer deposition (ALD). Unlike conventional bulk ZnO, ZnO QDs have potential applications in nanoscale devices, such as photonic and electronic devices, due to the quantum confinement effect⁸²⁻⁸³. The structural and optical properties of the ZnO monolayer on graphene are studied to exploit the quantum phenomena arising from confinement in QDs.

In particular, a ZnO monolayer can preserve the graphene's intrinsic electronic properties⁸⁴⁻⁸⁶, high carrier mobility⁸⁷, and optical transmission⁸⁸. Ultrathin 2D oxide semiconductors on graphene have potential applications in optoelectronic devices, and a new class of 2D heterostructures may arise through this deposition route.

Graphene is a strongly hydrophobic material, which limits the epitaxial growth of semiconductor oxides and thus hinders their various optoelectronic applications. Previously, we attempted to tailor the surface property of graphene surface from hydrophobic to hydrophilic using several methods including O₂ plasma⁸⁹⁻⁹⁰, O₃ treatment⁹¹⁻⁹², UV irradiation⁹³⁻⁹⁴, surface chemical doping⁹⁵, and electrical

field⁹⁶.

In this study, we select the UV/Ozone treatment⁹⁷⁻⁹⁹ because it provides sufficient energy to reform the graphene surface state, but does not damage the graphene and, it is a simple method uniformly applicable to large areas.

2. Experimental section

2.1. Graphene sample preparation

Graphene was synthesized by CVD on a 25- μm -thick copper foil (99.8% Alfa Aesar, 13382). First, 25 μm thick copper foils was washed with HCl/H₂O (1:10), washed with acetone and alcohol and dried around the air. The dried copper foil was inserted into a quartz tube and heated to 1,000 °C with flowing 2 sccm H₂ at 10 mTorr. After annealing for 1 hour, the gas mixture of 10 sccm CH₄ and 2 sccm H₂ at 100 mTorr was introduced for 25 min to synthesize graphene. Finally, it was rapidly cooling to room temperature while flowing 10 sccm CH₄ and 2 sccm H₂ was performed.

2.2. Graphene transfer

For Raman spectroscopy, XPS, field effect transistors, AFM, SEM and optical transmittance characterization, graphene was transferred to SiO₂ substrates. The graphene was grown on both sides of the copper foils; Ar plasma was the applied to remove the graphene layer on the backside of the Cu foil. The transfer of the graphene films onto 300 nm SiO₂ substrates was performed by the wet etching of the copper substrates. A PMMA solution was spin-coated on the surface of as-grown graphene on Cu foil at the speed of 4,000 rpm for 1 min and baked at 130°C for 10 min. Then the sample was placed into a solution of sodium persulphate (Na₂S₂O₈, a concentration of 0.2 g in 1 ml of water) to etch the underlying copper foil and is then rinsed with deionized water for several times, and then transferred onto a 300 nm SiO₂ substrates. After air drying, the PMMA was dissolved by acetone and the substrate was rinsed with isopropyl alcohol to yield a graphene film on the substrate.

2.3. Graphene TEM grid preparation

In the direct transfer, this support was provided by the target substrate, specifically the TEM grid's carbon film. For TEM characterization, graphene was transferred to Quantifoil holey carbon TEM grids (SPI supplies, 300 meshes, 2 μm hole size) using direct transfer method. To tightly attach the graphene and carbon, the TEM grid is placed on top of graphene on copper foil and a drop of IPA and air-dried. Finally, the sample was placed into a solution of sodium persulphate (Na₂S₂O₈, a concentration of 0.2 g in 1 ml of water) to etch the underlying copper foil and is then rinsed with deionized water for several times.

2.4. Atomic resolution TEM imaging and STEM-EELS spectra

Transmission electron microscopy (TEM) analysis was performed by using an aberration-corrected TEM, Titan G2 Cube 60-300kV (FEI) installed at UNIST. To minimize beam exposure to the sample, images were collected at a low operating voltage of 80 kV with a minimal beam exposure approach. STEM HAADF images and EELS spectra were recorded with a monochromatic beam at 80kV with a probe size of 1.5 nm and an energy resolution of $0.2\pm 0.05\text{eV}$, as measured from the full-width-at-half-maximum of the zero-loss peak.

2.5. Atomic layer deposition of ZnO

ZnO growth on graphene was conducted in an automatic atomic layer deposition system (SVT associate ALD), using a low vacuum condition with 10 sccm of ultra-high pure Ar (99.999%) carrier gas in all deposition sequences. Diethylzinc (DEZ, Sigma Aldrich) and deionized water ($> 18\text{ M}\Omega$) were prepared as precursors of seed layers in stainless cylinders, enclosed by a heater and thermocouple at room temperature and 30°C , respectively. For one cycle of ZnO monolayer growth, DEZ precursor was first injected into the growth chamber for 0.1 seconds ($\sim 80\text{ mTorr}$). Then, the chamber was purged with Ar carrier gas ($\sim 1000\text{ mTorr}$) for 30 seconds to remove residues and other impurities. Then, deionized water was injected for 0.5 s ($\sim 100\text{ mTorr}$). Finally, the chamber was purged with the Ar gas ($\sim 1000\text{ mTorr}$) to remove any remaining residues. The substrate temperature was maintained at 200°C during the deposition process. The set of ZnO samples presented in this report was grown by 10, 20, 100 and 200 ALD cycles.

2.6. Characterization

Raman spectra were acquired with a WiTech confocal Raman microscope (Helium Neon Laser 532 nm). X-ray Photoelectron Spectroscopy (XPS) analysis was performed K-alpha system (Thermo Fisher Instruments Inc.). Contact angle was measured using Phoenix 300 (SEO Inc.). X-ray Diffraction (XRD) was measured using D8 Advance (Bruker Instruments Inc.). SEM images were taken using S-4800 (Hitachi Instruments Inc.). The UV-Vis-NIR was measured using Cary 5000 (Agilent Instruments Inc.). The Time-of-Flight Secondary Ion Mass Spectrometry (TOF-SIMS) was analyzed using TOF-SIMS 5 (ION TOF Inc.). Electrical properties were measured in physical property measurement system (PPMS, Quantum Design) with controlling high vacuum and temperature variations.

2.7. Image simulation

Image simulations of AR-TEM Image were performed using MacTempasX with the experimental conditions. The simulated structure was constructed by Vesta and Matlab with an interlayer distance of 3.556 \AA which was estimated from DFT Calculation (Supplementary Figure 7b). Brightness

normalization and profiling were performed by Matlab.

2.8. DFT calculation

Density functional theory (DFT) calculation was performed with DMol³ module¹⁰⁰⁻¹⁰². Exchange and correlation interaction was described by the generalized gradient approximation (GGA) with Perdew-Burke-Ernzerhof (PBE) functional¹⁰³. Spin polarization was taken into account for all calculations. Core treatment was set to be all electrons relativistic with DNP 4.4 basis set. The convergence criteria for the geometry optimization were 2.0×10^{-5} Ha for energy, 0.004 Ha/Å for force, and 0.005 Å for displacement, respectively. The self-consistent field convergence was smaller than 1.0×10^{-5} Ha. The long-range dispersion correction was taken into account with the semi-empirical DFT-D2 method suggested by Grimm¹⁰⁴.

3. Results and discussion

3.1. ZnO monolayer on pristine and UV/Ozone-treated graphene

Figure 1 shows a ZnO monolayer grown on pristine graphene and the UV/Ozone-treated graphene after 20 ALD cycles. Figure 1a shows the ZnO deposited on the pristine graphene surface after 20 ALD cycles. Blue indicates the crystallized ZnO monolayer. Figure 1b, however, shows larger size of ZnO crystals epitaxially grown on the UV/Ozone-treated hydrophilic graphene surface after 20 ALD cycles. The crystalline ZnO monolayer is clearly visible and the ZnO coverage is much larger on the UV/Ozone-treated graphene. The misorientation angle of 0° is the most common. In order to investigate the effect of UV/Ozone treatment on graphene, Raman spectra are obtained for the graphene as a function of the UV/Ozone treatment time from 0 to 600 s (Figure 2a). After up to 180 s of UV/Ozone treatment, pristine graphene bands remain intact. However, after 300 s of the treatment, strong D (1345 cm^{-1}) and D' (1618 cm^{-1}) bands are observed in the spectra, suggesting the formation of lattice defects. These results indicate that excessive UV/Ozone treatment damages the graphene lattice⁹⁷. The X-ray photoelectron spectroscopy (XPS) results (Figure 2b) mainly display a C 1s peak, related to the sp^2 C-C bonds based on the UV/Ozone treatment time. The XPS spectra show a gradual decrease in the height and broadening of the sp^2 C-C bonds with increasing UV/Ozone treatment time. Such behavior is likely caused by p -type doping induced by the UV/Ozone treatment⁹⁷. The results of Raman spectroscopy and XPS indicate that excessive UV/Ozone treatment induces significant crystal lattice damages and graphene doping. The effects of UV/Ozone treatment on the electrical properties are also investigated through field-effect transistor (FET) measurements. The FET devices are fabricated to have a graphene channel (width = 200 μm , length = 5 μm) between the Au electrodes on the SiO₂/Si substrate. The mobility of the three pristine graphene FETs is 1346, 1648, and 1490 $\text{cm}^2/\text{V}\cdot\text{s}$, which changes to 1281, 1424, and 1361 $\text{cm}^2/\text{V}\cdot\text{s}$, respectively, after the UV/Ozone treatment without remarkable Dirac voltage

changes. Thus, the mobility decreases only by about 10%, suggesting that our UV/Ozone treatment does not severely deteriorate the graphene structure (Figure 2c, d). The inset in Figure 2c shows the change in the contact angle of water on graphene after the 180s UV/Ozone treatment, which is measured with an optical contact angle meter in ambient environment. The contact angle decreases from 87° to 67° for the UV/Ozone-treated graphene, indicating enhanced hydrophilicity. Therefore, we find that 180 s is the optimum UV/Ozone treatment time for ZnO deposition on a graphene substrate. Under these conditions, the graphene surface shows hydrophilicity without deteriorated electrical properties caused by lattice damage.

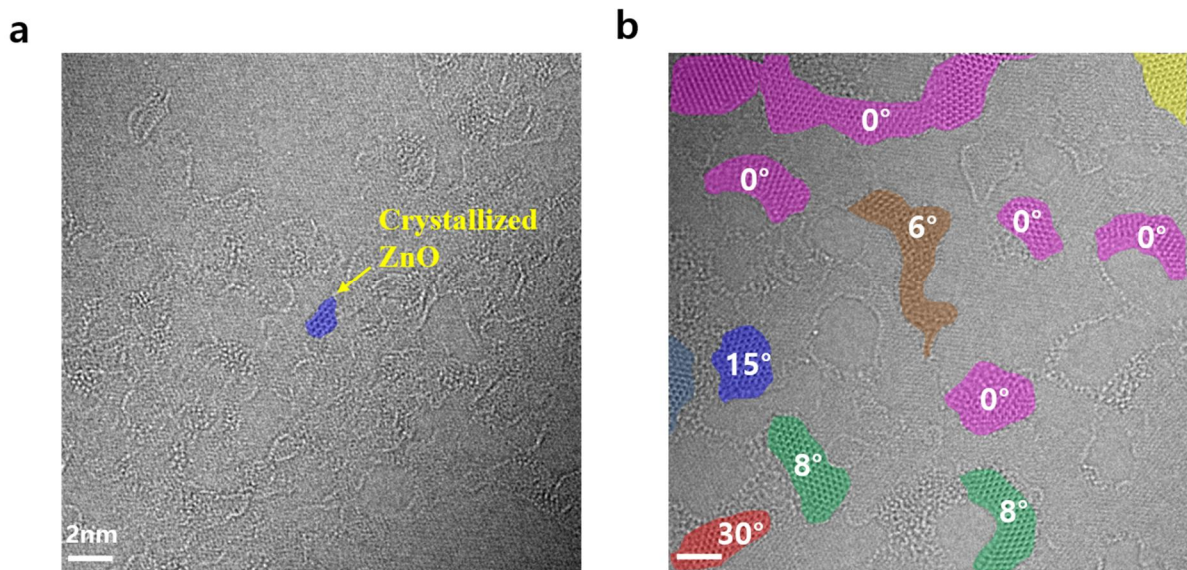


Figure 1. ZnO monolayer on pristine and UV/Ozone-treated graphene. (a) Atomic resolution image of ZnO nanoclusters on pristine graphene. The inset in the upper right corner shows the Fourier transform of the image. (b) Atomic resolution image of ZnO nucleation on a graphene substrate after 180 s of UV/Ozone treatment. The inset in the upper right corner shows the Fourier transform of the image. The scale bar is 2 nm.

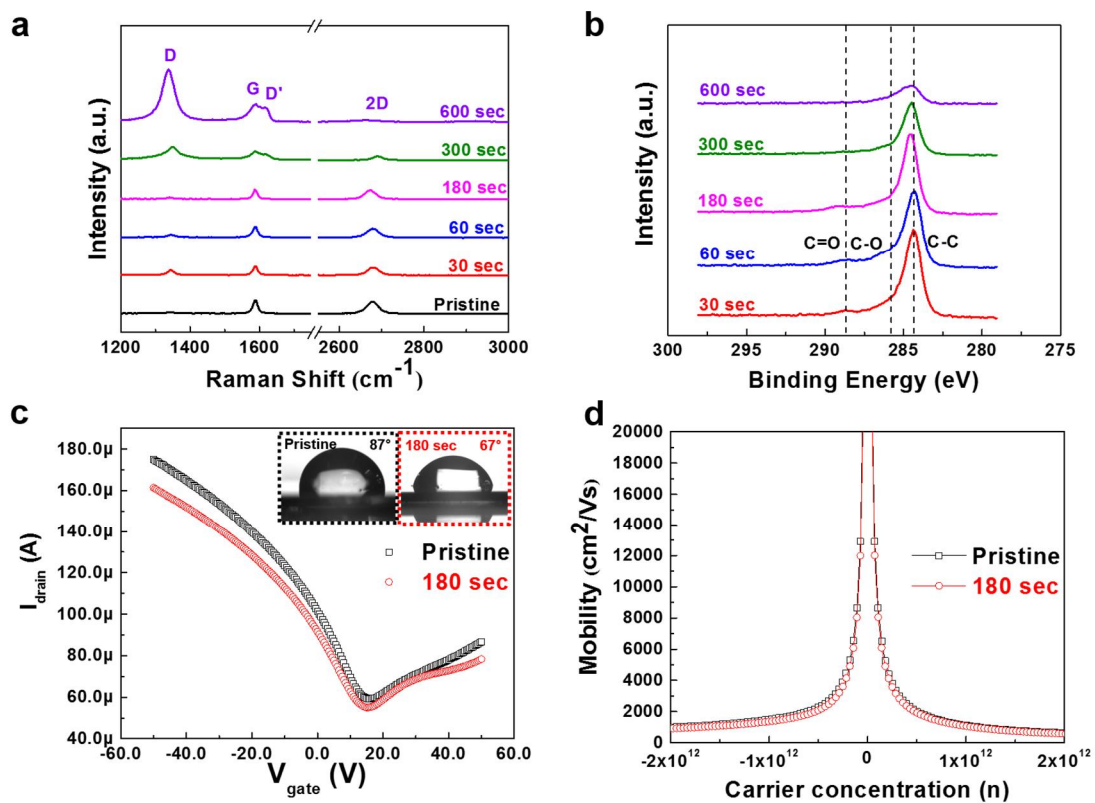


Figure 2. ZnO monolayer on pristine and UV/Ozone-treated graphene. (a) The Raman spectra of UV/Ozone-treated graphene after different treatment times. (b) XPS spectra of the UV/Ozone-treated graphene after different treatment times. (c) Current–gate voltage curves of the graphene for different UV/Ozone treatment times. The inset in the upper corner shows the contact angle to the graphene substrate treated to UV/Ozone from 0 to 180 s. (d) Mobility–carrier concentration curves of the graphene for varying UV/Ozone treatment time.

3.2. Field effect transistor measurement

Graphene synthesized by CVD on a copper foil (see Methods) was transferred to a p-doped 500 μm Si substrate covered with a 300 nm of SiO_2 layer. The electrode patterns of source and drain were fabricated by photolithography with width 200 μm and length 5 μm , and then Au was directly deposited in a thermal deposition system in a high vacuum ($<10^{-7}$ Torr). The prepared device was installed to the PPMS and annealed in a high vacuum condition at 100 $^\circ\text{C}$ to remove residual dopants and impurities from the photolithography with air contamination. After 3 hours of annealing, V_d - I_d characteristic depending on gate bias was measured at room temperature and we analyzed three samples, calculated the mobility of 1346, 1648 and 1490 $\text{cm}^2/\text{V}\cdot\text{s}$, respectively (at $n = 10^{12}$). To compare the UV/Ozone treatment effect, the measured sample was immediately transferred from the PPMS to the UV/Ozone chamber, and then exposed UV/Ozone during 180 seconds. The treated sample was quickly moved back to the PPMS and measured the field effect behavior with the same condition of the untreated one. All transfer times including the UV/Ozone treatment were less than 4 min to avoid contaminating doping in air. The UV/Ozone-treated graphene devices showed 1281, 1424 and 1361 $\text{cm}^2/\text{V}\cdot\text{s}$ without notable Dirac voltage shift by air doping, indicated about 5, 14 and 10% decrease only compared to the pristine graphene conditions.

3.3. Time-elapsed ARTEM images showing ZnO monolayer growth behavior under electron beam irradiation

The diffusion of monomers is the basic form of mass transport on graphene flat surface¹⁰⁵⁻¹⁰⁶. For technological purposes, it is often desirable to achieve layer-by-layer or Frank-van der Merwe growth to produce smooth layers. Under thermodynamic equilibrium conditions, the growth mode is determined by the surface energy¹⁰⁷. The epitaxial growth of ZnO wets the flat graphene surface completely when the surface energy of the ZnO monolayer is lower than that of the graphene surface; in the opposite case, the deposited material forms three-dimensional islands, following the Vollmer-Weber growth mode¹⁰⁷. Figure 2 shows time-elapsed ARTEM images taken during the epitaxial growth of the ZnO monolayer on the graphene surface triggered by electron beam irradiation. First, the ZnO monomer is adsorbed onto the graphene's flat surface (Figure 3a). Then, the diffused and desorbed species may also attach to an island nucleated in an earlier growth stage (Figure 3b). The next step is the formation of clusters, where unstable clusters are desorbed (Figure 3c). Then, the ZnO cluster develops which exhibits a periodic atomic arrangement. The epitaxially grown ZnO crystals have a diameter of 2 nm (Figure 3d). Especially, in the lateral growth of ZnO, the highest growth rate is observed along the c-axis and the large facets are usually $\{10\bar{1}0\}$ and $\{11\bar{2}0\}$, because it is energetically favorable when the $[10\bar{1}0]$ or $[11\bar{2}0]$ direction of ZnO matches the $[10\bar{1}0]$ direction of graphene¹⁰⁸. The ZnO monolayer has a (0001) polar surface plane, which is atomically flat and stable¹⁰⁹⁻¹¹⁰. During the coalescence stage (Figure 4), there is a distinct difference in the relative orientation of the ZnO crystals and the graphene surface. The ZnO monolayer has a facet edge development as shown in the time-elapsed images. In addition, it has a graphene-like structure along the c-axis and the ZnO adatoms are adsorbed onto the $\{10\bar{1}0\}$ facets. This shows that some crystals in the ZnO monolayer undergo non-epitaxial growth, rotated by 10° during the initial growth stage (Figure 5).

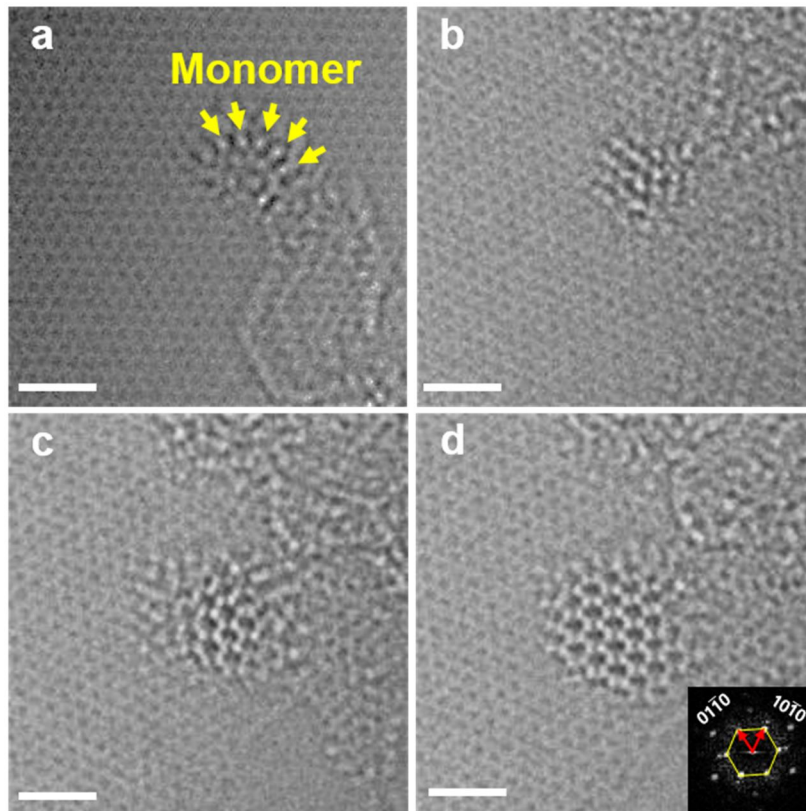


Figure 3. Time-elapsd ARTEM images showing ZnO monolayer growth behavior under electron beam irradiation. (a) ZnO monomer is adsorbed onto the graphene substrate. (b) ZnO becomes amorphous. (c) ZnO forms clusters; unstable clusters are desorbed. (d) The ZnO cluster has periodic atomic arrangement for epitaxial growth on graphene. The scale bar is 1 nm.

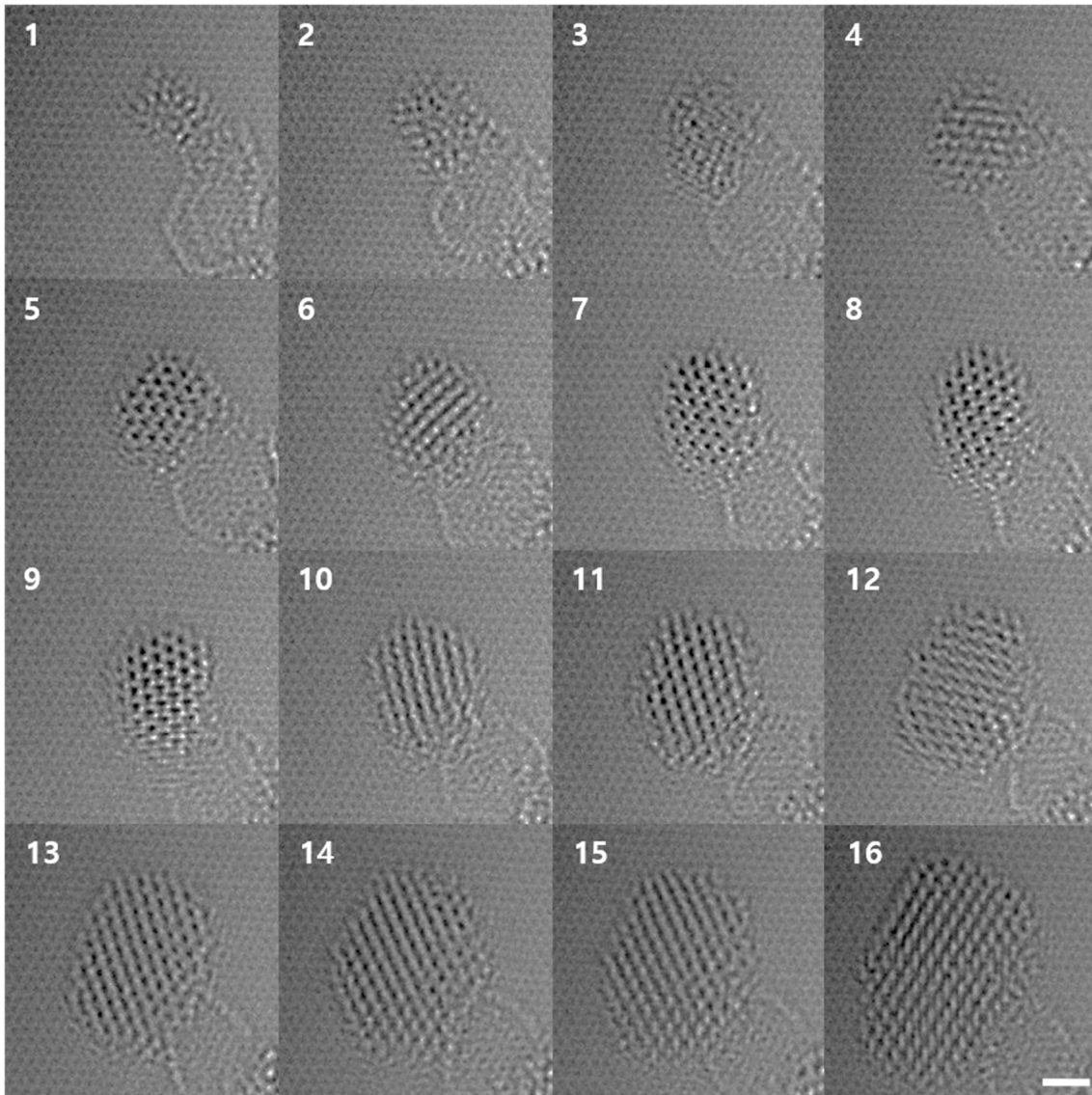


Figure 4. Time-elapsing ARTEM images show the growth process of ZnO monolayer on graphene monolayer. The scale bar is 2 nm.

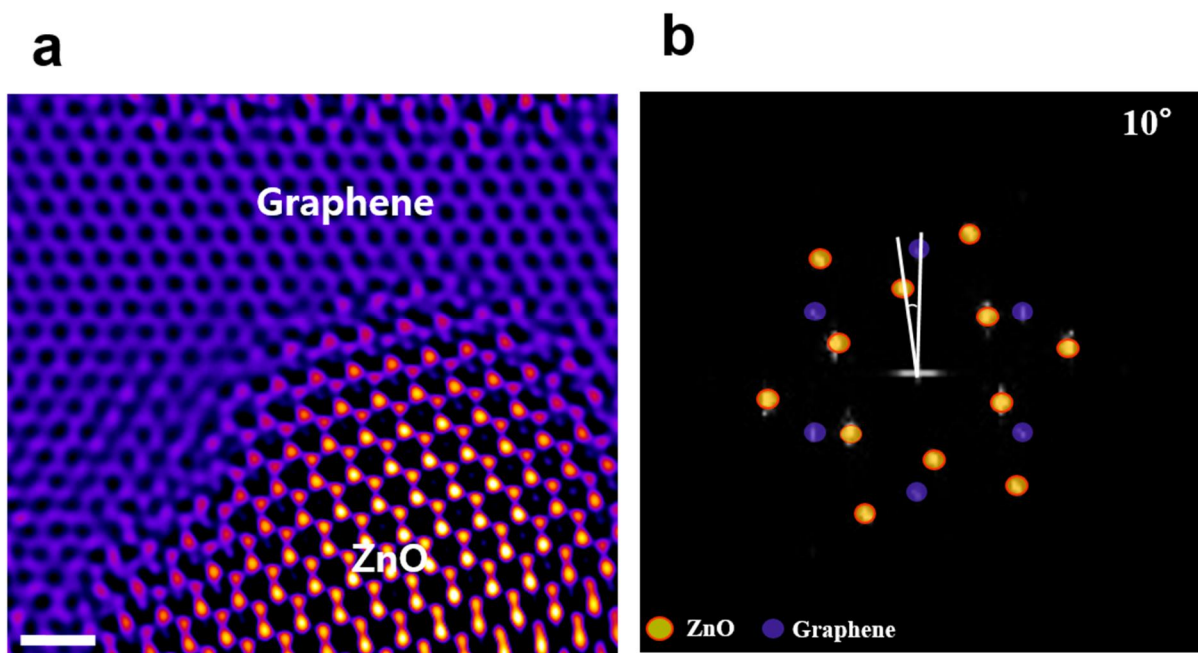


Figure 5. (a) ARTEM image of monolayer ZnO misoriented by 10° with respect to graphene substrate. (b) Fourier transform of the image (a). Scale bar is 1 nm.

3.4. Heteroepitaxial relations of the ZnO monolayer on graphene analyzed through aberration-corrected TEM

ZnO is crystallographically misoriented by 30° with respect to the graphene substrate to minimize the dangling bond density. The misorientation angles of 0° and 30° can be explained by the heteroepitaxial relationship between the ZnO monolayer and graphene; it is energetically favorable when the $[10\bar{1}0]$ or the $[11\bar{2}0]$ crystallographic direction of ZnO matches the $[10\bar{1}0]$ direction of the graphene¹⁰⁸. Figure 6 shows the heteroepitaxial relationship of the ZnO monolayer with the graphene surface, as revealed through ARTEM analysis. Figure 6a shows an atomic resolution image of the ZnO monolayer misoriented by 30° on the graphene. The inset in the upper right corner shows the Fourier transform of the image. According to the ARTEM analysis, the atomic model of ZnO/graphene rotated by 30° is simulated as shown in the Figure 7a. The corresponding simulated diffractogram (Figure 7b) is in good agreement with the diffractogram of the ARTEM image (Figure 6a). The ZnO monolayer, misoriented by 0° and 30° on the graphene, appears during the initial growth stage and eventually becomes misoriented by 0° as ZnO crystals grow further.

Figure 6b shows an ARTEM image of the ZnO layer on graphene misoriented by 0° . The image clearly shows a unit triangular Moiré pattern with a periodicity of about 2.0 nm, which is attributed to the lattice misfits. The determined lattice constants for ZnO ($a \approx 3.3 \text{ \AA}$, $c \approx 5.2 \text{ \AA}$) and graphene ($a \approx 2.46 \text{ \AA}$) agree well^{1, 73} with the reported lattice constants of graphene-like ZnO and graphene.

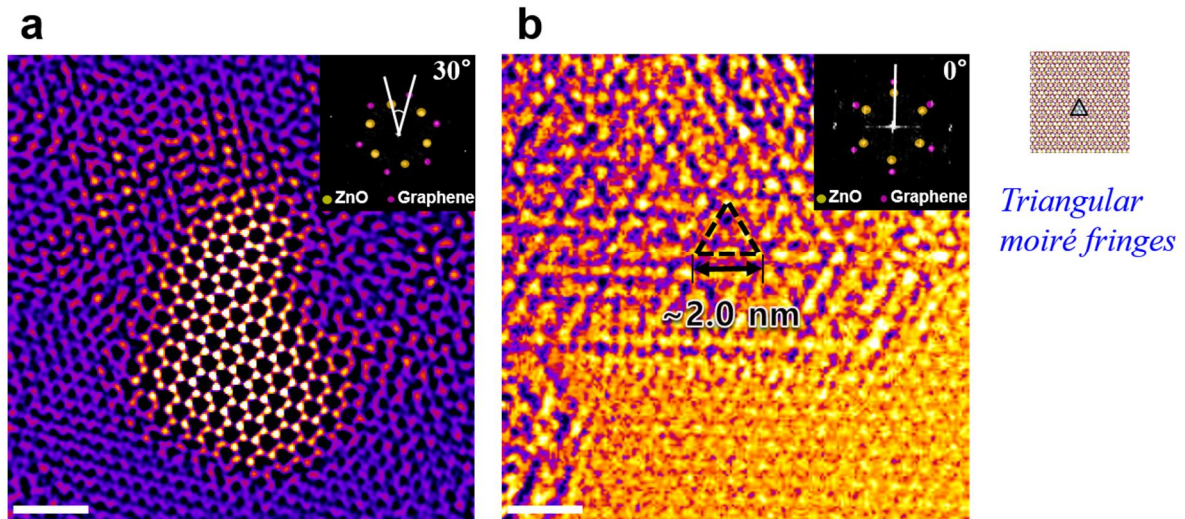


Figure 6. Heteroepitaxial relationship of the ZnO monolayer on graphene analyzed through aberration-corrected TEM. (a) Atomic resolution image of ZnO misoriented by 30° on graphene. The inset in the upper right corner shows the Fourier transform of the image. (b) Atomic resolution image of ZnO misoriented by 0°. The inset in the upper right corner shows the Fourier transform of the image. Triangular moiré patterns are repeatedly observed every 2 nm. The scale bars indicate 1 nm.

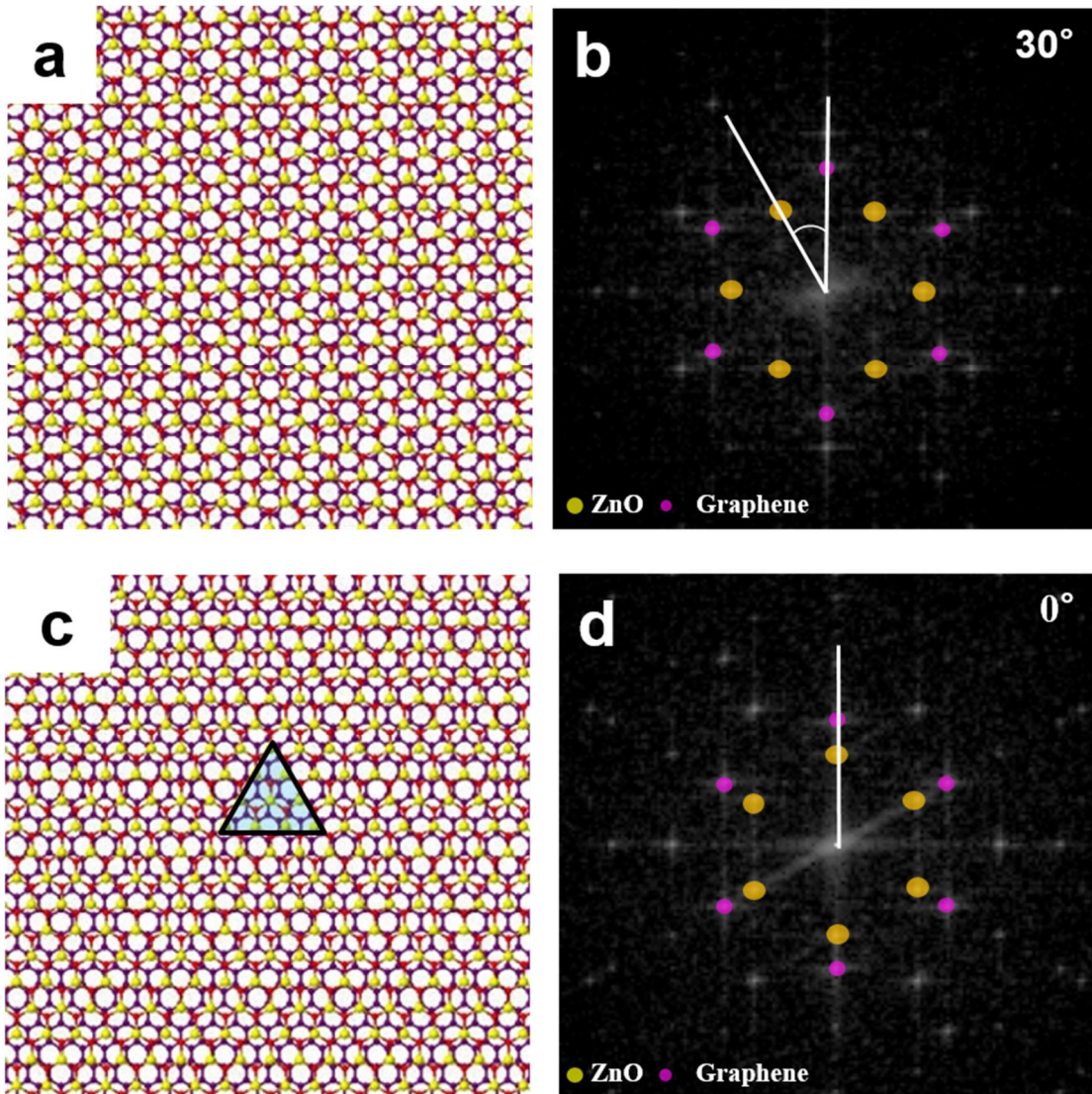


Figure 7. (a) Atomic model of ZnO/Graphene rotated by 30°. (b) Diffractogram pattern obtained through Fourier transform of the atomic model (a). (c) Atomic model of ZnO/Graphene rotated by 0°. The overlaid triangle shows unit moiré pattern. (d) Diffractogram pattern obtained through Fourier transform of the atomic model (c).

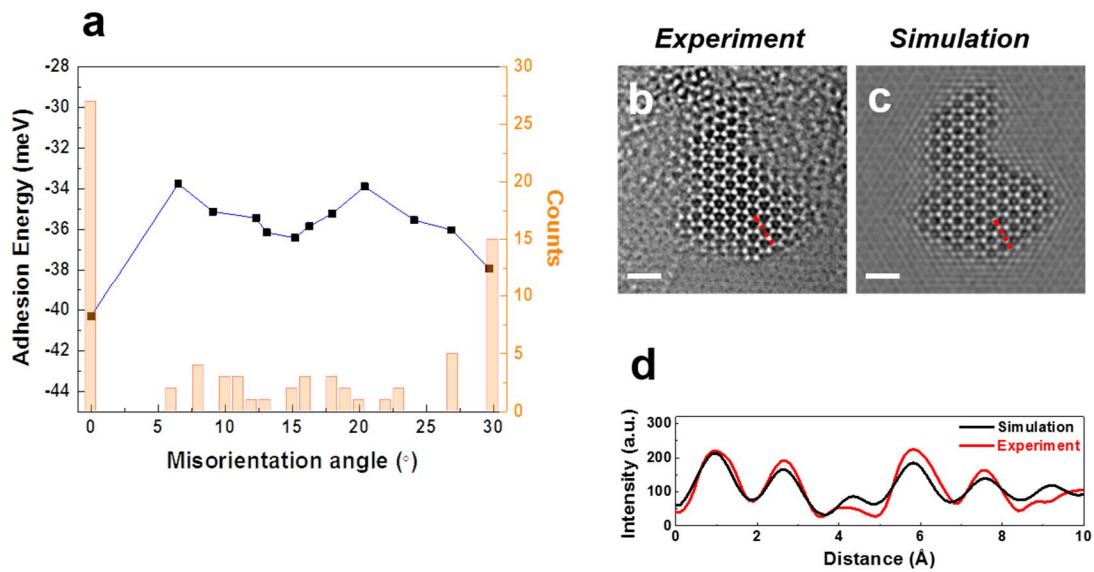


Figure 8. Heteroepitaxial relation of monolayer ZnO on monolayer graphene analyzed by using aberration corrected TEM. (a) Histogram of misorientation angles of ZnO on graphene and calculated binding energy. (b) Raw image of Figure 5a. (c) Image simulation result of monolayer ZnO on monolayer graphene. (d) Normalized intensity profiles acquired from the image simulation (black line) and experimental image (red line), corresponding to marked profiles in red dashed lines in (b) and (c). Scale bars indicate 1nm.

These results are in good agreement with the atomic model and the diffractogram (Figure 7c and d, respectively). In order to reveal the specific misorientation angles observed through the experiment, the stability of each misorientation angle is assessed by calculating the adhesion energy (E_{ad}) as follows:

$$E_{ad} = (E_{total} - (E_{ZnO} + E_G))/N \quad (1)$$

where E_{total} , E_{ZnO} , and E_G represent the energies of the ZnO nanocluster on graphene, the freestanding ZnO nanocluster, and the freestanding graphene, respectively, and N is the total number of Zn and O atoms in the ZnO nanoclusters. Based on the density functional theory (DFT) calculations of the different edges of ZnO nanoclusters (Figure 9 and Model Systems in 3.6), the misorientation angles 0° and 30° are more stable for the ZnO monolayer on graphene due to the strong van der Waals interactions between the edge atoms of ZnO and graphene. Figure 8a shows the histogram of the observed misorientation angles and the calculated adhesion energies between the oxygen-terminated triangular ZnO nanocluster and graphene. The counts of the experimental misorientation angle correspond well with the computational adhesion energy.

Figure 8b shows the raw ARTEM image of Figure 6a, and Figure 8c shows the image simulation result of the ZnO monolayer on graphene. It is noteworthy that both images have tiny bright spots in the vacuum regions of the ZnO lattice. The contrast comes from constructive interferences of the exit waves generated by the distance between the ZnO monolayer and the graphene surface. We also compare the variations in the normalized intensity profiles of the experimental image and the simulated image at the imaging condition of the microscope. The similarity of the two intensity profiles in Figure 8b, c confirms the identical atomic structures of ZnO monolayers in these images.

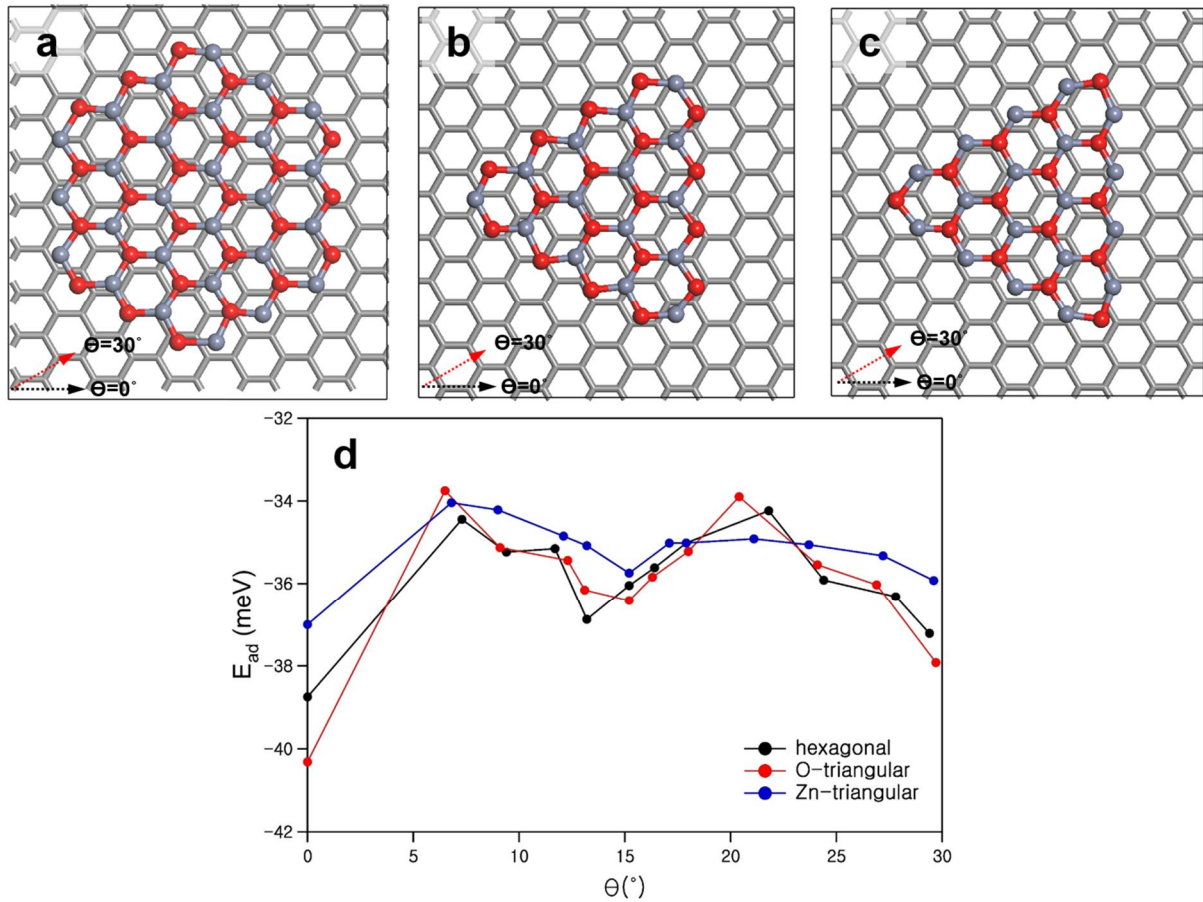


Figure 9. The optimized structure of hexagonal (a), oxygen-terminated (b) and zinc-terminated (c) triangular ZnO nanoclusters on graphene (See the Model Systems below for more information). The red and blue spheres represent oxygen and zinc atoms, respectively, and gray-stick honeycomb network represents graphene. (d) The adhesion energy between three types of ZnO nanoclusters and graphene vs the misorientation angle (θ).

3.5. Heteroepitaxial relations of the ZnO monolayer on graphene analyzed through aberration-corrected TEM

The ZnO monolayer on graphene monolayer assumes a graphene-like structure^{1, 71-75} rather than a wurtzite structure. ZnO monolayer nanoclusters have a predominantly zigzag edge configuration with a misorientation angle of 0° on graphene. Here, the *in situ* observation allows for demonstrating the atom-by-atom lateral growth of zinc and oxygen at a zigzag edge of the ZnO monolayer on graphene at atomic scale. Figure 10a, shows time-elapsd images of adsorbed ZnO adatoms on a graphene substrate. In order to understand the lateral growth at the edge, the formation energy, which may reveal the growth path, is estimated through DFT calculation. The formation energy E_f is defined as follows:

$$E_f = (E_{total} - E_G - N_{Zn}E_{Zn} - N_OE_O)/(N_{Zn} + N_O) \quad (2)$$

where E_{total} and E_G represent the energies of the ZnO monolayer on graphene and the freestanding graphene; E_{Zn} and E_O are the energies of zinc and oxygen atoms in vacuum; and N_{Zn} and N_O are the numbers of zinc and oxygen atoms in the total system, respectively. Based on the lateral growth model systems (Figure 11), the relative formation energy of the ZnO monolayer on graphene is estimated as shown in Figure 10b. After the first unstable adatom absorption, the formation energies tend to decrease. For oxygen- and zinc-terminated zigzag edges, the formation energies gradually decrease as the growth step increases. In particular, a large formation energy drop occurs by stabilizing the ZnO edge when a hexagonal structure is formed by adatom absorption. For the armchair edge, the formation energy fluctuates with increasing growth step. When adatoms form a full hexagonal structure, the formation energy decreases, but when they become dangling atoms, the formation energy increases. Consequently, the lateral growth of ZnO is energetically favorable for the zigzag edge over the armchair edge. In addition, parallel growth is favored less than lateral growth because of the continuous unstable adatom absorption at the pristine edge (Figure 12).

Figures 13a and c show the raw ARTEM image of Figure 10a at the final step 7 and the corresponding simulation image at the imaging condition, respectively. The ZnO adatoms are adsorbed onto the oxygen-terminated zigzag edges because these edges are more stable than Zn metal edges (Figure 10b). Figure 13b shows an intensity profile in the raw ARTEM image of Figure 13a, where Zn, O, and C atoms can be distinguished, because the Zn atoms display 4.5% higher intensity than the O atoms with $\pm 1.5\%$ deviation in the real image¹¹¹. This result reveals the lateral growth of ZnO as heteroepitaxy growth on graphene at the atomic scale. The observed ZnO monolayer appears crystallographically identical to the graphene-like structure. We draw attention to two findings from the results: First, the ZnO adatoms at the zigzag edges are energetically favorable, and oxygen-terminated edges are more stable than Zn-terminated edges (Figure 10, 11). Second, the ZnO adatoms along the growth direction are energetically more stable than those parallel to the growth direction (Figure 12).

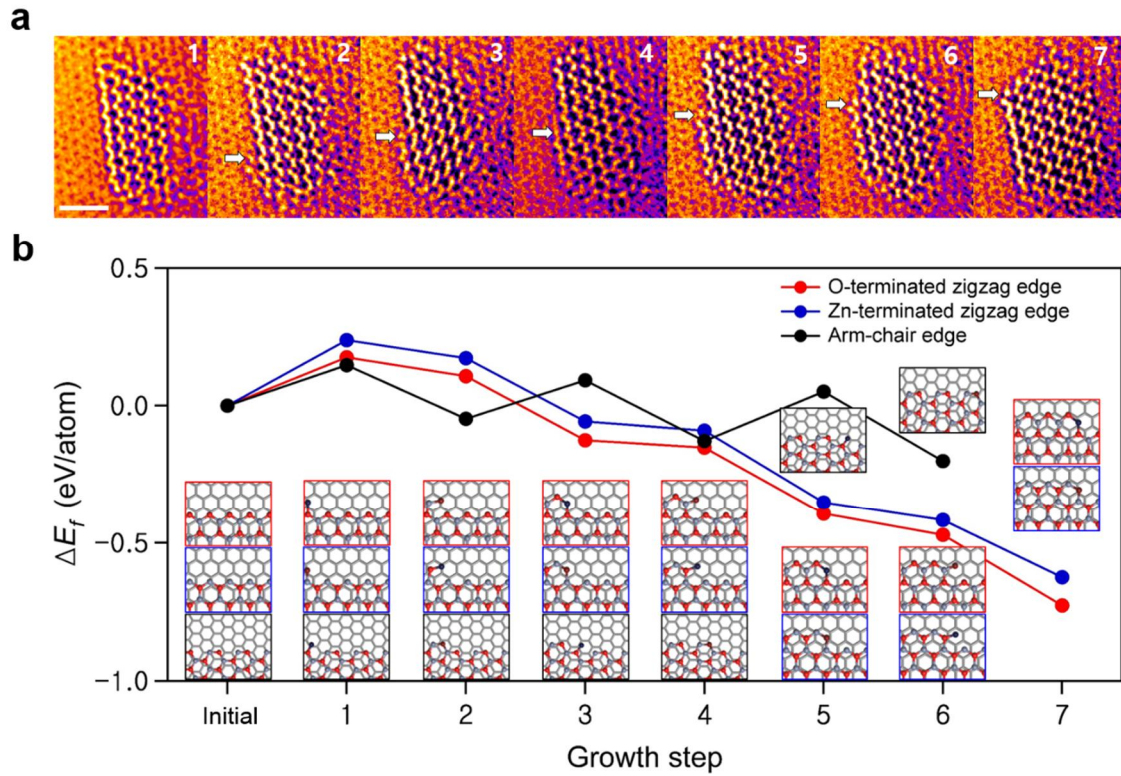


Figure 10. Lateral growth of the ZnO monolayer along the zigzag edges. (a) Time-elapsd ARTEM images show the adsorbed ZnO adatoms on graphene. (b) Relative formation energy (i.e., $\Delta E_f = E_{f_growth\ step} - E_{f_initial}$) of the lateral growth of the ZnO monolayer with oxygen- and zinc-terminated zigzag edges and armchair edge. The red and blue spheres represent oxygen and zinc atoms, respectively, and the gray-stick honeycomb network represents graphene. The scale bar is 1 nm.

Growth step	Initial	1	2	3	4	5	6	7
Zigzag (O-terminated)								
Zigzag (Zn-terminated)								
Armchair								-

Figure 11. The top view of atomic configuration of each lateral growth step of oxygen- and zinc-terminated zigzag edge models and armchair edge model, respectively. Note that each edge model consists of equal numbers of carbon, zinc, and oxygen atoms. The red, blue, burgundy, and navy spheres represent oxygen atoms, zinc atoms, oxygen adatom, and zinc adatom, respectively, and gray-stick honeycomb network represents graphene.

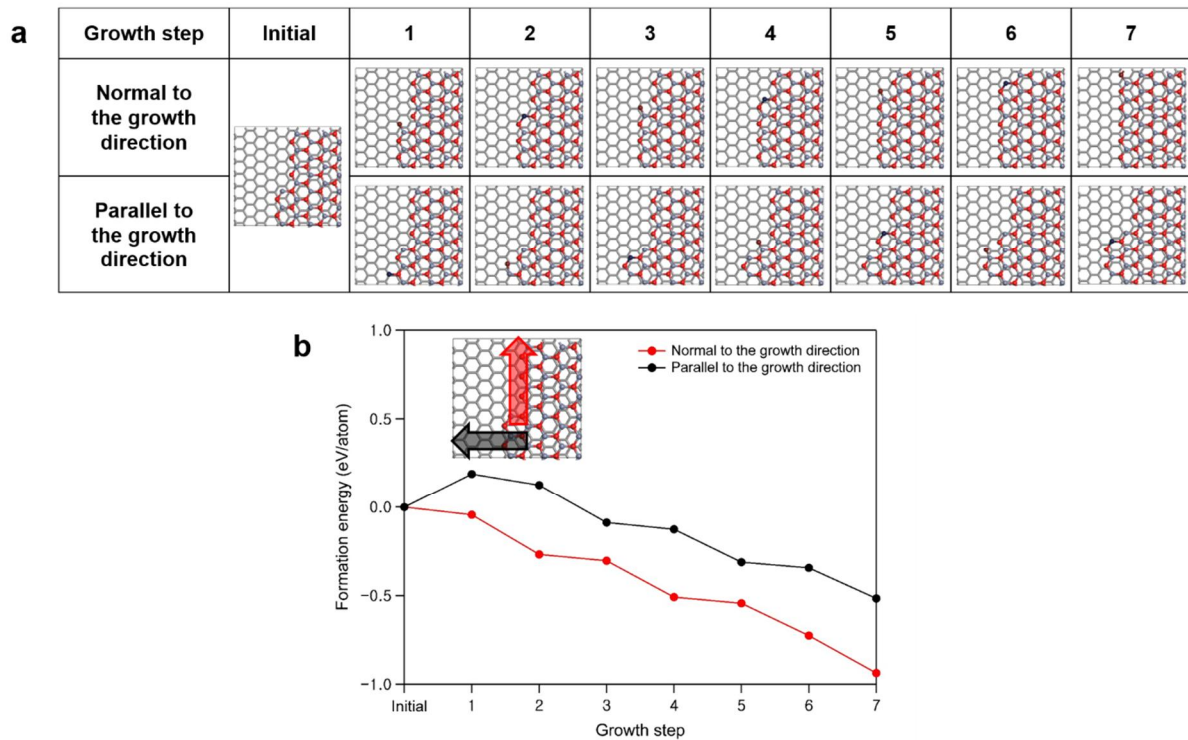


Figure 12. (a) Top view of atomic configuration of each growth step of normal and parallel to the growth front direction. Red, blue, burgundy, and navy spheres represent oxygen atoms, zinc atoms, oxygen adatom, and zinc adatom, respectively, and gray-stick honeycomb network represents graphene. (b) Formation energy of ZnO growth in normal and parallel to the growth front direction at oxygen terminated zigzag edges. The inset figure shows that the red arrow is normal to the growth front direction and the black arrow is parallel to the growth front of direction.

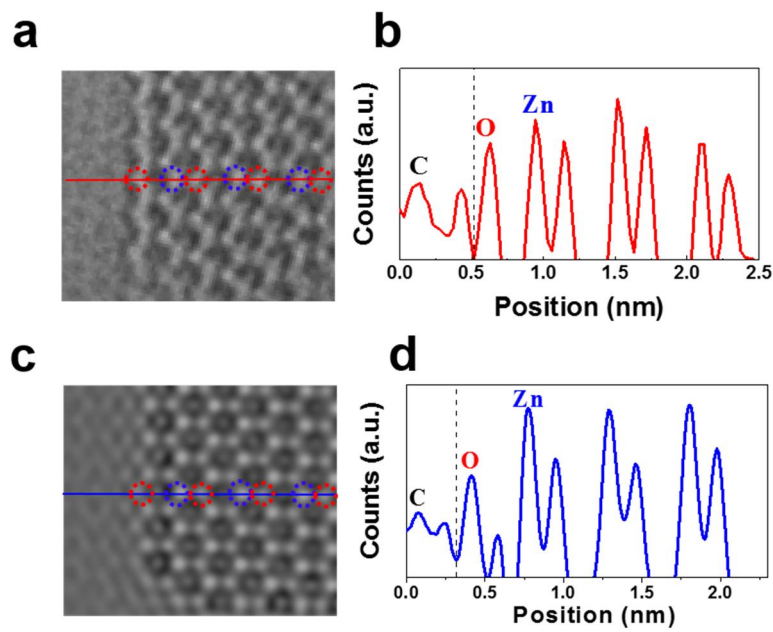


Figure 13. Lateral growth of the ZnO monolayer along the zigzag edges. (a) Raw image of Figure 10 (a) at final step 7. (b) Intensity profile acquired from the experimental image (red line). (c) Image simulation of Figure 10 (a) at final step 7. (d) Intensity profile acquired from the image simulation (blue line). The scale bar is 1 nm.

3.6. Model system

For the ZnO nanocluster model, we modeled hexagonal nanocluster and oxygen-terminated and zinc-terminated triangular ZnO nanoclusters to investigate edge effect for adhesion strength. $21.25 \times 22.13 \text{ \AA}^2$ rectangular graphene super-cell with 180 carbon atoms was used and 27 oxygen and zinc atoms were used for hexagonal ZnO nanocluster. 18 oxygen and 15 zinc atoms were used for oxygen-terminated triangular ZnO nanocluster. 15 oxygen and 18 zinc atoms were used for zinc-terminated triangular ZnO nanocluster (Figure 9). For lateral growth of ZnO model, $21.25 \times 19.58 \text{ \AA}^2$ rectangular graphene super-cell with 160 carbon atoms was used for ZnO growth model to minimize lattice mismatch with zigzag and armchair edge of ZnO. All initial system has 160 carbon atoms and 12 oxygen and zinc atoms (Figure 11). For ZnO growth of normal and parallel to the growth direction model, same size of graphene as lateral growth model was used for ZnO growth model to minimize lattice mismatch with zigzag of ZnO. Both normal to the growth and parallel to the growth direction initial systems have 160 carbon atoms and 26 oxygen and 27 zinc atoms (Figure 12). The Brillouin-zone integration of $3 \times 3 \times 1$ Monkhorst-Pack k-point grid¹¹² was used. All growth model systems were constructed with 0° orientation angle between ZnO and graphene which is most stable configuration based on experimental and simulation results. A vacuum space consisting of a 20 \AA normal to ZnO plane was used for all model system to avoid self-interactions. We modeled a periodic layer system with 4×4 supercell of hexagonal unit cell graphene and 3×3 supercell of ZnO monolayer. Lattice mismatch was about 0.59%. Geometry optimization was performed to find stable states (Figure 14) with the Brillouin-zone integration of $12 \times 12 \times 1$ Monkhorst-Pack k-point grid¹¹². Single layer ZnO on the graphene has graphene-like structure¹¹³ instead of wurtzite structure which is crystal structure of bulk ZnO.

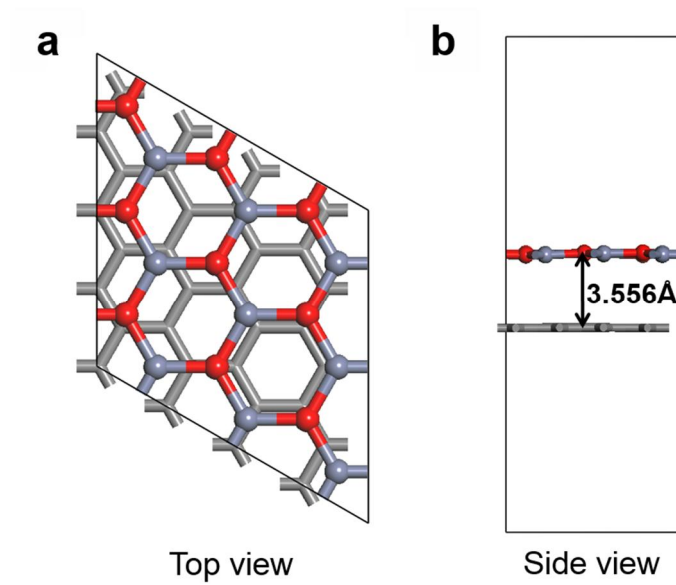


Figure 14. The top and side views of the optimized structure of periodic ZnO on graphene. (a) 4×4 supercell of hexagonal unit cell graphene is matched with a 3×3 supercell of ZnO monolayer, where the lattice mismatch is 0.59%. (b) The interlayer distance between ZnO monolayer and graphene is 3.556 Å. The red and blue spheres represent oxygen and zinc atoms, respectively, and gray-stick honeycomb network represents graphene.

3.7. Electronic and optical properties of ZnO deposited with different ALD cycles on UV/Ozone treated graphene

Bulk ZnO has a band gap of 3.37 eV at room temperature²¹. However, ZnO monolayer nanoclusters with a diameter of 2–4 nm or smaller (Figure 15 f, g) have increased band gaps due to strong quantum confinement effects⁸²⁻⁸³ and graphene-like crystallographic structure. Therefore, we anticipate a similar drastic change in the band gap of ZnO monolayer nanoclusters.

In this study, we experimentally measure the band gaps of the ZnO nanoclusters and verify the change in the band gaps of the ZnO monolayer QDs grown on graphene.

Figure 15a shows band gap measurements with electron energy loss spectroscopy (EELS) in the scanning transmission electron microscopy (STEM) mode for ZnO grown on graphene with different ALD cycles. Figure 15a shows the obtained EELS spectra after subtracting zero loss peaks. The band gaps are estimated from these spectra using a power law¹¹⁴. The results display higher band gap energy for smaller ZnO nanoclusters. For instance, a ZnO sample grown with 10 ALD cycles displays a band gap of 4.0 eV, whereas a ZnO sample grown with 200 ALD cycles exhibits a band gap of 3.25 eV, which is close to the bulk ZnO value. The observed gradual spectral shift in the band edge with the ALD cycles can be attributed to the expected quantum confinement effect⁸²⁻⁸³.

We also measure the variation in the band gap energy with a different experimental method. Figure 16 shows the optical transmission spectra obtained from the UV-VIS-NIR spectrophotometer. These spectra can provide plots of $(\alpha h\nu)^2$ as a function of photon energy ($h\nu$) for different ALD cycles—where α is the absorption coefficient of ZnO, defined as follows:

$$\alpha = \left(\frac{1}{\Delta d}\right) \ln\left(\frac{T_1}{T_2}\right) \quad (3)^{115}$$

Here, $\Delta d (= d_2 - d_1)$ is the thickness difference between the two ZnO films, and T_1 and T_2 are the transmittances of the two films. If $d_1 = 0$ (and $T_1 = 1$), we can also obtain the absorption coefficient of the ZnO film. The linear fit to the rapidly rising part of a spectrum gives the value for the optical band gap. Similar methods have been used for determining band gaps of various composite films. The ZnO band gaps for 10, 20, and 200 ALD cycles are determined in this way (Figure 16a-c). Indeed, the obtained band gaps are very close to those measured from the STEM-EELS spectra in Figure 15. This again verifies a significant change in band gap due to the quantum confinement effect in ZnO monolayer nanoclusters on graphene. The ZnO monolayer QDs on 2D materials with their tunable band gap can be a promising template for various photonic and electronic device applications. Figure 15b shows optical transmittance data of ZnO deposited with different ALD cycles on graphene. The ZnO films grown on graphene with 10 and 20 ALD cycles are nearly transparent, with flat optical transmittances of $T = 97.1\%$ and 96.8% at 550 nm, respectively. However, ZnO films grown with 200 cycles exhibit substantial reduction in transmittance ($T = 87.7\%$ at 550 nm). The drop in optical transmittance is highly nonlinear to the number of ALD cycles¹¹⁶ because the formation of ZnO

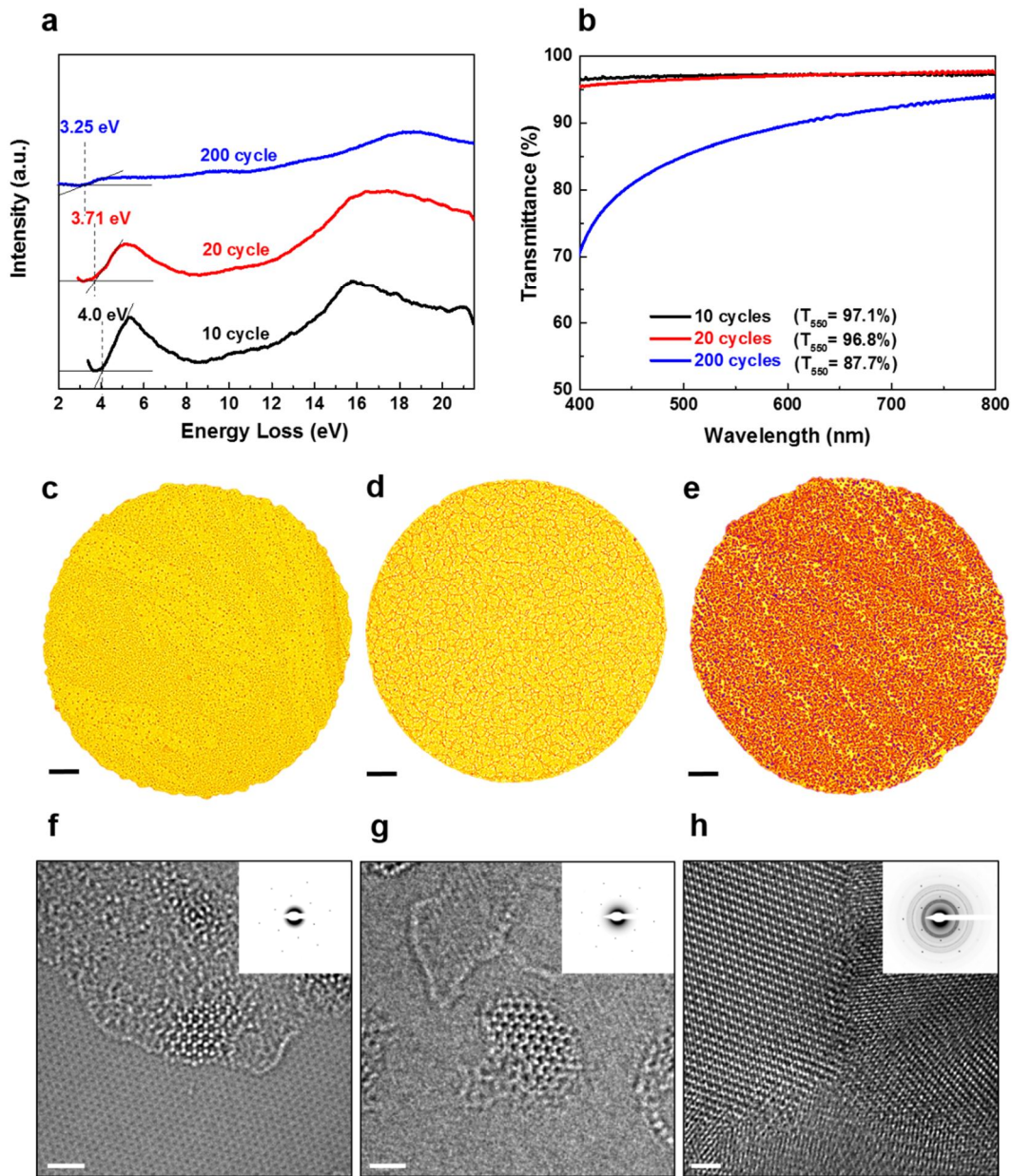


Figure 15. Electronic and optical properties of ZnO deposited with different ALD cycles on UV/Ozone treated graphene. (a) The STEM-EELS spectra of ZnO deposited with different ALD cycles on UV/Ozone-treated graphene. The extrapolation lines (dashed lines) indicate the band gap (E_g) values 4.0, 3.71, and 3.25 eV. Each curve is scaled differently. (b) Optical transmittance measurement of ZnO deposited with different ALD cycles on graphene. (c–e) Bright-field images of suspended UV/Ozone-treated graphene after 10, 20, and 200 cycles of ZnO ALD growth. The scale bar is 200 nm. (f–h) ARTEM images of 10, 20, and 200 cycles of ZnO ALD growth on the UV/Ozone-treated graphene substrate. The insets in the upper right corner show the electron diffraction patterns of the imaging regions (f–h). The scale bar is 1 nm.

nanoclusters, as observed in TEM images, results in a nonlinear expansion of the ZnO deposition area with increasing number of ALD cycles. The morphological development of the ZnO nanoclusters and their epitaxial relationship to graphene are characterized using bright-field TEM and atomic-resolution TEM. Figures 15c–e show bright-field TEM images of the ZnO nanostructures grown on graphene after UV/Ozone treatment for 180 s with 10, 20, and 200 ALD cycles. These TEM images display orange color for the ZnO monolayer and yellow for the graphene substrate. ZnO coverage on graphene increases significantly with the number of ALD cycles (Figure 15c–e). As shown in Figure 15e, a ZnO monolayer deposited with 200 cycles exhibits highly uniform and high-quality thin films on a large-area graphene substrate.

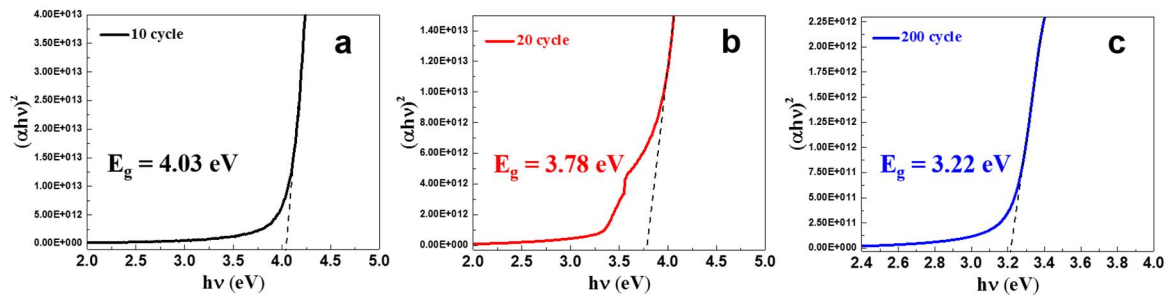


Figure 16. $(\alpha hv)^2$ versus photon energy of ZnO deposited on graphene by using ALD method. The extrapolation lines (dashed lines) indicate optical bandgaps (E_g) of 4.03, 3.78 and 3.22 eV for (a) 10 cycle, (b) 20 cycle and (c) 200 cycles.

In order to confirm the compositional changes of the 20 and 200 ZnO ALD cycles on UV/Ozone-treated graphene, Raman spectroscopy, X-ray diffraction and X-ray photoelectron spectroscopy (XPS) were carried out. In the Raman spectra of the 200 cycles ZnO on graphene, distinct ZnO peaks were observed near 1131 cm^{-1} and 1526 cm^{-1} (Figure 17). The X-ray diffraction patterns for the 200 cycles ALD grown ZnO on UV/Ozone-treated graphene sample revealed $[10\bar{1}0]$, $[0002]$, and $[10\bar{1}1]$ reflections of ZnO (Figure 18). XPS was also performed for the 20 and 200 ZnO ALD cycles on UV/Ozone-treated graphene on SiO_2/Si substrates (Figure 19). The peak of $1,022\text{ eV}$ in the spectra is corresponding to the Zn-O bonds (Figure 19a). Also, oxygen $1s$ spectra at 530.8 eV show O^{2-} ions in the Zn-O bonding of the ZnO film (Figure 19b). The other peaks located at 532.1 eV correspond to the oxygen atoms bonded to the zinc in the ZnO. We performed STEM HAADF imaging and EELS analysis. The EELS confirmed the presence of Zn and O by the presence of the O K-edge and Zn L-edge of the ZnO monolayer on graphene (Figure 20). In addition, the compositional analysis of ZnO monolayer was performed using a time-of-flight secondary ion mass spectrometry (TOF-SIMS). The TOF-SIMS maps show ZnO growth areas in yellow. ZnO coverage on graphene was enlarged as the ALD cycles increased (Figure 22a-c). Figures 15f–h show ARTEM images of ZnO nanostructures grown on graphene with 10, 20, and 200 ALD cycles. As shown in Fig. 15f, ZnO with 10 ALD cycles starts to develop nanoclusters of $1\text{--}2\text{ nm}$ in diameters. The diffraction pattern in the inset of Figure 15f shows mostly spot patterns of graphene because of the insufficient amount of crystalline ZnO. Figure 15g shows that the ZnO monolayer cluster gradually grows in size, by $2\text{--}3\text{ nm}$ in diameter. After 200 ALD cycles, coalescence takes place over the entire area of graphene and ZnO nanoclusters merge into larger grains, resulting in the formation of grain boundaries (Figure 15h). The diffraction patterns in the inset of Figure 15h shows the mixed spot patterns of nanosized polycrystalline ZnO and graphene.

3.8. Raman spectroscopy, X-ray diffraction, XPS, STEM-HAADF imaging, EELS core loss spectra and SEM measurement

ZnO nanostructures well grow on SiO₂/Si or Al₂O₃ substrates¹¹⁷. However, the lattice mismatch between ZnO and SiO₂ is larger than that between ZnO and graphene, and the SiO₂ used here is amorphous having many defect sites¹¹⁸. Therefore, these defect sites and the large lattice mismatch destabilize the energy of the ZnO-SiO₂ interface. The calculated results also show that the destabilization energy of the ZnO-graphene binding is 4.55 eV/nm², while that for ZnO-SiO₂ is 5.35 eV/nm², indicating that ZnO has a more stable bond with graphene than it does with amorphous SiO₂¹¹⁸. However, ZnO growth has some issue with graphene. Graphene is a strongly hydrophobic material, which limits its applications in metal oxide deposition and may contaminate the nanoelectromechanical systems. We performed UV/Ozone treatment for 180 seconds in order to induce the wettability transition in graphene from hydrophobic to hydrophilic. However, UV/Ozone treatment can usually induce lattice damaging in graphene. To minimize surface defects graphene sheet, we controlled UV/Ozone treatment time. Our UV/Ozone treatment did not deteriorate a graphene structure for electrical properties notably. Figure 17 shows Raman spectra of 20 and 200 ZnO ALD cycles on UV/Ozone-treated graphene on SiO₂/Si substrate. In the Raman spectra of the 200 cycles ZnO on graphene, distinct ZnO peaks were observed near 1131 cm⁻¹ and 1526 cm⁻¹, respectively. A negligible difference in I_D/I_G between the 20 cycles ZnO and 200 cycles ZnO is clearly observed. X-ray diffraction (XRD) of the 20 and 200 ZnO ALD cycles on UV/Ozone-treated graphene prepared on SiO₂/Si substrates are shown in Figure 18. In the X-ray diffraction patterns for the 200 cycles ALD grown ZnO on UV/Ozone-treated graphene sample revealed a [10 $\bar{1}$ 0], [0002], and [10 $\bar{1}$ 1] reflections. Figure 19 shows the Zn 2p_{3/2}, 2p_{1/2} and O 1s XPS spectra for the 20 and 200 ZnO ALD cycles on UV/Ozone-treated graphene on SiO₂/Si substrates. The binding energies were calibrated by taking the C 1s peak (284.6 eV).

Supplementary Figure 20 shows comparison of EEL spectra of a ZnO monolayer and a ZnO multilayer. Supplementary Figure 20a shows atomic resolution TEM image of ZnO on graphene. We then switched to the STEM mode and acquired quickly an HAADF image and simultaneously EEL spectra. STEM HAADF images show the contrast difference between ZnO monolayer, multilayer and graphene. The corresponding oxygen K-edge and zinc L-edge spectra are presented in Supplementary Figure 20c, d. The inset figure in (c) shows signal for the carbon K-edge from ZnO monolayer on graphene.

Figure 21 shows scanning electron micrograph (SEM) of 20 and 200 ZnO ALD cycles on UV/Ozone-treated graphene on SiO₂/Si substrate. In the SEM image of the 200 cycles ZnO on graphene clearly shows uniform and high-quality growth thin film. The ALD technique is capable of growing uniform and high-quality thin films on a large-area graphene.

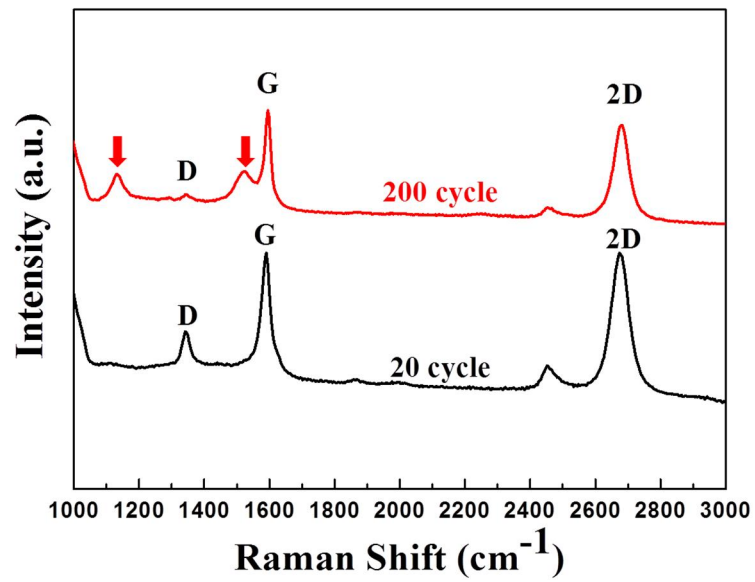


Figure 17. Raman spectroscopy of UV/Ozone-treated CVD graphene on the SiO₂/Si substrate, 20 and 200 ZnO ALD cycles.

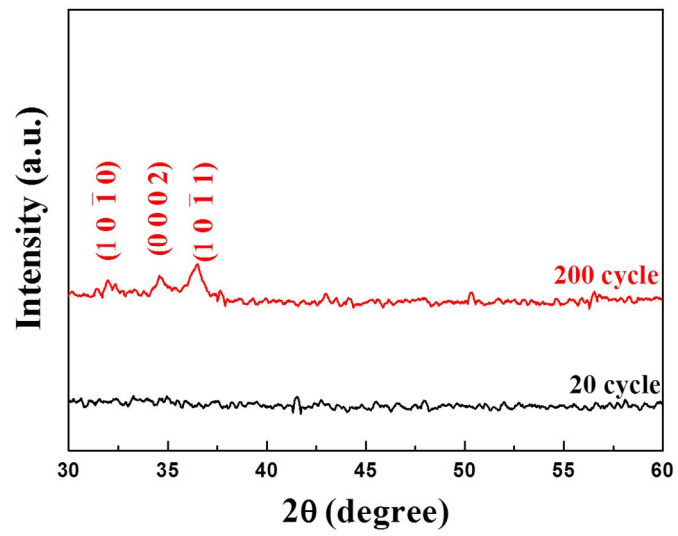


Figure 18. X-ray diffraction patterns of 20 and 200 ZnO ALD cycles on UV/Ozone-treated CVD graphene on the SiO₂/Si substrate.

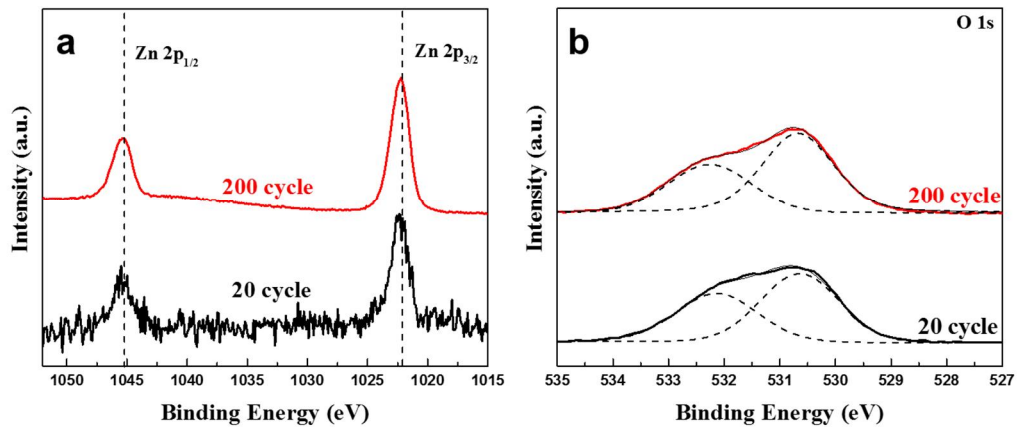


Figure 19. XPS spectra of UV/Ozone-treated CVD graphene on the SiO₂/Si substrate with 20 and 200 ZnO ALD cycles. (a) Zn 2p and (b) O 1s.

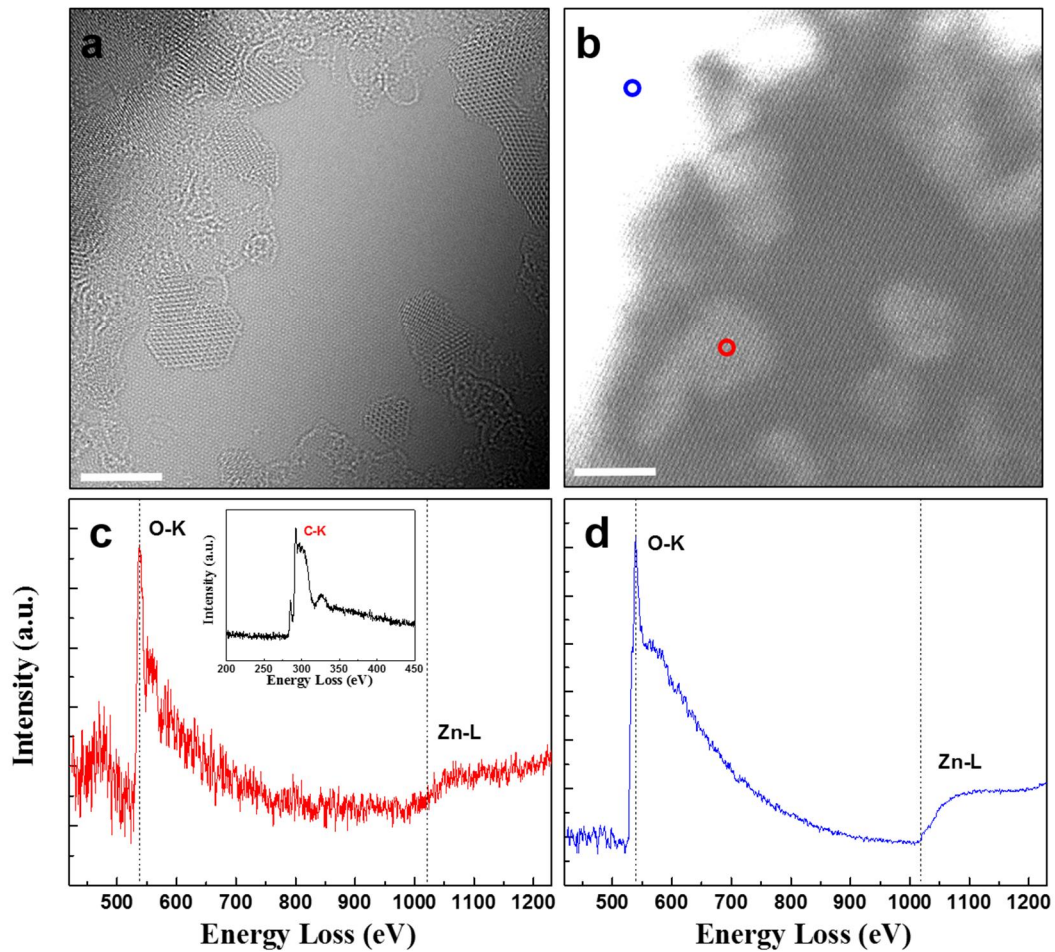


Figure 20. Comparison of EEL spectra of a ZnO monolayer and ZnO multilayer. (a) Atomic resolution TEM image of ZnO on graphene. (b) STEM HAADF image of ZnO on graphene. (c) EEL spectrum obtained from the red circle in (b) of show oxygen K-edge and zinc L-edge of the ZnO monolayer on graphene. The inset figure shows the carbon K-edge from graphene. (d) EEL spectrum obtained from the blue circle in (b) of oxygen K-edge and zinc L-edge of the multilayer ZnO on graphene. Scale bars indicate 5 nm.

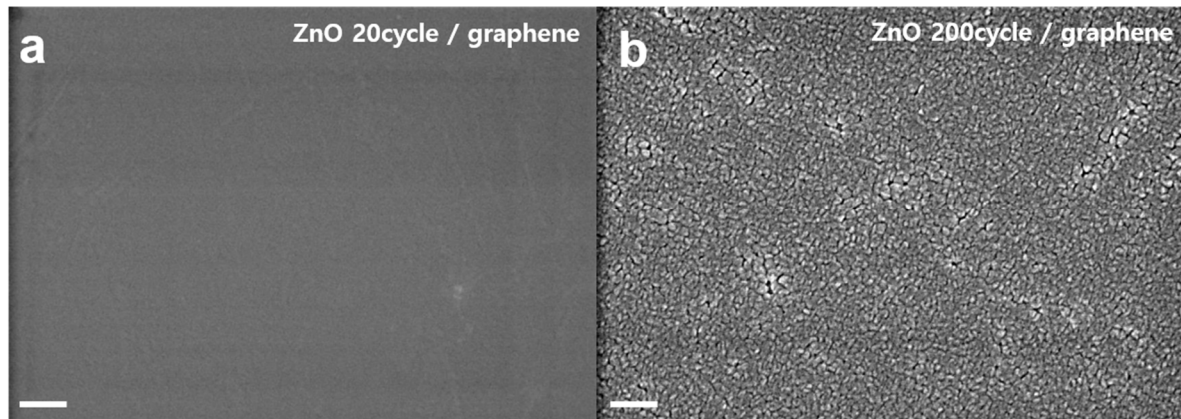


Figure 21. Scanning electron microscope images of UV/Ozone-treated CVD graphene on SiO₂/Si substrate. (a) SEM image of UV/Ozone-treated graphene on a SiO₂/Si substrate after 20 ALD cycles of ZnO deposition. (b) SEM image of UV/Ozone oxidized graphene on a SiO₂/Si substrate after 200 ALD cycles of ZnO deposition. The scale bar is 200 nm.

3.9. Compositional analysis of ZnO deposited on graphene by TOF-SIMS measurement

The compositional analysis of ZnO monolayer have been studied using Time-of-Flight Secondary Ion Mass Spectrometry (TOF-SIMS). Figure 22 shows TOF-SIMS elemental mapping and depth profile data of UV/Ozone-treated graphene on SiO₂/Si substrate, 20, 100 and 200 ZnO by using ALD cycles. TOF-SIMS mapping were analyzed in the area of 300 μm by 300 μm (Figure 22a-c). These TOF-SIMS mapping results show yellow color for ZnO growth areas. ZnO coverages on graphene were improved as the ALD cycles increased (Figure 22a-c). TOF-SIMS depth profiles were analyzed in the area of 70 μm by 70 μm (Figure 22d-f). Depth profile spectra of 20 cycle ZnO monolayer nanoclusters disappear as soon as etched of Cs ion after few seconds (Figure 22d). In case of 100 cycles of ZnO has uniform growth on graphene substrate (Figure 22e). Figure 22f shows 200 cycles of ZnO thin film. The ALD technique is capable of growing uniform and high-quality thin films on a large-area graphene substrate.

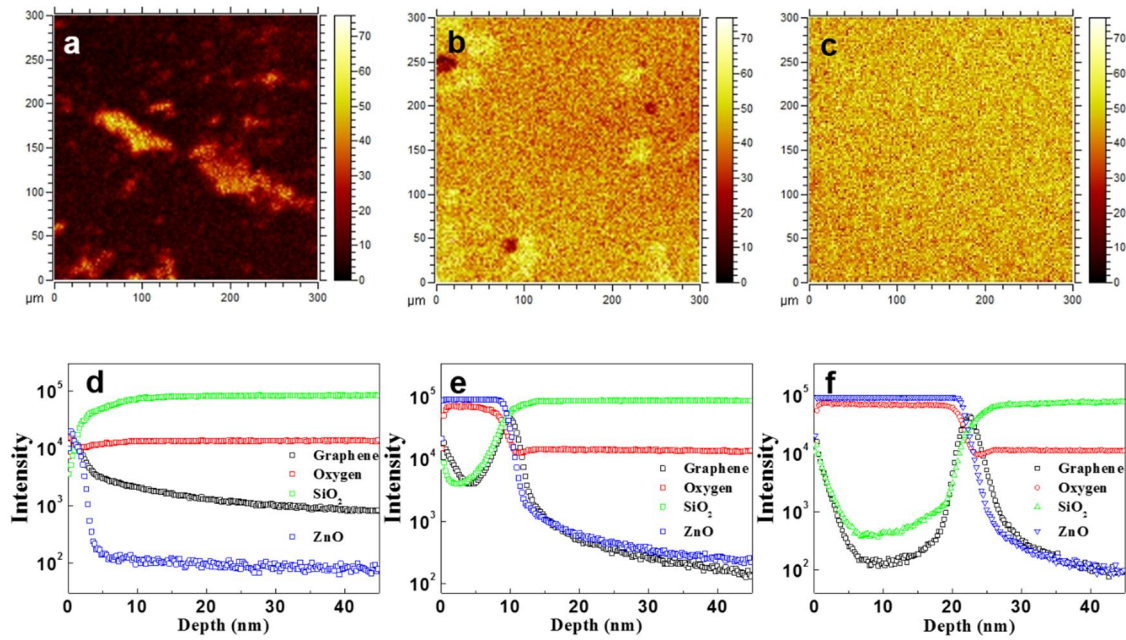


Figure 22. TOF-SIMS mapping images and depth profiles of UV/Ozone oxidized CVD graphene on SiO₂/Si substrate, 20 (a & d), 100 (b & e) and 200 (c & f) ZnO ALD cycles.

4. Conclusion

In summary, we demonstrate the formation of ZnO monolayer on graphene, which is the thinnest heteroepitaxial layer of semiconducting oxide on monolayer graphene. The optimized UV/Ozone treatment enhances the hydrophilicity of the graphene substrate without deteriorating its electrical properties due to lattice damage, and enables the epitaxial growth of ZnO. Through ARTEM investigation, the ZnO monolayer on graphene is directly observed at the atomic scale and its heterostructure is confirmed through image simulation. Most notably, we clearly show the *in situ* atom-by-atom growth of zinc and oxygen at the zigzag edge of the ZnO monolayer on graphene at the atomic scale. Both ARTEM observation and the calculation confirm that oxygen-terminated zigzag edges are more stable than zinc-terminated zigzag and armchair edges. We determine that two dominant misorientation angles (0° and 30°) are associated with the epitaxial growth of the ZnO monolayer on graphene and that the misorientation angle of 0° becomes more prominent as the ZnO monolayer grows. Moreover, we experimentally determine that the monolayer ZnO on graphene has a wide band gap of up to 4.0 eV, which is different from that of other ZnO nanostructures, due to the quantum confinement effect and the crystallographic structure. The heteroepitaxial stack of the thinnest 2D oxide semiconductors on graphene has potential for future optoelectronic device applications associated with high optical transparency and flexibility. This study can lead to a new class of 2D heterostructures including semiconducting oxides formed by highly controlled epitaxial growth through a deposition route.

Chapter 4: Synthesis of high-quality monolayer graphene by low-power plasma

1. Introduction

Graphene, which is a single layer of graphite¹¹⁹, has attracted extensive attention because of its potential applications in transparent electrodes¹²⁰⁻¹²¹ and electronic devices. Graphene has several extraordinary properties, including high carrier mobility^{85, 119, 122-123}, high electrical conductivity¹²¹, high transparency^{120, 124}, and good thermal conductivity¹²⁵⁻¹²⁷. Thus, graphene is regarded as a key material for future applications^{85-86, 119, 122-123}. Monolayer graphene has been synthesized extensively via mechanical exfoliation¹¹⁹, epitaxial growth on silicon carbide¹²⁸⁻¹²⁹, and chemical vapor deposition (CVD)¹³⁰⁻¹³². Among these methods, CVD is superior for synthesizing large-sized graphene.

Plasma-enhanced CVD (PECVD) is advantageous for the controlled synthesis of high-quality graphene. The synthesis of various carbon nanostructures, including carbon nanowalls¹³³⁻¹³⁴, carbon nanotubes¹³⁵, and nanosheets¹³⁶⁻¹³⁸, using PECVD has been demonstrated. Compared to thermal CVD, PECVD offers the advantages of high-density reactive gas atoms and shorter processing times¹³⁹ and the prospects of a relatively lower synthesis temperature (<1000°C) and faster growth¹⁴⁰⁻¹⁴¹. The quality of graphene synthesized by PECVD is highly influenced by plasma power. It highly affects whether hydrocarbon is dissociated, and it determines the concentration of precursors¹⁴². Additionally, nucleation density could be adjusted by modulating the plasma power. However, the concrete growth mechanism using PECVD is still in its infancy and a study of the effect of plasma on PECVD is essential.

We demonstrate the synthesis of high-quality monolayer graphene at 850°C on a copper foil using inductively coupled plasma chemical vapor deposition (ICP-CVD)^{139, 142-145}. The temperature is optimized to synthesize high-quality monolayer graphene using ICP-CVD. This conventional temperature is used to synthesize graphene by ICP-CVD. Moreover, we synthesized high-quality graphene by ICP-CVD under 50 W, which is a quite low plasma power, although monolayer graphene sheets are generally synthesized under 600 W by ICP-CVD according to most recent studies. A low plasma power synthesis helps to obtain better quality of graphene by reducing the damage compared to a high plasma power synthesis, and various substrates can be synthesized using low plasma power. We mainly discuss the effects of plasma on nucleation and subsequent growth of graphene. The plasma influence the generation of hydrogen species by decomposing hydrocarbon feedstock, such as methane (CH₄)¹⁴³. The generated hydrogen species act as an etchant and determine the size and morphology of graphene. Furthermore, it activates surface-bound carbon to synthesize high-quality monolayer graphene¹⁴⁶⁻¹⁴⁷. Elucidation of the ICP-CVD growth kinetics is necessary to establish the workable synthesis of high-quality graphene using supercapacitors, electronic device, and transparent electrode applications.

2. Experimental section

2.1. Graphene sample preparation

Graphene was synthesized by ICP-CVD on copper foil (99.8% Alfa Aesar, 13382). Copper foil was cleaned with H₂O/HCl (10:1), rinsed with acetone and alcohol, and dried under ambient air. The substrate was placed in an ICP-CVD vacuum chamber, its temperature was increased from 25°C to the synthesis temperature of 850°C at a rate of 25°C/min. The temperature was optimized to synthesize high-quality monolayer graphene. Graphene was synthesized by ICP-CVD at this conventional temperature. Ar and H₂ gas were flowed into the chamber at a flow rate of 100: 50 sccm. The base pressure of the chamber was maintained at 5×10^{-2} Torr. Before CH₄ gas was introduced, the plasma system was allowed to stabilize for 1 min. After the CH₄ gas was flowed at 1 sccm, 6×10^{-1} Torr of CH₄ was introduced for various times. In addition, the plasma power was controlled from 0 to 200 W to investigate the effect of plasma. The system was then cooled down to 25°C under flowing 1 sccm CH₄, 50 sccm H₂, and 100 sccm Ar.

2.2. Graphene transfer

Graphene was transferred onto 300-nm SiO₂ on Si substrate for surface characterization by scanning electron microscopy (SEM), Raman spectroscopy, and X-ray photoelectron spectroscopy and for incorporation into field-effect transistors, which were subsequently tested. A poly(methyl methacrylate) (PMMA) solution was spin-coated onto the graphene on copper foil.

To etch the underlying copper foil, the spin-coated graphene was placed onto a solution of sodium persulfate (Na₂S₂O₈) at a concentration of 5 g in 1 mL of deionized water. After the transferred specimen was dried in ambient air, the PMMA was dissolved with acetone for one day and the substrate was cleaned with isopropyl alcohol to yield a graphene film on the SiO₂ on Si substrate. For the direct transfer, support was provided by the target substrate—specifically, by the carbon film of a transmission electron microscopy (TEM) grid. For the TEM characterization, graphene was directly transferred onto Quantifoil holey carbon TEM grids (SPI Supplies, 300 mesh, 1.2- μ m hole size) using the direct transfer method.

2.3. Characterization

The domain sizes of graphene films on copper substrates were analyzed by SEM on S-4800 (Hitachi Instruments Inc.). Analysis by atomic-resolution transmission electron microscopy (ARTEM) was performed on an aberration-corrected transmission electron microscope (Titan G2 Cube 60-300 (FEI) installed at UNIST) operated at an accelerating voltage of 80 kV. Raman spectra were acquired with a WiTech confocal Raman microscope (He–Ne laser, $\lambda = 532$ nm). Electrical properties were measured using a physical property measurement system (PPMS, Quantum Design) in which the high-vacuum

and temperature conditions were controlled.

3. Results and discussion

3.1. Methane as an effective hydrogen source for monolayer graphene synthesis on Cu

CH₄ is known to provide hydrogen species; however, the process of generating hydrogen species from CH₄ requires its dissociation into active species^{143, 146-147}. We compare the thermal and plasma CVD methods with respect to the synthesis of graphene from a CH₄ source. In case of thermal CVD, the CH₄ source is not dissociated in the gas phase at temperatures generally used for graphene growth ($\leq 900^\circ\text{C}$)^{143, 148}. In case of PECVD, >80% of CH₄ is dissociated into other species such as H, H₂, CH₃, CH₂, and C₂H₄ because the plasma provides additional activation energy. In particular, ICP-CVD is effective to synthesize less-defective and highly uniform graphene at a low temperature and a low pressure along with a high plasma density among various types of PECVD.

Figs. 1a–c show graphene growth at 850°C for 12 s under various plasma powers of 0, 50, and 200 W in Ar/H₂/CH₄ gas mixtures. The average domain size was 0.62 μm when the plasma power was 0 W; however, it sharply increased to 7.5 μm when the plasma power was increased to 50 W. It also sharply decreased to 2.5 μm when the plasma power was further increased to 200 W. Fig. 1d is a graph of the domain size as a function of plasma power. The domain size reaches a maximum at 50 W because of the increased amount of hydrogen species generated under the plasma power. Graphene synthesis is well known to be highly dependent on the contribution of hydrogen. The generated hydrogen species act as an etchant, and it determines the size and morphology of graphene. Furthermore, it activates the surface-bound carbon to synthesize high-quality monolayer graphene¹⁴⁶. These catalyst and etching roles compete and influence the synthesis of high-quality graphene depending on the partial pressure of ambient H₂. Under low plasma power (≤ 50 W), the domain size increases because of the catalytic function that hydrogen plays in high-quality graphene growth. However, under 200 W, the domain size is reduced, which is due to the etching effect by hydrogen. Fig. 1e shows the Raman spectra of graphene synthesized for 12 s at various plasma powers of 0, 50, and 200 W. Graphene synthesized at 50 W shows the lowest I_D/I_G ratio (0) and the highest I_{2D}/I_G ratio (1.88), indicating that the structural quality of this graphene film was substantially better than that of the films synthesized at 0 and 200 W. In addition, a single-Lorentzian 2D peak was measured. The high-quality monolayer graphene was synthesized without defects (Fig. 1e). Graphene synthesized at 200 W shows the highest I_D/I_G value (1.475) and the lowest I_{2D}/I_G value (0.69), indicating that this graphene film was synthesized in few layers and contained the most defects among the graphene films synthesized under different plasma powers.

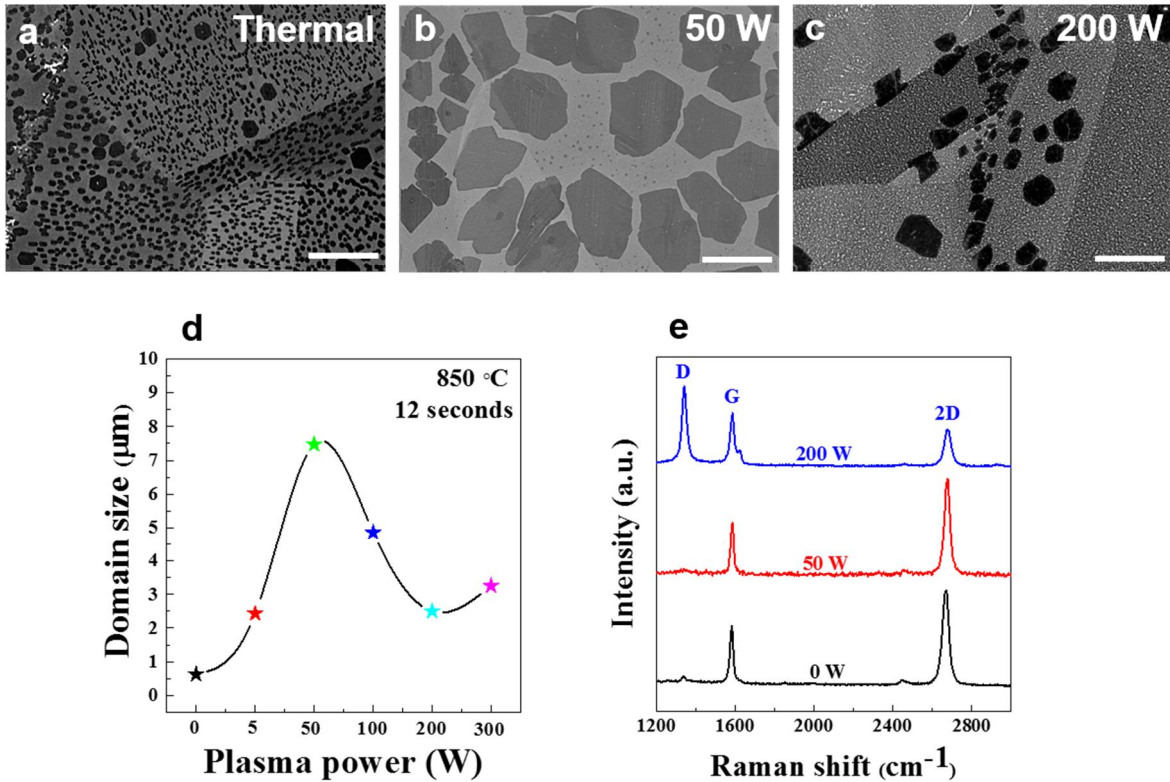


Figure 1. Graphene synthesized at 850°C for 12 s at plasma powers of 0, 50, and 200 W under an Ar/H₂/CH₄ gas mixture. (a)–(c) show SEM images of graphene domains synthesized at 850°C for 12 s at plasma powers of 0, 50, and 200 W under an Ar/H₂/CH₄ gas mixture. Scale bar is 5 μm. (d) Domain size of graphene as a function of plasma powers of 0–300 W. (h) Raman spectra of graphene synthesized for 12 s at various plasma powers of 0, 50, and 200 W.

3.2. Domain size and graphene coverage on copper foil using ICP-CVD

Fig. 2a shows the domain size of graphene synthesized at 850°C according to growth time at various plasma powers of 0, 50, and 200 W in an Ar/H₂/CH₄ gas mixture. The growth time required to fully cover the copper foil varied with the plasma power. With increasing growth time, graphene domains continued to grow laterally and coalesced into larger domains at 0 W because of the catalytic function of hydrogen species for graphene synthesis^{143, 146-147}. The average domain size was 0.62 μm when the growth time was 0.2 min; however, it sharply increased to 4.216 μm when the growth time was extended to 0.5 min. At 0 W, the graphene domain size increased nonlinearly with increasing growth time. The reduced domain sizes of graphene grown at 50 and 200 W are due to the etching effect of graphene by hydrogen^{143, 146-147}. In the case of 50 W, the domain size of graphene tended to decrease until 5 min; it then sharply increased to 10 μm after 30 min. After 60 min, synthesized graphene was a monolayer that fully covered the copper surface. When the plasma power was increased to 200 W, the time required for full coverage was reduced to 30 min at 850°C. Also, the graphene domain size decreased until 1 min of growth time but then sharply increased to 4.5 μm at 5 min and then increased to a graphene monolayer fully covering the substrate after 60 min. Overall, the lateral growth rate of graphene was promoted with increasing plasma power because of the increased amount of hydrogen species, which is attributed to the higher partial pressure of atomic hydrogen generated from hydrogen molecules by the ICP.

Fig. 2b shows graphene fully covered on copper foil according to growth time at different plasma powers. When the plasma power was 50 W, the copper surface was fully covered by graphene in 60 min under Ar/H₂/CH₄ conditions. When the plasma power was increased to 200 W, the full coverage time was reduced to 30 min (Fig. 2b). The growth rate was accelerated with increasing plasma power, which also promoted the growth of a second layer, as shown in Fig. 4c.

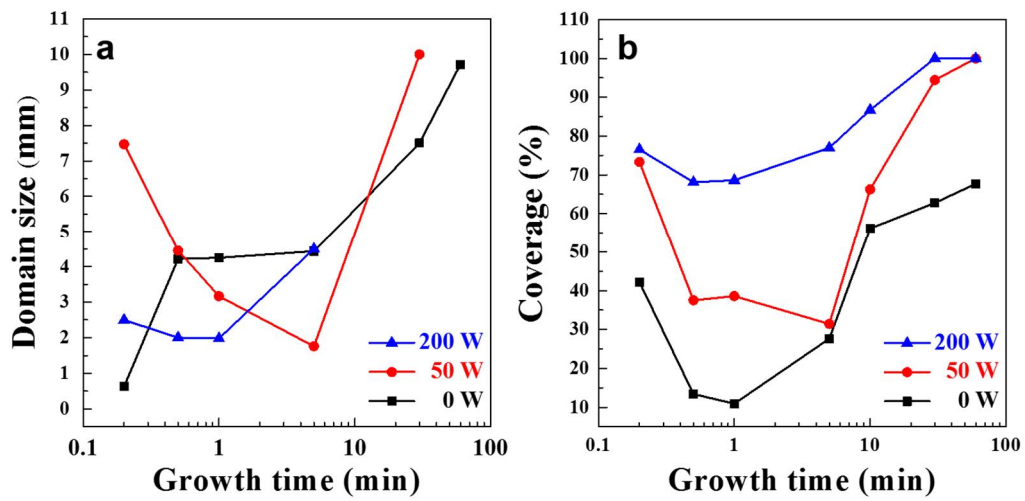


Figure 2. (a) Domain size of graphene and (b) Graphene coverage on copper foil as a function of growth time and plasma powers of 0, 50, and 200 W.

3.3. Graphene synthesized at 850°C for 60 min at plasma powers of 0, 50, and 200 W with an Ar/H₂/CH₄ gas mixture

Fig. 3a shows SEM images of graphene synthesized at 850°C for 60 min at various plasma powers of 0, 50, and 200 W in an Ar/H₂/CH₄ gas mixture. The growth time required to fully cover the copper foil again varied with the plasma power. When the plasma power was 0 W, graphene did not uniformly cover the copper foil, and the average domain size was 10 μm. Graphene grown under Ar/H₂/CH₄ conditions shows irregular, four-lobe-shaped domains. The graphene grown under plasma powers of 50 and 200 W covered the copper foil uniformly and had similar morphologies with each other. Fig. 3b shows the Raman spectra of graphene synthesized at various plasma powers of 0, 50, and 200 W for 60 min. The spectrum of graphene synthesized at 50 W shows the lowest I_D/I_G ratio (0) and the highest I_{2D}/I_G ratio (2.08), indicating that the structural quality of graphene was substantially improved compared with that of graphene synthesized at 0 W. The single-Lorentzian 2D peak indicates that graphene was a defect-free monolayer (Fig. 3b). ICP-CVD synthesizes graphene at a lower temperature and more rapidly compared with thermal CVD because plasma induces reactive gas atoms and radicals of a higher density¹⁴⁴.

For a plasma power of 200 W, the I_{2D}/I_G ratio reached approximately 1.42, which is in good agreement with the I_{2D}/I_G ratio of monolayer or bilayer graphene. However, the I_D/I_G ratio (0.5) is larger than the I_D/I_G ratio (0) of graphene grown at 50 W, likely because of defects resulting from inductively coupled plasma damage (Fig. 3c)¹⁴⁹. The high intensity of the D peak (Fig. 3c) and the broader full-width at half-maximum (FWHM) of the 2D band (Fig. 3d) at 0 W suggest a gradual increase of disorder in graphene synthesized at 0 W.

3.4. TEM images of graphene on copper foil

TEM images in Fig. 4 present graphene films synthesized at 850°C for 60 min on copper foil under Ar/H₂/CH₄ conditions according to the plasma powers of 0, 50, and 200 W. The films were transferred onto TEM grids to investigate how graphene grains were distributed through their diffraction patterns in conjunction with dark-field TEM technique (DF-TEM) to map the grain and grain boundaries of polycrystalline graphene films. Figs. 4a–c show grain-boundary maps superimposed on the corresponding TEM images of the graphene films depending on the plasma powers of 0, 50, and 200 W by applying the DF-TEM, which distinguishes adjacent grains on the graphene films through the obvious contrast differences described in Figs. 4d–f. When the plasma power was 0 W, the grains of graphene film showed diverse orientation and the grain sizes ranged from 5 to 15 μm, as shown in Fig 4a. The diffraction pattern in the inset of Fig. 4d suggests the existence of differently oriented grains in the graphene film. An ARTEM image in Fig. 4g also presents the monolayer graphene composed of different grains with 15° misorientation angle between grains 1 and 2. Figure 4b shows that the graphene grain size ranges from 5 to 10 μm on the monolayer graphene under our synthesis conditions at 50 W.

The diffraction pattern in the inset of Fig. 4e shows a small misorientation angle of 7° between grains 1 and 2. Under 200 W, the graphene comprises larger grains ranging from 15 to 20 μm compared with the graphene synthesized at 0 and 50 W (Fig. 4c).

Overall, the growth rate of graphene is promoted when the plasma power is increased because of the increased amount of hydrogen species caused by the higher partial pressure of hydrogen radical generated from hydrogen molecules by the ICP. However, the increased plasma power triggers the growth of second layer. As evident in Fig. 4f, the dark-field TEM image reveals two regions with an obvious contrast difference: Region 1 is monolayer graphene, whereas Region 2 is bilayer graphene. The ARTEM image in Fig. 4i also supports the coexistence of monolayer and twisted bilayer graphene with moiré patterns at the boundary between Region 1 and 2¹⁵⁰. Graphene is uniformly synthesized as a high-quality monolayer film at 50 W via direct mapping of the grain distribution using ARTEM.

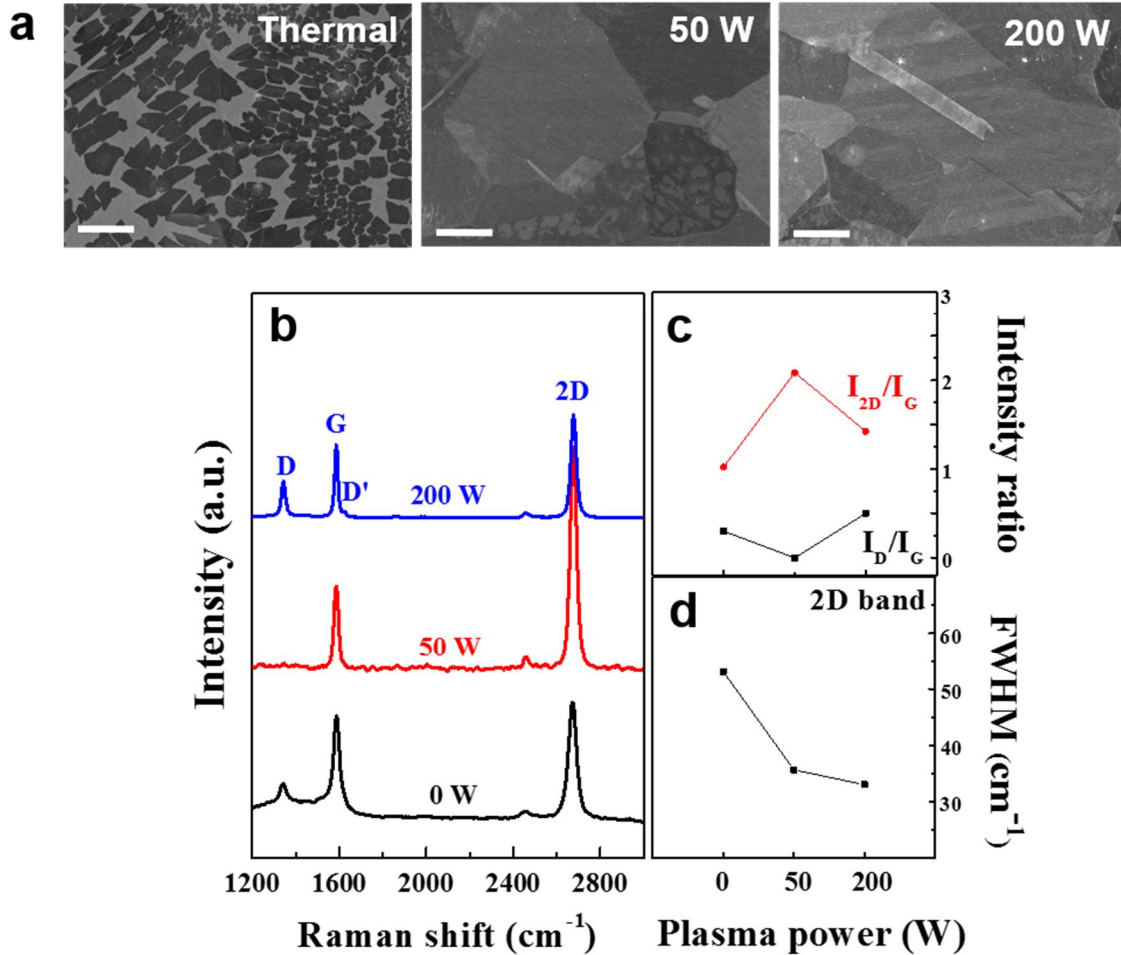


Figure 3. Graphene synthesized at 850°C for 60 min at plasma powers of 0, 50, and 200 W with an Ar/H₂/CH₄ gas mixture: (a) SEM image of graphene on copper foil synthesized at 850°C in 60 min as a function of plasma powers of 0, 50, and 200 W. Scale bars indicate 20 μm. (b) Raman spectra of graphene films on SiO₂/Si substrates, where the films were grown for 60 min at various plasma powers. (c) Intensity ratios of the D and 2D peaks to the G peak. (d) FWHM of a 2D band obtained from the single-Lorentzian fit.

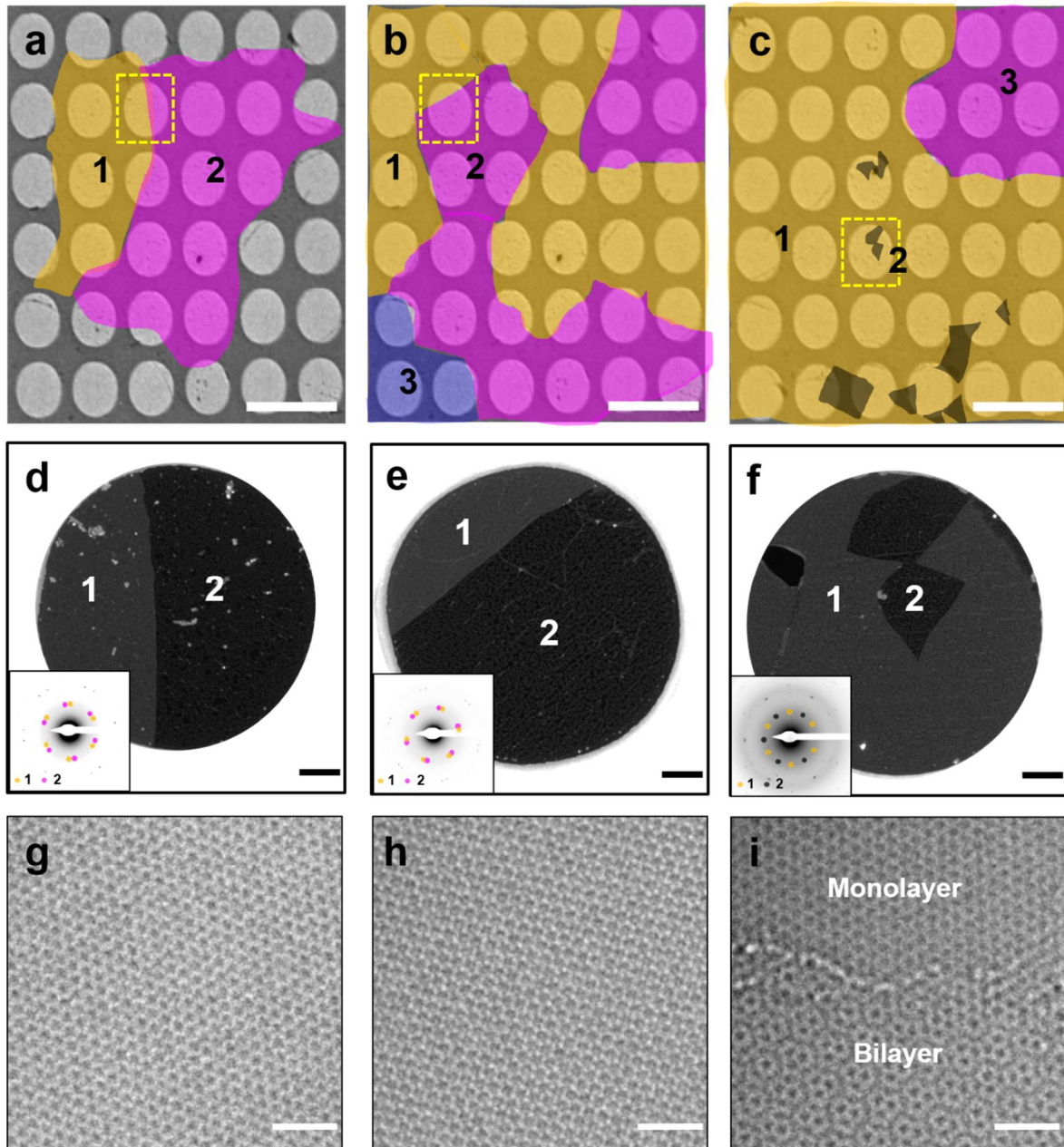


Figure 4. TEM images of graphene on copper foil synthesized at 850°C in 60 min under Ar/H₂/CH₄ conditions and plasma powers of 0, 50, and 200 W. (a)–(c) Grain-boundary map with an overlaid background of the graphene TEM image of the samples deposited at plasma powers of 0, 50, and 200 W, respectively. The yellow box represents dark-field image regions in Fig. 3(d)–(f). Scale bars indicate 5 μm. (d)–(f) Dark-field TEM images of graphene taken from areas 1 to 2. The inset at the bottom-left corner shows the diffraction pattern of the image. Scale bars indicate 200 nm. (g)–(i) ARTEM images of graphene deposited with plasma powers of 0, 50, and 200 W, respectively. Scale bars indicate 1 nm.

3.5. Electrical properties of graphene using ICP-CVD

The electrical properties of graphene were also investigated through measurements of field-effect transistors (FETs). The FETs were manufactured to have a synthesized graphene channel (width = 200 μm , length = 10 μm) between Au/Cr electrodes onto 300-nm SiO_2 on Si substrate. Fig. 5a shows the current gate voltage curves of the graphene films synthesized in 60 min according to plasma power (50 and 200 W). The type of carrier and the carrier concentration in the channel depend on the potential differences between the gates and channel. Negative gate voltages promote a p-type channel, and positive gate voltages lead to electron accumulation in the n-type channel¹⁵¹. The on-off ratios are approximately 4 (50 W) and 2.5 (200 W) in Fig. 5a. The points of neutral charge appear at approximately 32 V (50 W) and 25 V (200 W) in Fig. 5a. The shifted charge-neutral point demonstrate that some extrinsic hole-doping occurs in the graphene film, probably by residues from the PMMA or from the etching solutions¹⁴³. The experimentally confirmed FETs channel mobility μ is

$$\mu = \frac{1}{qn} \frac{I_{\text{DS}}/W}{V_{\text{DS}}/L}, \quad (1)$$

where I_{DS} is the drain-source current, q is the elementary charge, n is the carrier concentration, V_{DS} is the source-drain voltage, W is the channel width, and L is the channel length measured from optical microscope for each device¹⁵², respectively. Fig. 5b shows mobility-carrier density curves for graphene films according to plasma power at 50 and 200 W. In the film deposited at 50 W, the mobility of graphene was found to be $\sim 150 \text{ cm}^2/\text{V}\cdot\text{s}$ at a carrier concentration of 10^{12} cm^{-2} and at a channel length of 10 μm . In the film deposited at 200 W, the mobility of graphene was approximately $\sim 750 \text{ cm}^2/\text{V}\cdot\text{s}$ at a carrier concentration of 10^{12} cm^{-2} . We determined the dependency of the plasma power. In the sample deposited at 50 W, graphene was a monolayer, and its mobility was lower because of surface polar optical phonon scattering. By contrast, the mobility increased in the samples deposited at 200 W since the electric field of the surface polar optical phonon scattering was efficiently protected by the excessive graphene layer and because the mobility was governed by coulomb scattering¹⁵³.

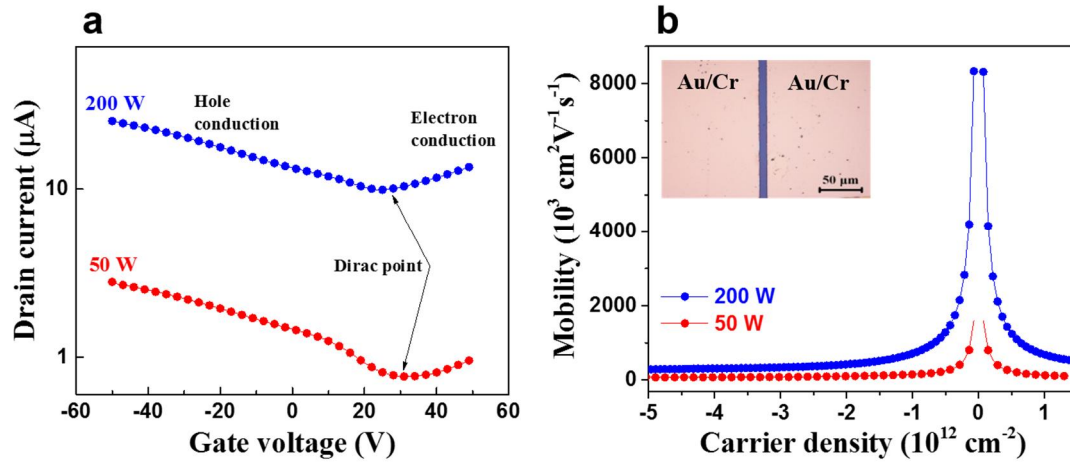


Figure 5. (a) Current gate voltage curves of the graphene films synthesized in 60 min as a function of plasma powers of 50 and 200 W. (b) Mobility–carrier concentration curves of graphene films as a function of plasma powers of 50 and 200 W. The inset at the upper corner shows an optical image of a 10- μm -long channel of an FET device using Au/Cr electrodes. Scale bar is 50 μm .

4. Conclusion

In summary, we demonstrated a double role of hydrogen on the graphene growth with ICP-CVD on copper foil. Graphene is synthesized inhomogeneously on the copper foil after 60 min without plasma. In contrast, it grows as a continuous film by covering the copper completely with either 50- or 200-W plasma, which is ascribed to activating surface-bound carbon for the growth of monolayer graphene. However, it takes the role of an etchant to manipulate the distribution of the graphene grains. Under low plasma power (≤ 50 W), the grain size of graphene is increased owing to the catalyst plays of hydrogen by activating surface-bound carbon for growth supported by the ARTEM investigation. Graphene is uniformly synthesized as a continuous high-quality monolayer film at 50 W via the direct mapping of the grain distribution using DF-TEM. By contrast, the grain size decreased under high plasma power over 50 W, which is ascribed to the etching role of hydrogen during the initial growth stage. It appears that the increased plasma power accelerates the growth rates along with promoting excessive layer growth. Therefore, the different grain sizes depending on the plasma power elucidates the growth kinetics of graphene associated with the role of hydrogen under ICP-CVD, which is in stark contrast to that under thermal CVD.

We think that our study provides insight to understand the kinetics of graphene growth under ICP and to control the synthesis of high-quality graphene applied to transparent electrodes and electronic devices.

References

1. Quang, H. T.; Bachmatiuk, A.; Dianat, A.; Ortmann, F.; Zhao, J.; Warner, J. H.; Eckert, J.; Cunniberti, G.; Rummeli, M. H., In Situ Observations of Free-Standing Graphene-like Mono- and Bilayer ZnO Membranes. *Acs Nano* **2015**, *9* (11), 11408-11413.
2. Kalantar-zadeh, K.; Ou, J. Z.; Daeneke, T.; Mitchell, A.; Sasaki, T.; Fuhrer, M. S., Two dimensional and layered transition metal oxides. *Applied Materials Today* **2016**, *5*, 73-89.
3. Goniakowski, J.; Finocchi, F.; Noguera, C., Polarity of oxide surfaces and nanostructures. *Reports on Progress in Physics* **2008**, *71* (1).
4. Mannhart, J.; Schlom, D. G., Oxide Interfaces-An Opportunity for Electronics. *Science* **2010**, *327* (5973), 1607-1611.
5. Choi, D.; Choi, M. Y.; Choi, W. M.; Shin, H. J.; Park, H. K.; Seo, J. S.; Park, J.; Yoon, S. M.; Chae, S. J.; Lee, Y. H.; Kim, S. W.; Choi, J. Y.; Lee, S. Y.; Kim, J. M., Fully rollable transparent nanogenerators based on graphene electrodes. *Adv Mater* **2010**, *22* (19), 2187-92.
6. Chung, K.; Lee, C. H.; Yi, G. C., Transferable GaN Layers Grown on ZnO-Coated Graphene Layers for Optoelectronic Devices. *Science* **2010**, *330* (6004), 655-657.
7. Lee, C. H.; Kim, Y. J.; Hong, Y. J.; Jeon, S. R.; Bae, S.; Hong, B. H.; Yi, G. C., Flexible inorganic nanostructure light-emitting diodes fabricated on graphene films. *Adv Mater* **2011**, *23* (40), 4614-9.
8. Mei, J.; Liao, T.; Kou, L. Z.; Sun, Z. Q., Two-Dimensional Metal Oxide Nanomaterials for Next-Generation Rechargeable Batteries. *Advanced Materials* **2017**, *29* (48).
9. Wang, F.; Seo, J. H.; Luo, G. F.; Starr, M. B.; Li, Z. D.; Geng, D. L.; Yin, X.; Wang, S. Y.; Fraser, D. G.; Morgan, D.; Ma, Z. Q.; Wang, X. D., Nanometre-thick single-crystalline nanosheets grown at the water-air interface. *Nature Communications* **2016**, *7*.
10. Zhang, Y. C.; Guerra-Nunez, C.; Utke, I.; Michler, J.; Agrawal, P.; Rossell, M. D.; Erni, R., Atomic Layer Deposition of Titanium Oxide on Single-Layer Graphene: An Atomic-Scale Study toward Understanding Nucleation and Growth. *Chemistry of Materials* **2017**, *29* (5), 2232-2238.
11. Zhu, J. B.; Bai, L. F.; Sun, Y. F.; Zhang, X. D.; Li, Q. Y.; Cao, B. X.; Yan, W. S.; Xie, Y., Topochemical transformation route to atomically thick Co₃O₄ nanosheets realizing enhanced lithium storage performance. *Nanoscale* **2013**, *5* (12), 5241-5246.
12. Wang, S. L.; Zhu, Y.; Luo, X.; Huang, Y.; Chai, J. W.; Wong, T. I.; Xu, G. Q., 2D WC/WO₃ Heterogeneous Hybrid for Photocatalytic Decomposition of Organic Compounds with Vis-NIR Light. *Advanced Functional Materials* **2018**, *28* (11).
13. Yin, K. B.; Zhang, Y. Y.; Zhou, Y. L.; Sun, L. T.; Chisholm, M. F.; Pantelides, S. T.; Zhou, W., Unsupported single-atom-thick copper oxide monolayers. *2d Materials* **2017**, *4* (1).
14. Wei, Z.; Hai, Z.; Akbari, M. K.; Qi, D. C.; Xing, K. J.; Zhao, Q.; Verpoort, F.; Hu, J.; Hyde, L.; Zhuiykov, S., Atomic layer deposition-developed two-dimensional alpha-MoO₃ windows

- excellent hydrogen peroxide electrochemical sensing capabilities. *Sensors and Actuators B-Chemical* **2018**, 262, 334-344.
15. Wang, S.; Huang, D.; Xu, S. S.; Jiang, W. K.; Wang, T.; Hu, J.; Hu, N. T.; Su, Y. J.; Zhang, Y. F.; Yang, Z., Two-dimensional NiO nanosheets with enhanced room temperature NO₂ sensing performance via Al doping. *Physical Chemistry Chemical Physics* **2017**, 19 (29), 19043-19049.
 16. Bai, J.; Han, S. H.; Peng, R. L.; Zeng, J. H.; Jiang, J. X.; Chen, Y., Ultrathin Rhodium Oxide Nanosheet Nanoassemblies: Synthesis, Morphological Stability, and Electrocatalytic Application. *Acs Applied Materials & Interfaces* **2017**, 9 (20), 17196-17201.
 17. Singh, M.; Della Gaspera, E.; Ahmed, T.; Walia, S.; Ramanathan, R.; van Embden, J.; Mayes, E.; Bansal, V., Soft exfoliation of 2D SnO with size-dependent optical properties. *2d Materials* **2017**, 4 (2).
 18. Carcia, P. F.; McLean, R. S.; Reilly, M. H.; Nunes, G., Transparent ZnO thin-film transistor fabricated by rf magnetron sputtering. *Applied Physics Letters* **2003**, 82 (7), 1117-1119.
 19. Pearton, S. J.; Norton, D. P.; Ip, K.; Heo, Y. W.; Steiner, T., Recent progress in processing and properties of ZnO. *Superlattices and Microstructures* **2003**, 34 (1-2), 3-32.
 20. Nomura, K.; Ohta, H.; Ueda, K.; Kamiya, T.; Hirano, M.; Hosono, H., Thin-film transistor fabricated in single-crystalline transparent oxide semiconductor. *Science* **2003**, 300 (5623), 1269-1272.
 21. Wang, Z. L., Zinc oxide nanostructures: growth, properties and applications. *Journal of Physics: Condensed Matter* **2004**, 16 (25), R829-R858.
 22. Billinge, S. J.; Levin, I., The problem with determining atomic structure at the nanoscale. *Science* **2007**, 316 (5824), 561-565.
 23. Urban, K. W., Studying atomic structures by aberration-corrected transmission electron microscopy. *Science* **2008**, 321 (5888), 506-510.
 24. Smith, D. J., The realization of atomic resolution with the electron microscope. *Reports on Progress in Physics* **1997**, 60 (12), 1513.
 25. Haider, M.; Uhlemann, S.; Schwan, E.; Rose, H.; Kabius, B.; Urban, K., Electron microscopy image enhanced. *Nature* **1998**, 392, 768-769.
 26. Dellby, N.; Krivanek, L.; Nellist, D.; Batson, E.; Lupini, R., Progress in aberration-corrected scanning transmission electron microscopy. *Journal of Electron Microscopy* **2001**, 50 (3), 177-185.
 27. Varela, M.; Lupini, A. R.; Benthem, K. v.; Borisevich, A. Y.; Chisholm, M. F.; Shibata, N.; Abe, E.; Pennycook, S. J., Materials characterization in the aberration-corrected scanning transmission electron microscope. *Annu. Rev. Mater. Res.* **2005**, 35, 539-569.

28. Lentzen, M., Progress in aberration-corrected high-resolution transmission electron microscopy using hardware aberration correction. *Microscopy and Microanalysis* **2006**, *12* (3), 191-205.
29. Smith, D. J., Development of aberration-corrected electron microscopy. *Microscopy and Microanalysis* **2008**, *14* (1), 2-15.
30. Uhlemann, S.; Haider, M., Residual wave aberrations in the first spherical aberration corrected transmission electron microscope. *Ultramicroscopy* **1998**, *72* (3), 109-119.
31. Krivanek, O.; Dellby, N.; Lupini, A., Towards sub-Å electron beams. *Ultramicroscopy* **1999**, *78* (1), 1-11.
32. Rose, H., Outline of a spherically corrected semiplanatic medium voltage transmission electron microscope. *Optik* **1990**, *85*, 19-24.
33. Haider, M.; Müller, H.; Uhlemann, S.; Zach, J.; Loebau, U.; Hoeschen, R., Prerequisites for a C c/C s-corrected ultrahigh-resolution TEM. *Ultramicroscopy* **2008**, *108* (3), 167-178.
34. Warner, J. H.; Margine, E. R.; Mukai, M.; Robertson, A. W.; Giustino, F.; Kirkland, A. I., Dislocation-driven deformations in graphene. *Science* **2012**, *337* (6091), 209-212.
35. Girit, Ç. Ö.; Meyer, J. C.; Erni, R.; Rossell, M. D.; Kisielowski, C.; Yang, L.; Park, C.-H.; Crommie, M.; Cohen, M. L.; Louie, S. G., Graphene at the edge: stability and dynamics. *science* **2009**, *323* (5922), 1705-1708.
36. Suenaga, K.; Koshino, M., Atom-by-atom spectroscopy at graphene edge. *Nature* **2010**, *468* (7327), 1088-1090.
37. Otten, M. T.; Coene, W. M., High-resolution imaging on a field emission TEM. *Ultramicroscopy* **1993**, *48* (1-2), 77-91.
38. Buseck, P.; Cowley, J.; Eyring, L., *High-Resolution Transmission Electron Microscopy: And Associated Techniques*. Oxford University Press: 1989.
39. Keast, V.; Scott, A.; Brydson, R.; Williams, D.; Bruley, J., Electron energy-loss near-edge structure—a tool for the investigation of electronic structure on the nanometre scale. *Journal of Microscopy* **2001**, *203* (2), 135-175.
40. Williams, D. B.; Carter, C. B., The transmission electron microscope. In *Transmission electron microscopy*, Springer: 1996; pp 3-17.
41. Gonzalez-Martinez, I. G.; Bachmatiuk, A.; Bezugly, V.; Kunstmann, J.; Gemming, T.; Liu, Z.; Cuniberti, G.; Rummeli, M. H., Electron-beam induced synthesis of nanostructures: a review. *Nanoscale* **2016**, *8* (22), 11340-11362.
42. Takamori, T.; Messier, R.; Roy, R., PHENOMENOLOGY OF EXPLOSIVE CRYSTALLIZATION OF SPUTTERED NON-CRYSTALLINE GERMANIUM FILMS. *Journal of Materials Science* **1973**, *8* (12), 1809-1816.

43. Das, V. D.; Lakshmi, P. J., ELECTRON-BEAM-INDUCED EXPLOSIVE CRYSTALLIZATION OF AMORPHOUS SE80TE20 ALLOY THIN-FILMS AND ORIENTED GROWTH OF CRYSTALLITES. *Physical Review B* **1988**, 37 (2), 720-726.
44. Ewing, R. C.; Headley, T. J., ALPHA-RECOIL DAMAGE IN NATURAL ZIRCONOLITE (CAZRTI2O7). *Journal of Nuclear Materials* **1983**, 119 (1), 102-109.
45. Weber, W. J.; Wald, J. W.; Matzke, H., EFFECTS OF SELF-RADIATION DAMAGE IN CM-DOPED GD2TI2O7 AND CAZRTI2O7. *Journal of Nuclear Materials* **1986**, 138 (2-3), 196-209.
46. Kern, P.; Muller, Y.; Patscheider, J.; Michler, J., Electron-beam-induced topographical, chemical, and structural patterning of amorphous titanium oxide films. *Journal of Physical Chemistry B* **2006**, 110 (47), 23660-23668.
47. Murray, J.; Song, K.; Huebner, W.; O'Keefe, M., Electron beam induced crystallization of sputter deposited amorphous alumina thin films. *Materials Letters* **2012**, 74, 12-15.
48. Meldrum, A.; Boatner, L. A.; Ewing, R. C., Electron-irradiation-induced nucleation and growth in amorphous LaPO4, ScPO4, and zircon. *Journal of Materials Research* **1997**, 12 (7), 1816-1827.
49. Lulli, G.; Merli, P. G.; Antisari, M. V., SOLID-PHASE EPITAXY OF AMORPHOUS-SILICON INDUCED BY ELECTRON-IRRADIATION AT ROOM-TEMPERATURE. *Physical Review B* **1987**, 36 (15), 8038-8042.
50. Corticelli, F.; Lulli, G.; Merli, P. G., SOLID-PHASE EPITAXY OF IMPLANTED SILICON AT LIQUID-NITROGEN AND ROOM-TEMPERATURE INDUCED BY ELECTRON-IRRADIATION IN THE ELECTRON-MICROSCOPE. *Philosophical Magazine Letters* **1990**, 61 (3), 101-106.
51. Jencic, I.; Bench, M. W.; Robertson, I. M.; Kirk, M. A., ELECTRON-BEAM-INDUCED CRYSTALLIZATION OF ISOLATED AMORPHOUS REGIONS IN SI, GE, GAP, AND GAAS. *Journal of Applied Physics* **1995**, 78 (2), 974-982.
52. Yang, X. X.; Wang, R. H.; Yan, H. P.; Zhang, Z., Low energy electron-beam-induced recrystallization of continuous GaAs amorphous foils. *Materials Science and Engineering B-Solid State Materials for Advanced Technology* **1997**, 49 (1), 5-13.
53. Kooi, B. J.; Groot, W. M. G.; De Hosson, J. T. M., In situ transmission electron microscopy study of the crystallization of Ge2Sb2Te5. *Journal of Applied Physics* **2004**, 95 (3), 924-932.
54. Zhang, T.; Song, Z. T.; Sun, M.; Liu, B.; Feng, S. L.; Chen, B., Investigation of electron beam induced phase change in Si2Sb2Te5 material. *Applied Physics a-Materials Science & Processing* **2008**, 90 (3), 451-455.

55. Lu, F. Y.; Shen, Y. Q.; Sun, X.; Dong, Z. L.; Ewing, R. C.; Lian, J., Size dependence of radiation-induced amorphization and recrystallization of synthetic nanostructured CePO₄ monazite. *Acta Materialia* **2013**, *61* (8), 2984-2992.
56. Nakamura, R.; Ishimaru, M.; Yasuda, H.; Nakajima, H., Atomic rearrangements in amorphous Al₂O₃ under electron-beam irradiation. *Journal of Applied Physics* **2013**, *113* (6).
57. Qin, W.; Nagase, T.; Umakoshi, Y., Electron irradiation-induced nanocrystallization of amorphous Fe₈₅B₁₅ alloy: Evidence for athermal nature. *Acta Materialia* **2009**, *57* (4), 1300-1307.
58. Borrnert, F.; Avdoshenko, S. M.; Bachmatiuk, A.; Ibrahim, I.; Buchner, B.; Cuniberti, G.; Rummeli, M. H., Amorphous Carbon under 80 kV Electron Irradiation: A Means to Make or Break Graphene. *Advanced Materials* **2012**, *24* (41), 5630-5635.
59. Zhao, J.; Deng, Q. M.; Bachmatiuk, A.; Sandeep, G.; Popov, A.; Eckert, J.; Rummeli, M. H., Free-Standing Single-Atom-Thick Iron Membranes Suspended in Graphene Pores. *Science* **2014**, *343* (6176), 1228-1232.
60. Sun, Z. Q.; Liao, T.; Kou, L. Z., Strategies for designing metal oxide nanostructures. *Science China-Materials* **2017**, *60* (1), 1-24.
61. Zhou, G. M.; Wang, D. W.; Yin, L. C.; Li, N.; Li, F.; Cheng, H. M., Oxygen Bridges between NiO Nanosheets and Graphene for Improvement of Lithium Storage. *Acs Nano* **2012**, *6* (4), 3214-3223.
62. Yang, S.; Yue, W. B.; Zhu, J.; Ren, Y.; Yang, X. J., Graphene-Based Mesoporous SnO₂ with Enhanced Electrochemical Performance for Lithium-Ion Batteries. *Advanced Functional Materials* **2013**, *23* (28), 3570-3576.
63. Ren, W. C.; Cheng, H. M., The global growth of graphene. *Nature Nanotechnology* **2014**, *9* (10), 726-730.
64. Ma, R. Z.; Sasaki, T., Nanosheets of Oxides and Hydroxides: Ultimate 2D Charge-Bearing Functional Crystallites. *Advanced Materials* **2010**, *22* (45), 5082-5104.
65. Li, L. H.; Chen, Y.; Behan, G.; Zhang, H. Z.; Petravic, M.; Glushenkov, A. M., Large-scale mechanical peeling of boron nitride nanosheets by low-energy ball milling. *Journal of Materials Chemistry* **2011**, *21* (32), 11862-11866.
66. Coleman, J. N.; Lotya, M.; O'Neill, A.; Bergin, S. D.; King, P. J.; Khan, U.; Young, K.; Gaucher, A.; De, S.; Smith, R. J.; Shvets, I. V.; Arora, S. K.; Stanton, G.; Kim, H. Y.; Lee, K.; Kim, G. T.; Duesberg, G. S.; Hallam, T.; Boland, J. J.; Wang, J. J.; Donegan, J. F.; Grunlan, J. C.; Moriarty, G.; Shmeliov, A.; Nicholls, R. J.; Perkins, J. M.; Grievson, E. M.; Theuwissen, K.; McComb, D. W.; Nellist, P. D.; Nicolosi, V., Two-Dimensional Nanosheets Produced by Liquid Exfoliation of Layered Materials. *Science* **2011**, *331* (6017), 568-571.
67. Nicolosi, V.; Chhowalla, M.; Kanatzidis, M. G.; Strano, M. S.; Coleman, J. N., Liquid Exfoliation of Layered Materials. *Science* **2013**, *340* (6139), 1420-+.

68. Tan, C. L.; Zhang, H., Wet-chemical synthesis and applications of non-layer structured two-dimensional nanomaterials. *Nature Communications* **2015**, *6*.
69. Huang, X.; Zeng, Z. Y.; Bao, S. Y.; Wang, M. F.; Qi, X. Y.; Fan, Z. X.; Zhang, H., Solution-phase epitaxial growth of noble metal nanostructures on dispersible single-layer molybdenum disulfide nanosheets. *Nature Communications* **2013**, *4*.
70. Sun, Z. Q.; Liao, T.; Dou, Y. H.; Hwang, S. M.; Park, M. S.; Jiang, L.; Kim, J. H.; Dou, S. X., Generalized self-assembly of scalable two-dimensional transition metal oxide nanosheets. *Nature Communications* **2014**, *5*.
71. Freeman, C. L.; Claeyssens, F.; Allan, N. L.; Harding, J. H., Graphitic nanofilms as precursors to wurtzite films: theory. *Phys Rev Lett* **2006**, *96* (6), 066102.
72. Tu, Z. C.; Hu, X., Elasticity and piezoelectricity of zinc oxide crystals, single layers, and possible single-walled nanotubes. *Physical Review B* **2006**, *74* (3).
73. Tusche, C.; Meyerheim, H. L.; Kirschner, J., Observation of depolarized ZnO(0001) monolayers: formation of unreconstructed planar sheets. *Phys Rev Lett* **2007**, *99* (2), 026102.
74. Lee, J.; Sorescu, D. C.; Deng, X., Tunable Lattice Constant and Band Gap of Single- and Few-Layer ZnO. *J Phys Chem Lett* **2016**, *7* (7), 1335-40.
75. Demel, J.; Pleštil, J.; Bezdička, P.; Janda, P.; Klementová, M.; Lang, K., Few-Layer ZnO Nanosheets: Preparation, Properties, and Films with Exposed {001} Facets. *The Journal of Physical Chemistry C* **2011**, *115* (50), 24702-24706.
76. Kim, Y. J.; Lee, J. H.; Yi, G. C., Vertically aligned ZnO nanostructures grown on graphene layers. *Applied Physics Letters* **2009**, *95* (21), 3.
77. Akhavan, O., Graphene Nanomesh by ZnO Nanorod Photocatalysts. *Acs Nano* **2010**, *4* (7), 4174-4180.
78. Kim, Y. J.; Hadiyawardan; Yoon, A.; Kim, M.; Yi, G. C.; Liu, C., Hydrothermally grown ZnO nanostructures on few-layer graphene sheets. *Nanotechnology* **2011**, *22* (24), 245603.
79. Yin, Z.; Wu, S.; Zhou, X.; Huang, X.; Zhang, Q.; Boey, F.; Zhang, H., Electrochemical deposition of ZnO nanorods on transparent reduced graphene oxide electrodes for hybrid solar cells. *Small* **2010**, *6* (2), 307-12.
80. Wu, S. X.; Yin, Z. Y.; He, Q. Y.; Huang, X. A.; Zhou, X. Z.; Zhang, H., Electrochemical Deposition of Semiconductor Oxides on Reduced Graphene Oxide-Based Flexible, Transparent, and Conductive Electrodes. *Journal of Physical Chemistry C* **2010**, *114* (27), 11816-11821.
81. Xu, C.; Lee, J.-H.; Lee, J.-C.; Kim, B.-S.; Hwang, S. W.; Whang, D., Electrochemical growth of vertically aligned ZnO nanorod arrays on oxidized bi-layer graphene electrode. *CrystEngComm* **2011**, *13* (20), 6036.
82. Viswanatha, R.; Sapra, S.; Satpati, B.; Satyam, P. V.; Dev, B. N.; Sarma, D. D., Understanding the quantum size effects in ZnO nanocrystals. *Journal of Materials Chemistry* **2004**, *14* (4), 661.

83. Kukreja, L. M.; Misra, P.; Fallert, J.; Sartor, J.; Kalt, H.; Klingshirn, C.; Ieee, *Nano - ZnO in Photonics Landscape*. Ieee: New York, 2008; p 61-66.
84. Saito, R.; Fujita, M.; Dresselhaus, G.; Dresselhaus, M. S., Electronic structure of chiral graphene tubules. *Applied Physics Letters* **1992**, *60* (18), 2204.
85. Geim, A. K.; Novoselov, K. S., The rise of graphene. *Nature Materials* **2007**, *6* (3), 183-191.
86. Castro Neto, A. H.; Guinea, F.; Peres, N. M. R.; Novoselov, K. S.; Geim, A. K., The electronic properties of graphene. *Reviews of Modern Physics* **2009**, *81* (1), 109-162.
87. Bolotin, K. I.; Sikes, K. J.; Jiang, Z.; Klima, M.; Fudenberg, G.; Hone, J.; Kim, P.; Stormer, H. L., Ultrahigh electron mobility in suspended graphene. *Solid State Communications* **2008**, *146* (9-10), 351-355.
88. Wang, F.; Zhang, Y. B.; Tian, C. S.; Girit, C.; Zettl, A.; Crommie, M.; Shen, Y. R., Gate-variable optical transitions in graphene. *Science* **2008**, *320* (5873), 206-209.
89. Gokus, T.; Nair, R. R.; Bonetti, A.; Bohmler, M.; Lombardo, A.; Novoselov, K. S.; Geim, A. K.; Ferrari, A. C.; Hartschuh, A., Making Graphene Luminescent by Oxygen Plasma Treatment. *Acs Nano* **2009**, *3* (12), 3963-3968.
90. Shin, Y. J.; Wang, Y.; Huang, H.; Kalon, G.; Wee, A. T. S.; Shen, Z.; Bhatia, C. S.; Yang, H., Surface-Energy Engineering of Graphene. *Langmuir* **2010**, *26* (6), 3798-3802.
91. Lee, B.; Park, S.-Y.; Kim, H.-C.; Cho, K.; Vogel, E. M.; Kim, M. J.; Wallace, R. M.; Kim, J., Conformal Al₂O₃ dielectric layer deposited by atomic layer deposition for graphene-based nanoelectronics. *Applied Physics Letters* **2008**, *92* (20), 203102.
92. Leconte, N.; Moser, J.; Ordejon, P.; Tao, H. H.; Lherbier, A.; Bachtold, A.; Alsina, F.; Torres, C. M. S.; Charlier, J. C.; Roche, S., Damaging Graphene with Ozone Treatment: A Chemically Tunable Metal-Insulator Transition. *Acs Nano* **2010**, *4* (7), 4033-4038.
93. Liu, L.; Ryu, S. M.; Tomasik, M. R.; Stolyarova, E.; Jung, N.; Hybertsen, M. S.; Steigerwald, M. L.; Brus, L. E.; Flynn, G. W., Graphene oxidation: Thickness-dependent etching and strong chemical doping. *Nano Letters* **2008**, *8* (7), 1965-1970.
94. Xu, Z.; Ao, Z.; Chu, D.; Younis, A.; Li, C. M.; Li, S., Reversible hydrophobic to hydrophilic transition in graphene via water splitting induced by UV irradiation. *Sci Rep* **2014**, *4*, 6450.
95. Liu, H.; Liu, Y.; Zhu, D., Chemical doping of graphene. *J. Mater. Chem.* **2011**, *21* (10), 3335-3345.
96. Jiang, Q. G.; Ao, Z. M.; Chu, D. W.; Jiang, Q., Reversible Transition of Graphene from Hydrophobic to Hydrophilic in the Presence of an Electric Field. *The Journal of Physical Chemistry C* **2012**, *116* (36), 19321-19326.
97. Huh, S.; Park, J.; Kim, Y. S.; Kim, K. S.; Hong, B. H.; Nam, J. M., UV/Ozone-Oxidized Large-Scale Graphene Platform with Large Chemical Enhancement in Surface-Enhanced Raman Scattering. *Acs Nano* **2011**, *5* (12), 9799-9806.

98. Mulyana, Y.; Uenuma, M.; Ishikawa, Y.; Uraoka, Y., Reversible Oxidation of Graphene Through Ultraviolet/Ozone Treatment and Its Nonthermal Reduction through Ultraviolet Irradiation. *The Journal of Physical Chemistry C* **2014**, *118* (47), 27372-27381.
99. Wang, W.; Ruiz, I.; Lee, I.; Zaera, F.; Ozkan, M.; Ozkan, C. S., Improved functionality of graphene and carbon nanotube hybrid foam architecture by UV-ozone treatment. *Nanoscale* **2015**, *7* (16), 7045-50.
100. Delley, B., An all-electron numerical method for solving the local density functional for polyatomic molecules. *The Journal of Chemical Physics* **1990**, *92* (1), 508.
101. Delley, B., From molecules to solids with the DMol3 approach. *The Journal of Chemical Physics* **2000**, *113* (18), 7756.
102. Materials Studio. *BIOVIA Inc.: San Diego, CA*, **2016**.
103. Perdew, J. P.; Burke, K.; Ernzerhof, M., Generalized gradient approximation made simple. *Physical Review Letters* **1996**, *77* (18), 3865-3868.
104. Grimme, S., Semiempirical GGA-type density functional constructed with a long-range dispersion correction. *J Comput Chem* **2006**, *27* (15), 1787-99.
105. Jiang, B.; Zhang, C.; Jin, C.; Wang, H.; Chen, X.; Zhan, H.; Huang, F.; Kang, J., Kinetic-Dynamic Properties of Different Monomers and Two-Dimensional Homoepitaxy Growth on the Zn-Polar (0001) ZnO Surface. *Crystal Growth & Design* **2012**, *12* (6), 2850-2855.
106. Peng, Z. A.; Peng, X. G., Nearly monodisperse and shape-controlled CdSe nanocrystals via alternative routes: Nucleation and growth. *J. Am. Chem. Soc.* **2002**, *124* (13), 3343-3353.
107. Kohler, U.; Dorna, V.; Jensen, C.; Kneppel, M.; Piaszenski, G.; Reshofs, K.; Wolf, C., *In-situ analysis of thin film growth using STM*. Elsevier Science Bv: Amsterdam, 2004; p 391-412.
108. Jo, J.; Yoo, H.; Park, S. I.; Park, J. B.; Yoon, S.; Kim, M.; Yi, G. C., High-resolution observation of nucleation and growth behavior of nanomaterials using a graphene template. *Adv Mater* **2014**, *26* (13), 2011-5.
109. Dulub, O.; Diebold, U.; Kresse, G., Novel stabilization mechanism on polar surfaces: ZnO(0001)-Zn. *Phys Rev Lett* **2003**, *90* (1), 016102.
110. Lauritsen, J. V.; Porsgaard, S.; Rasmussen, M. K.; Jensen, M. C. R.; Bechstein, R.; Meinander, K.; Clausen, B. S.; Helveg, S.; Wahl, R.; Kresse, G.; Besenbacher, F., Stabilization Principles for Polar Surfaces of ZnO. *Acs Nano* **2011**, *5* (7), 5987-5994.
111. Ryu, G. H.; Park, H. J.; Ryou, J.; Park, J.; Lee, J.; Kim, G.; Shin, H. S.; Bielawski, C. W.; Ruoff, R. S.; Hong, S.; Lee, Z., Atomic-scale dynamics of triangular hole growth in monolayer hexagonal boron nitride under electron irradiation. *Nanoscale* **2015**, *7* (24), 10600-5.
112. Monkhorst, H. J.; Pack, J. D., Special points for Brillouin-zone integrations. *Physical Review B* **1976**, *13* (12), 5188-5192.

113. Yao, Q.; Liu, Y.; Lu, R.; Xiao, C.; Deng, K.; Kan, E., Will a graphitic-like ZnO single-layer be an ideal substrate for graphene? *RSC Advances* **2014**, *4* (34), 17478.
114. Rafferty, B.; Brown, L. M., Direct and indirect transitions in the region of the band gap using electron-energy-loss spectroscopy. *Physical Review B* **1998**, *58* (16), 10326-10337.
115. Kim, E.; Jiang, Z. T.; No, K., Measurement and calculation of optical band gap of chromium aluminum oxide films. *Jpn. J. Appl. Phys. Part 1 - Regul. Pap. Short Notes Rev. Pap.* **2000**, *39* (8), 4820-4825.
116. Kim, K.; Lee, H. B.; Johnson, R. W.; Tanskanen, J. T.; Liu, N.; Kim, M. G.; Pang, C.; Ahn, C.; Bent, S. F.; Bao, Z., Selective metal deposition at graphene line defects by atomic layer deposition. *Nat Commun* **2014**, *5*, 4781.
117. Ahn, C. H.; Senthil, K.; Cho, H. K.; Lee, S. Y., Artificial semiconductor/insulator superlattice channel structure for high-performance oxide thin-film transistors. *Sci Rep* **2013**, *3*, 2737.
118. Choi, W. M.; Shin, K.-S.; Lee, H. S.; Choi, D.; Kim, K.; Shin, H.-J.; Yoon, S.-M.; Choi, J.-Y.; Kim, S.-W., Selective growth of ZnO nanorods on SiO₂/Si substrates using a graphene buffer layer. *Nano Research* **2011**, *4* (5), 440-447.
119. Novoselov, K. S.; Geim, A. K.; Morozov, S. V.; Jiang, D.; Zhang, Y.; Dubonos, S. V.; Grigorieva, I. V.; Firsov, A. A., Electric field effect in atomically thin carbon films. *Science* **2004**, *306* (5696), 666-669.
120. Kim, K. S.; Zhao, Y.; Jang, H.; Lee, S. Y.; Kim, J. M.; Kim, K. S.; Ahn, J. H.; Kim, P.; Choi, J. Y.; Hong, B. H., Large-scale pattern growth of graphene films for stretchable transparent electrodes. *Nature* **2009**, *457* (7230), 706-710.
121. Li, X. S.; Zhu, Y. W.; Cai, W. W.; Borysiak, M.; Han, B. Y.; Chen, D.; Piner, R. D.; Colombo, L.; Ruoff, R. S., Transfer of Large-Area Graphene Films for High-Performance Transparent Conductive Electrodes. *Nano Letters* **2009**, *9* (12), 4359-4363.
122. Novoselov, K. S.; Geim, A. K.; Morozov, S. V.; Jiang, D.; Katsnelson, M. I.; Grigorieva, I. V.; Dubonos, S. V.; Firsov, A. A., Two-dimensional gas of massless Dirac fermions in graphene. *Nature* **2005**, *438* (7065), 197-200.
123. Zhang, Y. B.; Tan, Y. W.; Stormer, H. L.; Kim, P., Experimental observation of the quantum Hall effect and Berry's phase in graphene. *Nature* **2005**, *438* (7065), 201-204.
124. Nair, R. R.; Blake, P.; Grigorenko, A. N.; Novoselov, K. S.; Booth, T. J.; Stauber, T.; Peres, N. M. R.; Geim, A. K., Fine structure constant defines visual transparency of graphene. *Science* **2008**, *320* (5881), 1308-1308.
125. Stankovich, S.; Dikin, D. A.; Dommett, G. H. B.; Kohlhaas, K. M.; Zimney, E. J.; Stach, E. A.; Piner, R. D.; Nguyen, S. T.; Ruoff, R. S., Graphene-based composite materials. *Nature* **2006**, *442* (7100), 282-286.

126. Balandin, A. A.; Ghosh, S.; Bao, W. Z.; Calizo, I.; Teweldebrhan, D.; Miao, F.; Lau, C. N., Superior thermal conductivity of single-layer graphene. *Nano Letters* **2008**, *8* (3), 902-907.
127. Balandin, A. A., Thermal properties of graphene and nanostructured carbon materials. *Nature Materials* **2011**, *10* (8), 569-581.
128. Berger, C.; Song, Z. M.; Li, T. B.; Li, X. B.; Ogbazghi, A. Y.; Feng, R.; Dai, Z. T.; Marchenkov, A. N.; Conrad, E. H.; First, P. N.; de Heer, W. A., Ultrathin epitaxial graphite: 2D electron gas properties and a route toward graphene-based nanoelectronics. *Journal of Physical Chemistry B* **2004**, *108* (52), 19912-19916.
129. Berger, C.; Song, Z. M.; Li, X. B.; Wu, X. S.; Brown, N.; Naud, C.; Mayou, D.; Li, T. B.; Hass, J.; Marchenkov, A. N.; Conrad, E. H.; First, P. N.; de Heer, W. A., Electronic confinement and coherence in patterned epitaxial graphene. *Science* **2006**, *312* (5777), 1191-1196.
130. Li, X. S.; Cai, W. W.; Colombo, L.; Ruoff, R. S., Evolution of Graphene Growth on Ni and Cu by Carbon Isotope Labeling. *Nano Letters* **2009**, *9* (12), 4268-4272.
131. Reina, A.; Jia, X. T.; Ho, J.; Nezich, D.; Son, H. B.; Bulovic, V.; Dresselhaus, M. S.; Kong, J., Large Area, Few-Layer Graphene Films on Arbitrary Substrates by Chemical Vapor Deposition. *Nano Letters* **2009**, *9* (1), 30-35.
132. Wei, D. C.; Liu, Y. Q.; Wang, Y.; Zhang, H. L.; Huang, L. P.; Yu, G., Synthesis of N-Doped Graphene by Chemical Vapor Deposition and Its Electrical Properties. *Nano Letters* **2009**, *9* (5), 1752-1758.
133. Vizireanu, S.; Nistor, L.; Haupt, M.; Katzenmaier, V.; Oehr, C.; Dinescu, G., Carbon nanowalls growth by radiofrequency plasma-beam-enhanced chemical vapor deposition. *Plasma Processes and Polymers* **2008**, *5* (3), 263-268.
134. Davami, K.; Shaygan, M.; Kheirabi, N.; Zhao, J.; Kovalenko, D. A.; Rummeli, M. H.; Opitz, J.; Cuniberti, G.; Lee, J. S.; Meyyappan, M., Synthesis and characterization of carbon nanowalls on different substrates by radio frequency plasma enhanced chemical vapor deposition. *Carbon* **2014**, *72*, 372-380.
135. Li, Y. M.; Mann, D.; Rolandi, M.; Kim, W.; Ural, A.; Hung, S.; Javey, A.; Cao, J.; Wang, D. W.; Yenilmez, E.; Wang, Q.; Gibbons, J. F.; Nishi, Y.; Dai, H. J., Preferential growth of semiconducting single-walled carbon nanotubes by a plasma enhanced CVD method. *Nano Letters* **2004**, *4* (2), 317-321.
136. Joshi, R. K.; Gomez, H.; Alvi, F.; Kumar, A., Graphene Films and Ribbons for Sensing of O₂ and 100 ppm of CO and NO₂ in Practical Conditions. *Journal of Physical Chemistry C* **2010**, *114* (14), 6610-6613.
137. Terasawa, T.; Saiki, K., Growth of graphene on Cu by plasma enhanced chemical vapor deposition. *Carbon* **2012**, *50* (3), 869-874.

138. Bo, Z.; Yang, Y.; Chen, J. H.; Yu, K. H.; Yan, J. H.; Cen, K. F., Plasma-enhanced chemical vapor deposition synthesis of vertically oriented graphene nanosheets. *Nanoscale* **2013**, *5* (12), 5180-5204.
139. Nang, L. V.; Kim, E.-T., Controllable Synthesis of High-Quality Graphene Using Inductively-Coupled Plasma Chemical Vapor Deposition. *Journal of The Electrochemical Society* **2012**, *159* (4).
140. Woehrl, N.; Ochedowski, O.; Gottlieb, S.; Shibasaki, K.; Schulz, S., Plasma-enhanced chemical vapor deposition of graphene on copper substrates. *AIP Advances* **2014**, *4* (4).
141. Boyd, D. A.; Lin, W. H.; Hsu, C. C.; Teague, M. L.; Chen, C. C.; Lo, Y. Y.; Chan, W. Y.; Su, W. B.; Cheng, T. C.; Chang, C. S.; Wu, C. I.; Yeh, N. C., Single-step deposition of high-mobility graphene at reduced temperatures. *Nature Communications* **2015**, *6*.
142. Gao, L. B.; Xu, H.; Li, L. J.; Yang, Y.; Fu, Q.; Bao, X. H.; Loh, K. P., Heteroepitaxial growth of wafer scale highly oriented graphene using inductively coupled plasma chemical vapor deposition. *2d Materials* **2016**, *3* (2).
143. Kim, Y. S.; Lee, J. H.; Kim, Y. D.; Jerng, S. K.; Joo, K.; Kim, E.; Jung, J.; Yoon, E.; Park, Y. D.; Seo, S.; Chun, S. H., Methane as an effective hydrogen source for single-layer graphene synthesis on Cu foil by plasma enhanced chemical vapor deposition. *Nanoscale* **2013**, *5* (3), 1221-6.
144. Nang, L. V.; Kim, E.-T., Low-temperature synthesis of graphene on Fe₂O₃ using inductively coupled plasma chemical vapor deposition. *Materials Letters* **2013**, *92*, 437-439.
145. Cheng, L. X.; Yun, K. Y.; Lucero, A.; Huang, J.; Meng, X.; Lian, G. D.; Nam, H. S.; Wallace, R. M.; Kim, M.; Venugopal, A.; Colombo, L.; Kim, J., Low temperature synthesis of graphite on Ni films using inductively coupled plasma enhanced CVD. *Journal of Materials Chemistry C* **2015**, *3* (20), 5192-5198.
146. Vlassioux, I.; Regmi, M.; Dai, P. F. S.; Datskos, P.; Eres, G.; Smirnov, S., Role of Hydrogen in Chemical Vapor Deposition Growth of Large Single-Crystal Graphene. *ACS NANO* **2011**, *5* (7), 6069-6076.
147. Wei, D. C.; Lu, Y. H.; Han, C.; Niu, T. C.; Chen, W.; Wee, A. T. S., Critical Crystal Growth of Graphene on Dielectric Substrates at Low Temperature for Electronic Devices. *Angewandte Chemie-International Edition* **2013**, *52* (52), 14121-14126.
148. Hash, D. B.; Meyyappan, M., Model based comparison of thermal and plasma chemical vapor deposition of carbon nanotubes. *Journal of Applied Physics* **2003**, *93* (1), 750-752.
149. Pham, V. P.; Kim, K. H.; Jeon, M. H.; Lee, S. H.; Kim, K. N.; Yeom, G. Y., Low damage pre-doping on CVD graphene/Cu using a chlorine inductively coupled plasma. *Carbon* **2015**, *95*, 664-671.
150. Kim, J. H.; Kim, K.; Lee, Z., The Hide-and-Seek of Grain Boundaries from Moire Pattern Fringe of Two-Dimensional Graphene. *Scientific Reports* **2015**, *5*.

151. Schwierz, F., Graphene transistors. *Nat Nanotechnol* **2010**, *5* (7), 487-96.
152. Sabri, S. S.; Lévesque, P. L.; Aguirre, C. M.; Guillemette, J.; Martel, R.; Szkopek, T., Graphene field effect transistors with parylene gate dielectric. *Applied Physics Letters* **2009**, *95* (24).
153. Zhu, W.; Perebeinos, V.; Freitag, M.; Avouris, P., Carrier scattering, mobilities, and electrostatic potential in monolayer, bilayer, and trilayer graphene. *Physical Review B* **2009**, *80* (23).

* Chapter 3 is reproduced in part with permission of “Atomic scale study on growth and heteroepitaxy of ZnO monolayer on graphene, *Nano Letters*, 17, 120-127, 2017”

Copyright 2016 American Chemical Society.